



University of Maribor Press



ISSN 1854-0171

ACTA GEOTECHNICA SLOVENICA

2018/2
VOL. 15

- Monitoring of the Belca rockfall
- S_BRICK: A constitutive model for soils and soft rocks
- Loading and unloading test of hard rock and its elastoplastic damage coupling model
- Predicting the uplift capacity of vertically located two-plate anchors
- Consolidation analysis of clayey soils using analytical tools
- The effects of the geometric parameters of a circular shallow foundation on its uplift bearing capacity in loess soil
- The design of drilled displacement system piles using the cavity expansion theory



Ustanovitelji

Founders

Univerza v Mariboru, Fakulteta za gradbeništvo, prometno inženirstvo in arhitekturo
University of Maribor, Faculty of Civil Engineering, Transportation Engineering and Architecture

Univerza v Ljubljani, Fakulteta za gradbeništvo in geodezijo
University of Ljubljana, Faculty of Civil and Geodetic Engineering

Univerza v Ljubljani, Naravoslovnotehniška fakulteta
University of Ljubljana, Faculty of Natural Sciences and Engineering

Slovensko geotehniško društvo
Slovenian Geotechnical Society

Društvo za podzemne in geotehniške konstrukcije
Society for Underground and Geotechnical Constructions

Izdajatelj

Publisher

Univerza v Mariboru, Fakulteta za gradbeništvo, prometno inženirstvo in arhitekturo
Faculty of Civil Engineering, Transportation Engineering and Architecture

Odgovorni urednik

Editor-in-Chief

Bojana Dolinar University of Maribor

Uredniki

Co-Editors

Jakob Likar Geoport d.o.o.
University of Ljubljana
Janko Logar University of Ljubljana
Borut Macuh University of Maribor
Stanislav Škrabl University of Maribor
Milivoj Vulić University of Ljubljana
Bojan Žlender University of Maribor

Posvetovalni uredniki

Advisory Editors

Heinz Brandl Vienna University of Technology
Chandrakant. S. Desai University of Arizona
Bojan Majes University of Ljubljana
Pedro Seco e Pinto National Laboratory of Civil Eng.

Lektor

Proof-Reader

Paul McGuiness

Naklada

Circulation

200 izvodov - issues

Cena

Price

25 EUR/letnik - 25 EUR/vol.; (50 EUR for institutions/za institucije)

Tisk

Print

Tiskarna Saje

Revija redno izhaja dvakrat letno. Članki v reviji so recenzirani s strani priznanih mednarodnih strokovnjakov. Baze podatkov v katerih je revija indeksirana: SCIE - Science Citation Index Expanded, JCR - Journal Citation Reports / Science Edition, ICONDA - The international Construction database, GeoRef. Izid publikacije je finančno podprla Javna agencija za raziskovalno dejavnost Republike Slovenije iz naslova razpisa za sofinanciranje domačih periodičnih publikacij.

Uredniški odbor

Editorial Board

Marx Ferdinand Ahlinhan National University in Abomey
Amin Barari Aalborg University
Theodoros Hatzigogos Aristotle University of Thessaloniki
Vojkan Jovičič IRGO-Ljubljana
Rolf Katzenbach Technical University Darmstadt
Nasser Khalili The University of New South Wales, Sydney
Svetlana Melentijevic Complutense University of Madrid
Seyed Hamed Mirmoradi Federal University of Rio de Janeiro
Ana Petkovšek University of Ljubljana
Borut Petkovšek Slovenian National Building and Civil Engineering Institute
Mihael Ribičič University of Ljubljana
César Sagasetta University of Cantabria
Patrick Selvadurai McGill University
Stephan Semprich University of Technology Graz
Devendra Narain Singh Indian Institute of Technology, Bombay
Abdul-Hamid Soubra University of Nantes
Kiichi Suzuki Saitama University
Antun Szavits-Nossan University of Zagreb
Kosta Urumović Croatian geological survey
Ivan Vaniček Czech Technical University in Prague

Založnik

Published by

Univerzitetna založba Univerze v Mariboru
Slomškov trg 15, 2000 Maribor, Slovenija
e-pošta: zalozba@um.si, http://press.um.si/, http://journals.um.si/
University of Maribor Press
Slomškov trg 15, 2000 Maribor, Slovenia
e-mail: zalozba@um.si, http://press.um.si/, http://journals.um.si/

Naslov uredništva

Address

ACTA GEOTECHNICA SLOVENICA
Univerza v Mariboru, Fakulteta za gradbeništvo, prometno inženirstvo in arhitekturo
Smetanova ulica 17, 2000 Maribor, Slovenija
Telefon / Telephone: +386 (0)2 22 94 300
Faks / Fax: +386 (0)2 25 24 179
E-pošta / E-mail: ags@uni-mb.si

Spletni naslov

web Address

http://zalozba.um.si/index.php/ags/index

The journal is published twice a year. Papers are peer reviewed by renowned international experts. Indexation data bases of the journal: SCIE - Science Citation Index Expanded, JCR - Journal Citation Reports / Science Edition, ICONDA - The international Construction database, GeoRef. The publication was financially supported by Slovenian Research Agency according to the Tender for co-financing of domestic periodicals.

<i>A. Lazar in drugi</i> Monitoring skalnega podora Belca	<i>A. Lazar et al.</i> Monitoring of the Belca rockfall	2
<i>V. Vukadin in V. Jovičić</i> S_BRICK: Konstitutivni model za zemljine in mehke kamnine	<i>V. Vukadin and V. Jovičić</i> S_BRICK: A constitutive model for soils and soft rocks	16
<i>Z. Li in drugi</i> Obremenilni in razbremenilni preizkus trdnih kamnin in njihov elastoplastični model poškodbe kontakta	<i>Z. Li et al.</i> Loading and unloading test of hard rock and its elastoplastic damage coupling model	38
<i>G. Misir</i> Napovedovanje izvlečne nosilnosti navpičnih sider z dvema ploščama	<i>G. Misir</i> Predicting the uplift capacity of vertically located two-plate anchors	47
<i>B. S. Olek</i> Analiza konsolidacije glinastih tal s pomočjo analitičnih orodij	<i>B. S. Olek</i> Consolidation analysis of clayey soils using analytical tools	58
<i>C. Qiang in drugi</i> Učinki geometrijskih parametrov krožnega plitvega temelja na njegovo nosilnost na izvlek v rahlih zemljinah	<i>C. Qiang et al.</i> The effects of the geometric parameters of a circular shallow foundation on its uplift bearing capacity in loess soil	74
<i>J. Stacho</i> Načrtovanje sistema uvrtnih pilotov z odmikanjem z uporabo teorije razširjanja prostora	<i>J. Stacho</i> The design of drilled displacement system piles using the cavity expansion theory	81
Navodila avtorjem	Instructions for authors	92

MONITORING OF THE BELCA ROCKFALL

Aleš Lazar (*corresponding author*)
Geoservis, d.o.o
Litijska cesta 45, 1000 Ljubljana, Slovenia
E-mail: lazarales@gmail.com

Tomaž Beguš
Geotrias d.o.o.
Dimičeva ulica 14, 1000 Ljubljana, Slovenia
E-mail: t.begus@gmail.com

Milivoj Vulić
University of Ljubljana,
Faculty of Natural Sciences and Engineering
Aškerčeva cesta 12, 1000 Ljubljana, Slovenia
E-mail: milivoj.vulic@guest.arnes.si

MONITORING SKALNEGA PODORA BELCA

DOI <https://doi.org/10.18690/actageotechslov.15.2.2-15.2018>

Keywords

monitoring, deformation analysis, rock fall, landslide, terrestrial laser scanning, geotechnics

Ključne besede

monitoring, analiza deformacij, skalni podor, plaz, terestrično lasersko skeniranje, geotehnika

Abstract

This paper reviews the monitoring of the rock block above the forest road of Belca Jepca near the village of Belca in the municipality of Kranjska Gora, Slovenia. A rockfall in part of the block occurred in autumn 2014. Both classic and some new measurement technologies were used. The new technologies were implemented according to new findings: an unmanned aircraft was used in the hazardous and hardly accessible areas of the observation, a terrestrial laser scanner was used for the comprehensive observation of the rock slopes and large cracks were observed with the installation of invar wires. The deformation analysis uses data between 2014 and 2017, among which airborne laser scanning (ALS) data from 2014 is included. The study also includes a comparison of the airborne laser scanning and the terrestrial laser scanning.

Izvleček

V prispevku je podan pregled monitoringa skalnega bloka, ki se je jeseni 2014 sprožil nad gozdno cesto Belca Jepca v bližini vasi Belca v občini Kranjska gora v Sloveniji. V sklopu monitoringa je bila uporabljena tako klasična kot tudi najnovejša merska tehnologija. Metode dela smo prilagajali novim spoznanjem. Tako smo na nevarnih in težko dostopnih območjih za opazovanje uporabili brezpilotni zrakoplov, za celostno opazovanje skalnih brežin pa terestrični laserski skener. Analiza deformacij obsega podatke med letoma 2014 in 2017, med katerimi so uporabljeni tudi podatki aerolaserskega skeniranja površja, zajeti leta 2014. V raziskavi je vključena primerjava podatkov aerolaserskega skeniranja in terestričnega laserskega skeniranja.

1 INTRODUCTION

This paper reviews the monitoring of a rock block located near the village of Belca in the municipality of Kranjska Gora, Slovenia. The reason to begin monitoring the area was a rockfall from some parts of the rock block in September 2014 and the possibility of a collapse of the entire block. Geotechnical measurements were used as part of the monitoring process, as well as geolocating measurements, complemented by field geological surveys and observations using an unmanned aircraft. Of the measurement techniques, the following were

used: surveys using wire extensometers, tachometry and terrestrial laser scanning (TLS). We have also acquired lidar data from the summer of 2014, using airborne laser scanning (ALS), showing the status of the area before the rockfall. The analysis of the acquired data covers the period from 2014 to 2017. The aim of this research was to assess the risk of another rockfall, as well as finding a solution to achieve the safety and transportability of the road. We have used both classic and the latest measurement technology. In hard-to-reach areas, an unmanned aircraft was used for the observation, while a terrestrial laser scanner was used to comprehensively monitor the

rock slopes. The deformation analysis also includes a data comparison between the airborne laser scanning and the terrestrial laser scanning.

1.1 An overview of related works

Scaioni et al. [1] were the first to use terrestrial laser scanning for the monitoring of a rock block in the Alps, together with an interferometric synthetic aperture radar (InSAR), terrestrial photogrammetry and geotechnical measurements. Teza et al. [2] showed the monitoring of a rock block to assess the risk of a rockfall using TLS and infrared thermography (IRT). The first to try TLS for monitoring the movements and deformations were Gordon et al. [3] on an old wooden bridge. Gordon et al. [4] showed that the technology of laser scanning can be more efficient than classic methods for sensing the changes of flat objects due to the large number of acquired points. Alba et al. [5] used terrestrial laser scanning to control the stability of a big dam, while Schneider [6] used it to determine the inclination of a high water tower and the deformations of two dams. Tsakiri et al. [7] researched the required conditions to use a scanner to measure deformations, in the sense of calibrating the scanner and the processes of modelling clouds for movement sensing. The mentioned works are papers from conferences, while we found one article [8] in a scientific journal that describes using TLS for measuring deformations in an incriminating laboratory test. At the ISPRS congress in Beijing in 2008, the authors of [9, 10, 11, 12, 13] presented their work regarding the use of TLS for the measurements

of deformations. Berényi et al. [14] used TLS to measure how much large bridges sag in incriminating tests, while Vežočanik et al. [15] tried to determine the movement of a gas line using the movement of concrete columns connected to underground pipes. Abellán et al. [16] dealt with the field of sensing changes in natural environments. De Asís López et al. [17] used statistical methods to compare two clouds of points, accumulated in different ways. Harmening and Neuner [18] use clouds to flatten various 3D planes and compare them with one another.

1.2 The area of research

The area of interest is the right rock slope above the river Belca, which is above the forest road Belca Jepca, near the village of Belca. In the autumn of 2014 a rockfall with a volume of between 5,000 and 10,000 m³ was launched over the forest road. The terrain is rocky with some rockface on distinct slopes. The rock block is made from Upper Triassic rocks: massive dolomite and limestone, strongly tectonized: limited by open cracks. The main area of interest is the independent block between the road and the peak ridge that we call *Main block*. Its volume is estimated to be 150,000 m³. The most unstable block – *Upper block* – is clearly limited with 0.5-m-wide and 4–6-m deep cracks. The volume is estimated to be 16,000–20,000 m³. On the side of the main block some significant open cracks determine the *Side block*: 45,000 m³. The terrain is quite steep. Where there is no rock, the area is covered in a sparse pine forest. There are two distinct screes below the road, up to the valley of Belca, which is the main watercourse.

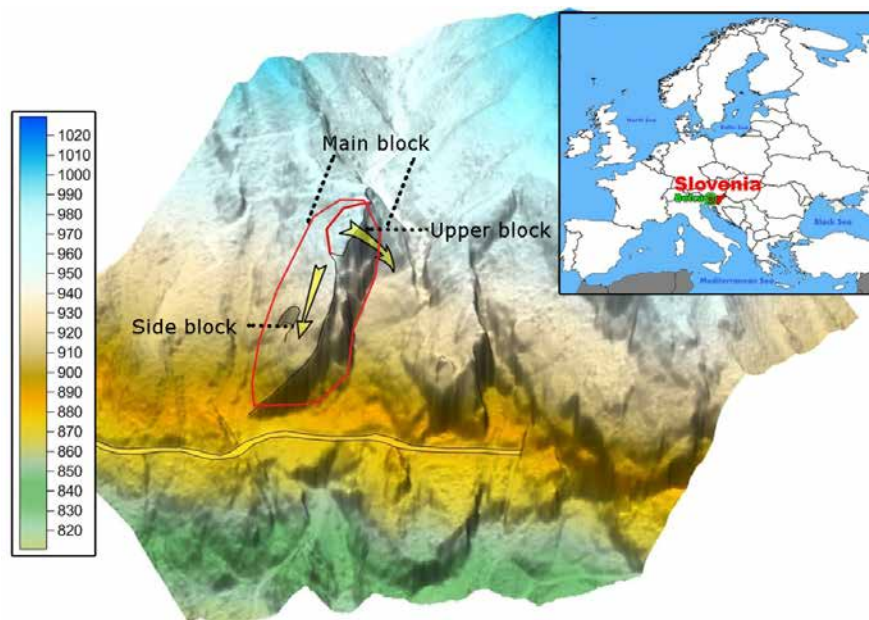


Figure 1. The researched area, view towards the northeast. The construction of the terrain is from lidar data from 2014. Indicated are the main directions of the potential falling and the main fallen blocks of the slope.

After the rockfall in autumn 2014, the area of the road was completely covered by rock to a length of 45–50 m. The waterways of the unnamed stream were also completely ruined.

There were many activities during the redevelopment that provide a safe commute on the forest road:

- Transportability of the road was provided by widening the road. On the wider road rubble and smaller stones can be stopped on the inner part of the road.
- Monitoring during the construction works was also carried out to determine the size of the movement and alert the working crew. With the monitoring, an estimation of the stability of the entire rock block was also achieved.

2 MATERIALS AND METHODS USED

The main methods for monitoring the rock block consisted of:

- Visual monitoring of the rock block;
- Installing and recording the six measuring points on the slope;
- Installing extensometers on the cracks.

We broadened our monitoring based on the knowledge we acquired while constructing the monitoring system and measuring:

- Using an unmanned aircraft,
- Recording the rock block with terrestrial laser scanning.

2.1 Visual observations

The visual observations are based on geological field overviews [19, 20]. Based on these visual observations, we concluded the following:

- The main part of the material has fallen off (and will probably continue to fall off) the upper part, which is limited by clear rupture cracks. This applies to the so-called upper block;
- We mapped the area that fell off in autumn 2014. It is located on the upper block; the volume of the fallen material is estimated to be 5,000–10,000 m³ (rough estimate).

On the opposite side of the upper block, a larger volume of rock fell off (estimated at 300 m³) a few years before. Open cracks are clearly visible in this area. We named this area the side block.

Given the incursions of major discontinuities, we decided for two potential ways of material falling: falling of the upper block, or the possibility of another rockfall of the whole block from the ridge to the road. The volume of the entire block was estimated at 150,000 m³.

The area is very dangerous for the observation at some points of the terrain change. Some areas are also very hard to reach, even with mountain-climbing equipment. There-

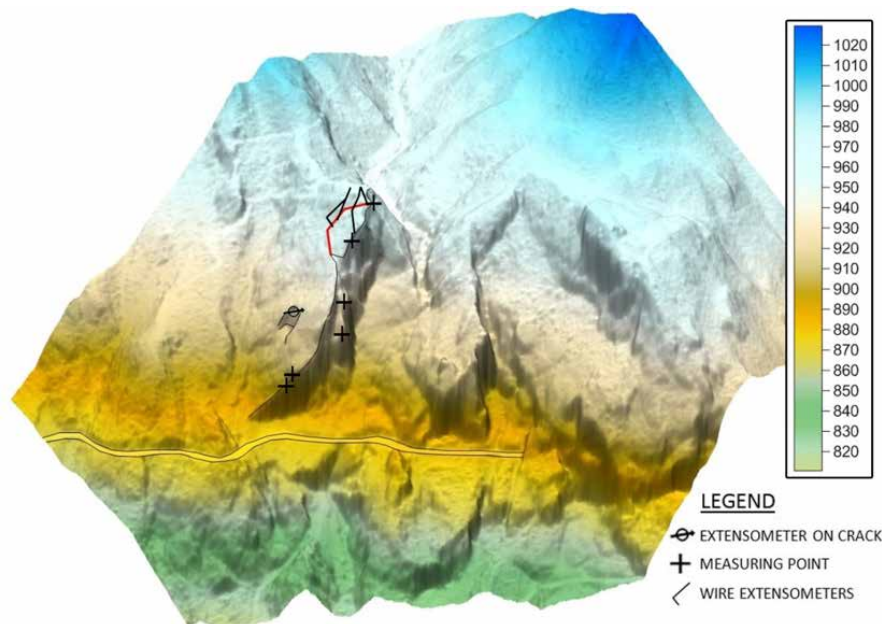


Figure 2. The positions of the extensometers and measuring points in the rock block Belca. The crack that limits the main block is pictured with red.



Figure 3. Left: schematic position of the wire extensometers, based on the upper block and based on the potential direction of movement; Right: a double and triple extensometer.

fore, we used an unmanned aircraft to observe the dangerous and hard-to-reach areas. We captured over 400 aerial photographs. Based on aerial photogrammetry, the aerial photographs were later evaluated. The result is a photo-realistic 3D model of the observed rock block, where the rock block can be viewed from any given perspective. The usability is mainly found in a better spatial orientation of the rock block and in finding a comprehensive image, which makes predicting possible outcomes easier.

2.2 Geotechnical surveying

For the verification and quantification of the absolute movements of the rock block, several measuring techniques were used [21, 22, 23]. We installed geotechnical surveying instruments on the cracks, i.e., wire extensometers. We used tacheometry, which we supplemented with terrestrial laser scanning.

- The widening of the cracks on the main block was measured with five wire extensometers, and a wire extensometer with a clock on the side block,

- The whole rock block was measured at six measuring points, installed at several points on the slope: two points on the upper block, with which we assess the possibility of a rockfall of the side block, and four points, with which the stability of the entire rock block is controlled.

2.2.1 Wire extensometers

Wire extensometers were installed on five characteristic parts of the cracks that limit the upper rock block. They were used to transmit the potential movements on the block. We used invar wires, which largely compensated for the influence of temperature.

The measurements were carried out periodically. The results are shown in the table 1, as well as pictured in Figure 4.

The increased increment in 2017 is clearly visible. If we understand the values that are increasing or declining in a *trend* as values worth using, we can state the following:

- *Triple left* is increasing at a constant rate and reaches a value of 2.7 cm. We can conclude that the north

Table 1. Wire-extensometer measurements.

date	DOUBLE				TRIPLE					
	left	diff. left	right	diff. right	left	diff. left	middle	diff. middle	right	diff. right
19. 11. 2015	245.8		245.8				134.1		131.5	
04. 12. 2015	245.8	0.0	245.8	0.0	134.4	-0.1	134.1	0.0	133.0	1.5
22. 01. 2016	245.7	-0.1	246	0.2	135.0	0.5	133.8	-0.3	130.5	-1.0
10. 06. 2016	244.5	-1.3	245.5	-0.3	136.5	2.0	136.0	1.9	116.8	
13. 10. 2016	243.5	-2.3	245.5	-0.3	137.0	2.5	107.0	-27.1	117.0	0.2
27. 10. 2016	243.5	-2.3	245.5	-0.3	137.0	2.5	106.0	-28.1	117.5	0.7
29. 05. 2017	250.8	5.0	248.0	2.2	137.2	2.7	108.0	-26.1	128.0	11.2

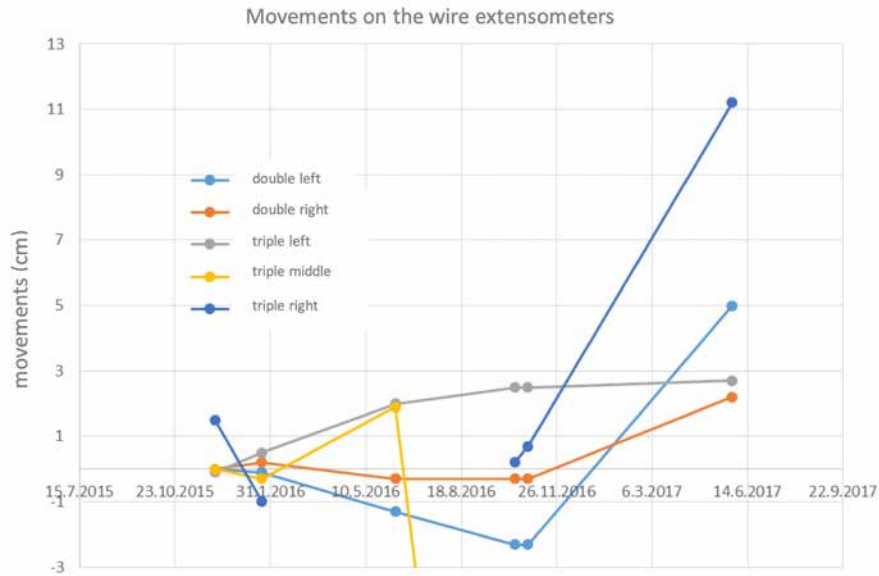


Figure 4. Graph of movements on the wire extensometers.

part of the rock block is moving towards the south at a constant speed.

- *Double left* and *triple right* increased to 5 and 11.2 cm in 2017; therefore, the rock block is moving away from the crack.
- A sudden value change for the extensometer *triple middle* also stands out. The point is directly above a turning point of the slope into a rocky overhang. Therefore, the slope can be so loose that the anchor holding the measuring wire gives way.

An extensometer for measuring the spreading of the larger crack of the rock is placed on the side block (the measuring scale shows movements of up to 65 mm).

The value increased to 5 mm between January and June 2016, after that (between June and November 2016) the value was constant. Between November 2016 and May 2017 the value increased to 11 mm.

2.2.2 Geolocating

We have installed six fixed measuring points using a classic polar method (tacheometry) in the most prominent areas as a part of the observational methods. They were labelled from T1 to T6:

- T1, T2 on the front edge of the rock block; these two points are used to measure the movement of the entire rock block,



Figure 5. Left: view of the extensometer in September 2015; Middle: view of the extensometer in June 2016; Right: view of the extensometer in May 2017. The difference is 11.0 mm. The increase of the value occurred between January and June 2016 (5 mm), as well as between November 2016 and May 2017 (6 mm).

Table 2. Coordinates of points in different epochs.

Measure- ment point	02.09.2015			11.11.2015			28.10.2016		
	X [m]	Y [m]	h [m]	X [m]	Y [m]	h [m]	X [m]	Y [m]	h [m]
T1	416724.048	149131.063	909.662	416724.050	149131.061	909.651	416724.060	149131.057	909.647
T2	416726.666	149133.189	917.702	416726.670	149133.185	917.693	416726.677	149133.175	917.688
T3	416742.017	149171.512	944.830	416742.023	149171.511	944.821	416742.046	149171.508	944.811
T4	416732.672	149181.141	964.918	416732.683	149181.143	964.911	416732.715	149181.150	964.898
T5	416713.598	149207.500	998.636	416713.612	149207.509	998.613	416713.694	149207.539	998.557
T6	416710.956	149234.294	1016.681	416710.978	149234.306	1016.651	416711.081	149234.357	1016.561

- T3, T4 on the side slope, where no distinct movement is expected; they are also used to control the movement of the entire rock block,
- T5 in the middle of the upper rock block; the point is used to monitor the movement of the upper block,
- T6 on the first parts of the upper rock block; this point is used to monitor the movement of parts above the upper block.

Three periodic measurements using a classic polar method (tachymetry) were made in 2015 and 2016. The accuracy of the measurements is 1 cm. The results are shown in the table 2.

2.2.3 Terrestrial laser scanning and airborne laser scanning

The area of the Belca rockfall was scanned with an airborne laser in 2014. This is how, using publicly

accessible lidar data through the eVode portal (<http://evode.arso.gov.si/>), we managed to consider the state of the surface before the rockfall. We managed to do that, because the airborne laser scanning of Slovenia was carried out in the summer of 2014 in that area. We made a digital model of the relief (DMR) with a spatial resolution of 50 cm using the lidar data. Because some details remained hidden (vertical beams of reflection) while scanning and recording from the air (helicopter), we carried out a terrestrial laser scanning of the area from the first measurement on. Doing this we automatically obtained many points from the laser-beam reflections:

- Measurements from 13.7.2015 have 142.4 million points,
- Measurements from 11.11.2015 have 129.1 million points,
- Measurements from 28.10.2016 have 145.5 million points.

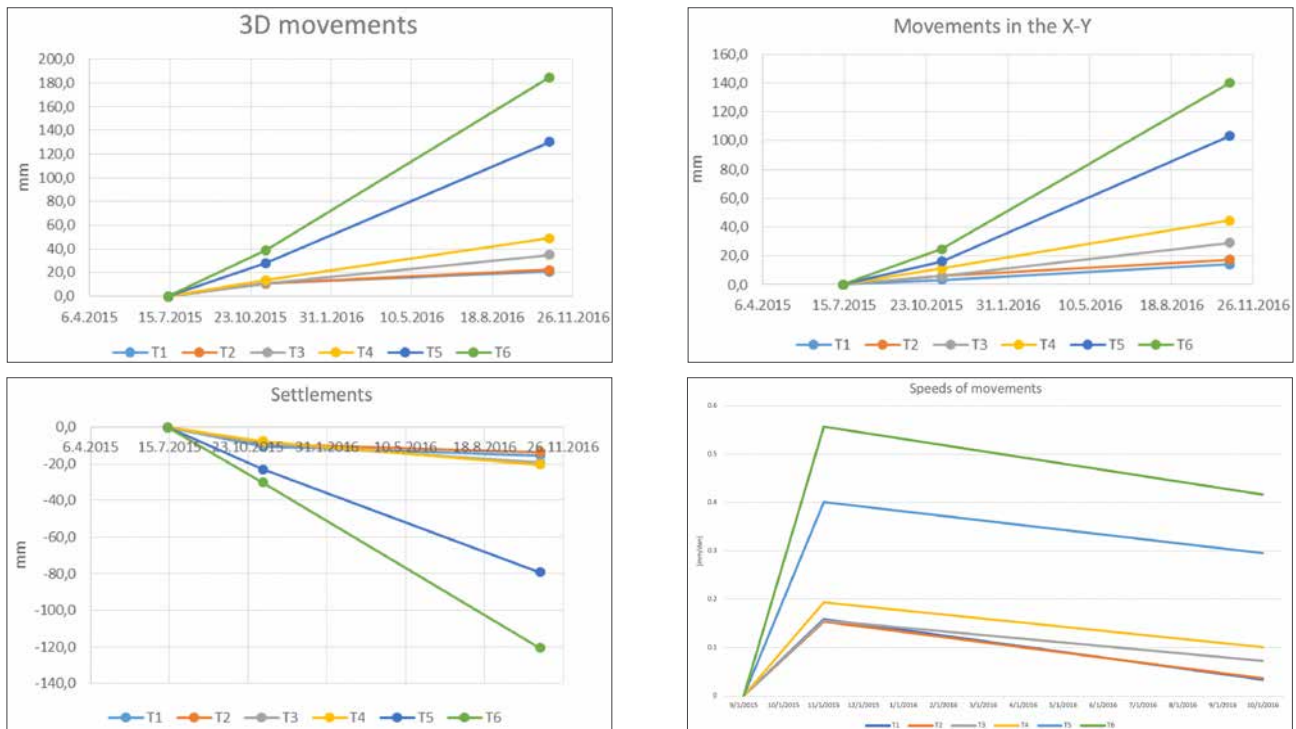


Figure 6. Graphs: size of movements – absolute (top left) and in the X-Y plane (top right); settlements (bottom left) and speeds of movements (bottom right).

The relevant data used in the further implementation is acquired from these points using a variety of software tools. We use these to:

- construct 3D models of the terrain,
- determine the movement by comparing the point clouds of different periods of recording time.

3 RESULTS

3.1 Observation results

Based on two or more periodic measurements of the observations of stabilized measurement points on the rock block with a classic polar method, we determined the size of the spatial movements of the object. Next, based on three or more periodic measurements, we determined the speed of the movements. The analysis of the results is shown in the graphs in Figure 6 (previous page).

The graphs show that the points in the upper part (T5 and T6) clearly stand out while looking at the sizes of the movements. This indicates the intensity and ever-present events on and near the upper rock block. The movement direction clearly shows the possibility of further rockfall around the upper rock block. The values of the other points (T1–T4) also show the movement of the block.

Changes are clearly seen on the upper block and around the lower spree (Figure 8 shows the colour scale going towards

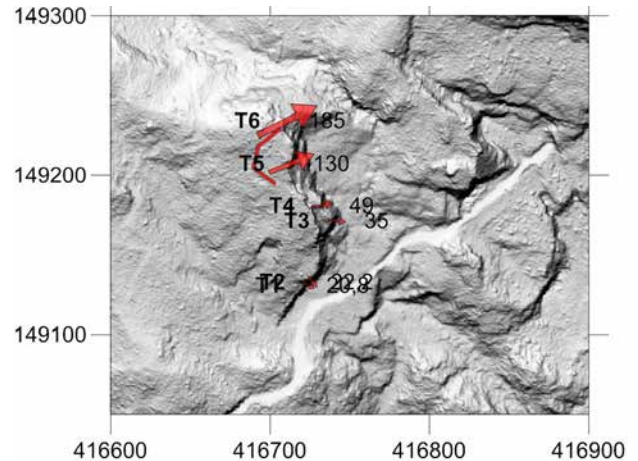


Figure 7. The position and labelling of the measurement points on the rock block. The arrows proportionally show the directions of movement, while the values of the absolute movements between July 2015 and October 2016 are shown on the right-hand side.

red) while comparing the point clouds accumulated with terrestrial laser scanning from 11.11.2015 and 28.8.2016. We attribute the other changes (on the left- and right-hand sides of the figure) to the influence of the vegetation.

3.2 Data analysis of the airborne laser scanning and the terrestrial laser scanning

Airborne laser scanning of the surface was conducted within the LIDAR survey of Slovenia in the summer

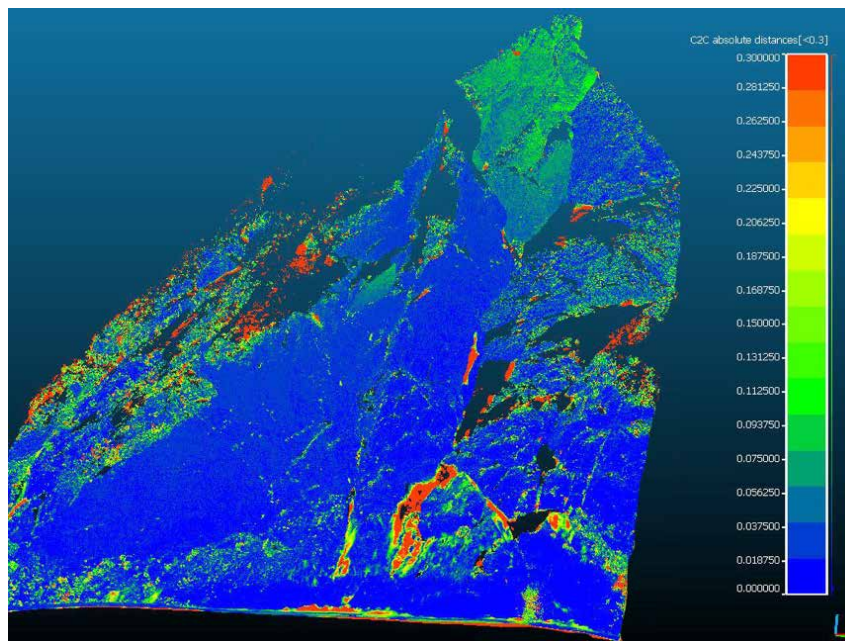


Figure 8. Differences between the terrestrial laser scanning on 11.11.2015 and on 28.8.2016.

of 2014, so a few months before the rockfall in the autumn. This gave us the chance to compare the data from before and after the rockfall. The difference in its surface is visible when comparing the inclination maps (Figure 9).

The biggest fallen block of rock measures approximately 90 m x 20 m in layout dimensions, and is 33 m in height. Based on the 3D analysis of the difference between the surfaces in 2014 and 2015, we have defined the volume of the fallen rock, which measures 6,700 m³.

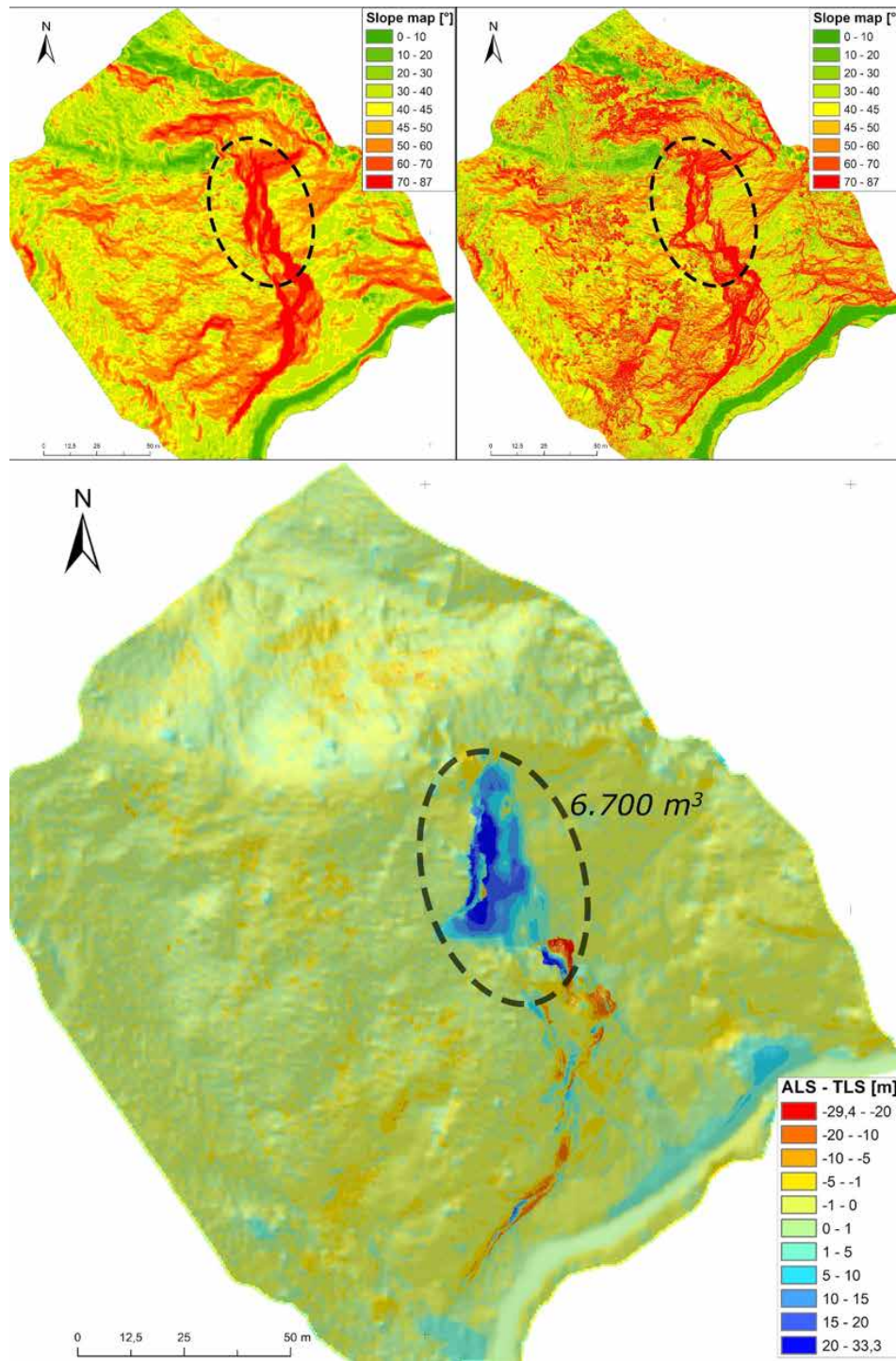


Figure 9. Top left: a relief of the surface, made based on ALS data (summer 2014); Top right: a relief of the surface, made based on TLS data (summer 2015); Bottom: The volume differences.

4 DISCUSSION

4.1 A visualisation of the events and projections into the future

Based on the field survey, measurements and detailed reviews of the measured results, we can conclude that the rock block above the forest road in Belca is still moving. Based on the measurements so far, we can also conclude that the values in the upper block are within 10–20 cm per year.

Often, a graph of the reverse velocity and time values is used to estimate the launching time of a landslide. The launch time is the time when the value of the speed-1 is approaching 0. In the case of all the points from T1 to T6, the values do not asymptotically fall towards the value 0 (Figure 10). However, we must warn of the fact that the upper block is made up of pieces of dolomite, which are clearly separated between themselves with open cracks. Therefore, the falling of free blocks can still occur. Moreover, the conclusions are derived from three series of measurements, which can be a too small number of repetitions for a credible assessment.

In the case of the rock block Belca, we are interested in two things:

- The possibility of more rockfall in the upper block and the consequences of it falling onto the road.
- The possibility of the whole block falling and making its way towards the valley of the river Belca.

4.2 The possibility of rockfall in the upper block and the consequences of rockfall to the road

Smaller rockfall of the slopes and greater filling of the road with the rockfall also occur after repair work. A

10-m road segment is especially at risk. Despite the roadway being wide in this part, the road is also hit with single larger pieces of stones, with dimensions of up to a few decimetres. This area requires constant cleaning of the roadway. Because the area is relatively well shrouded, the potentially dangerous stones can be controlled by a catch fence at the bank above the road.

4.3. Basic and derived measurements

With the basic examination of the terrain, a first picture of the events is made. This picture is then upgraded with new findings and new methods of work: basic recording of data was updated to terrestrial laser scanning, with which we can create a spatial assessment of the fallen block, as well as an assessment of the spatial spreading of the block. The picture of the event was completed by recording with an unmanned aircraft.

5 CONCLUSION

The measurements indicate that the rock block is still in motion, being 10–20 cm/year at the upper part.

We have calculated the volume of the fallen rock (the volume of the rockfall in September 2014) using a 3D deformation analysis of the state of the rock before and after the rockfall.

There is a risk of a rockfall for the whole block of rock in the direction of the river Belca, in the worst case damming the river with the rockfall material. To assess the possibility of the further falling of either parts of the rock block (upper block) or the whole rock block, it is necessary to continue the monitoring process and adapt it per the results.

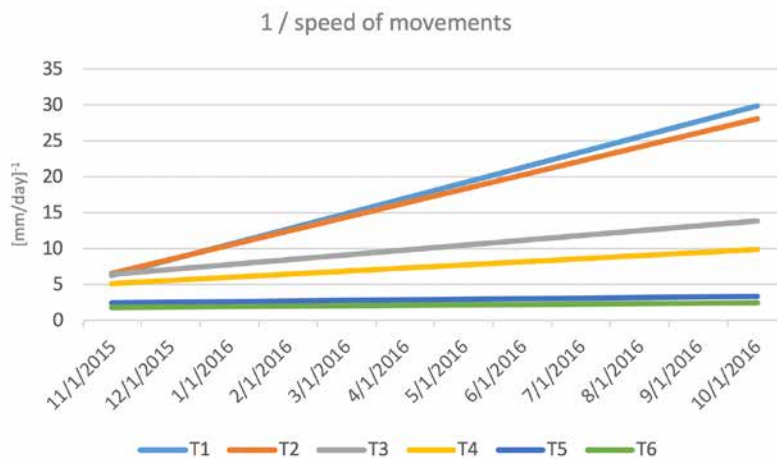


Figure 10. Projection graph of the reverse speed values.

In the monitoring process, the use of UAV flights is extremely useful in surveying the rock block. The entire block can be reconstructed and hidden details can be clearly visible. Due to a difficult visual surveying approach, which is also very dangerous, the use of UAV can become a standard tool in such operations. The only disadvantage is the low GPS positioning of the device due to the narrow, hilly terrain, which prevents a good signal.

Acknowledgment

We would like to thank the companies Geotrias d.o.o. and Magelan Group Ltd., which provided us with access to the collected data. We would also like to thank the municipality of Kranjska Gora for their engagement with the issues in Belca.

REFERENCES

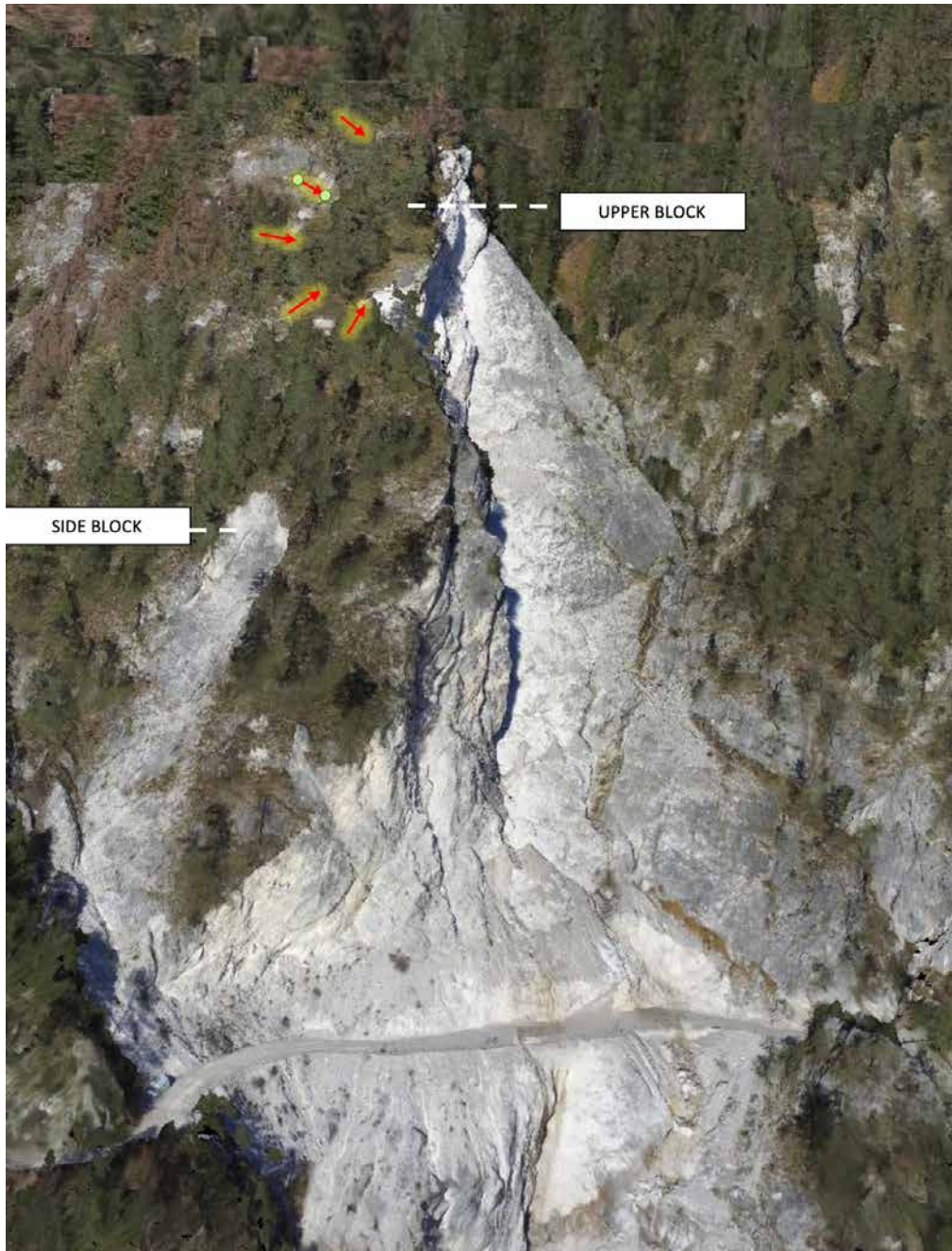
- [1] Scaioni, M., Arosio, D., Longoni, L., Papini, M., Zanzi, L. 2008. Integrated Monitoring and Assessment of Rockfall. V: Proceedings from International Conference on Building Education and Research, Kandalama, Sri Lanka, 10. - 15. February 2008: pp. 618-629.
- [2] Teza, G., Marcato, G., Pasuto, A., Galgaro, A. 2015. Integration of laser scanning and thermal imaging in monitoring optimization and assessment of rockfall hazard: a case history in the Carnic Alps (Northeastern Italy). *Natural Hazards* 76, 3: 1535-1549. doi: 10.1007/s11069-014-1545-1
- [3] Gordon, S., Lichti, D., Stewart, M. 2001. Application of a high-resolution, ground-based laser scanner for deformation measurements. V: The 10th FIG International Symposium on Deformation Measurements, Orange, California, USA, 19. - 22. March 2001: pp. 23-32.
- [4] Gordon, S., Lichti, D., Stewart, M., Franke, J. 2003. Structural deformation measurement using terrestrial laser scanners. V: 11th FIG Symposium on Deformation Measurements, Santorini, Greece, 5. - 28. May 2003: pp. 8.
- [5] Alba, M., Fregonese, L., Prandi, F., Scaioni, M., Valgoi, P. 2006. Structural monitoring of a large dam by terrestrial laser scanning. V: ISPRS Commission V Symposium 'Image Engineering and Vision Metrology', Dresden, Germany, 25. - 27. September 2006.
- [6] Schneider, D. 2006. Terrestrial laser scanning for area based deformation analysis of towers and water dams. V: 3rd IAG / 12th FIG Symposium, Baden, Austria, 22. - 24. May 2006.
- [7] Tsakiri, M., Lichti, D., Pfeifer, N. 2006. Terrestrial Laser Scanning For Deformation Monitoring. V: 3rd IAG / 12th FIG Symposium, Baden, Austria, 22. - 24. May 2006: pp. 1-10.
- [8] Gordon, S.J., Lichti, D.D. 2007. Modeling Terrestrial Laser Scanner Data for Precise Structural Deformation Measurement. *Journal of Surveying Engineering* 133, 2, 72-80. doi: 10.1061/(ASCE)0733-9453(2007)133:2(72)
- [9] Bu, L., Zhang, Z., Scanning, L., Cloud, P., Modeling, S. 2008. Application of point clouds from terrestrial 3d laser scanner for deformation measurements. V: XXI. ISPRS Congress, Beijing, China, 3-11 July, 2008, pp. 545-548.
- [10] Lovas, T., Barsi, A., Detrekoi, A., Dunai, L., Csak, Z., Polgar, A., Berenyi, A., Kibedy, Z., Szocs, K. 2008. Terrestrial laser scanning in deformation measurements of structures. V: XXI. ISPRS Congress, Beijing, China, 3. - 11. July 2008, pp. 527-532.
- [11] Monserrat, O., Crosetto, M., Pucci, B. 2008. TLS deformation measurement using LS3D surface and curve matching. V: XXI. ISPRS Congress, Beijing, China, 3. - 11. July 2008, pp. 591-595.
- [12] Qiu, D.W., Wu, J.G. 2008. Terrestrial laser scanning for deformation monitoring of the thermal pipeline traversed subway tunnel engineering. V: XXI. ISPRS Congress, Beijing, China, 3. - 11. July 2008, pp. 491-494.
- [13] Zogg, H.M., Ingensand, H. 2008. Terrestrial laser scanning for deformation monitoring - load tests on the Felsenau viaduct. V: XXI. ISPRS Congress, Beijing, China, 3. - 11. July 2008, pp. 555-562.
- [14] Berényi, A., Lovas, T., Barsi, Á., Dunai, L. 2009. Potential of terrestrial laserscanning in load test measurements of bridges. *Periodica Polytechnica Civil Engineering* 53, 1, 25. doi: 10.3311/pp.ci.2009-1.04
- [15] Vežočnik, R., Ambrožič, T., Sterle, O., Bilban, G., Pfeifer, N., Stopar, B. 2009. Use of terrestrial laser scanning technology for long term high precision deformation monitoring. *Sensors* 9, 12, 9873-95. doi: 10.3390/s91209873
- [16] Abellán, A., Calvet, J., Vilaplana, J.M., Blanchard, J. 2010. Detection and spatial prediction of rockfalls by means of terrestrial laser scanner monitoring. *Geomorphology* 119, 3-4, 162-171. doi: 10.1016/j.geomorph.2010.03.016
- [17] De Asís López, F., Ordóñez, C., Roca-Pardinas, J., García-Cortés, S. 2014. Point cloud comparison under uncertainty. Application to beam bridge measurement with terrestrial laser scanning. *Measurement* 51, 1, 259-264. doi: 10.1016/j.measurement.2014.02.013
- [18] Harmening, C., Neuner, H. 2015. Continuous

modelling of point clouds by means of freeform surfaces. *Vermessung & Geoinformation* 103, 2+3, 121-129.

- [19] Koren, E., Vižintin, G. 2015. Idrisi as a tool for slope stability analysis = Idrisi kot orodje za analizo stabilnosti pobočij. *RMZ - Materials and geoenvironment* 62, 2, 95-104.
- [20] Vižintin, G., Mayer, J., Lajlar, B., Vukelič, Ž. 2017. Rock burst dependency on the type of steel arch support in the Velenje mine = Hribinski udari v

odvisnosti od vrste jeklenih podpornih lokov v premogovniku Velenje. *Materiali in tehnologije* 51, 1, 11-18.

- [21] Vižintin, G., Stevanovič, L., Vukelič, Ž. 2008. Development of environmental criteria for estimation of land development using GIS = Uporaba GIS-a za določitev naravnih kriterijev možnosti okoljskega razvoja. *RMZ - Materials and geoenvironment* 55, 2, 237-258.
- [22] Vižintin, G, Viršek, S. 2008B. Analytical surface



Appendix 1. Frontal view

water forecasting system for Republic of Slovenia = Analitičen sistem napovedovanja pretokov površinskih vod v Republiki Sloveniji. RMZ - Materials and geoenvironment 55, 2, 215-224.

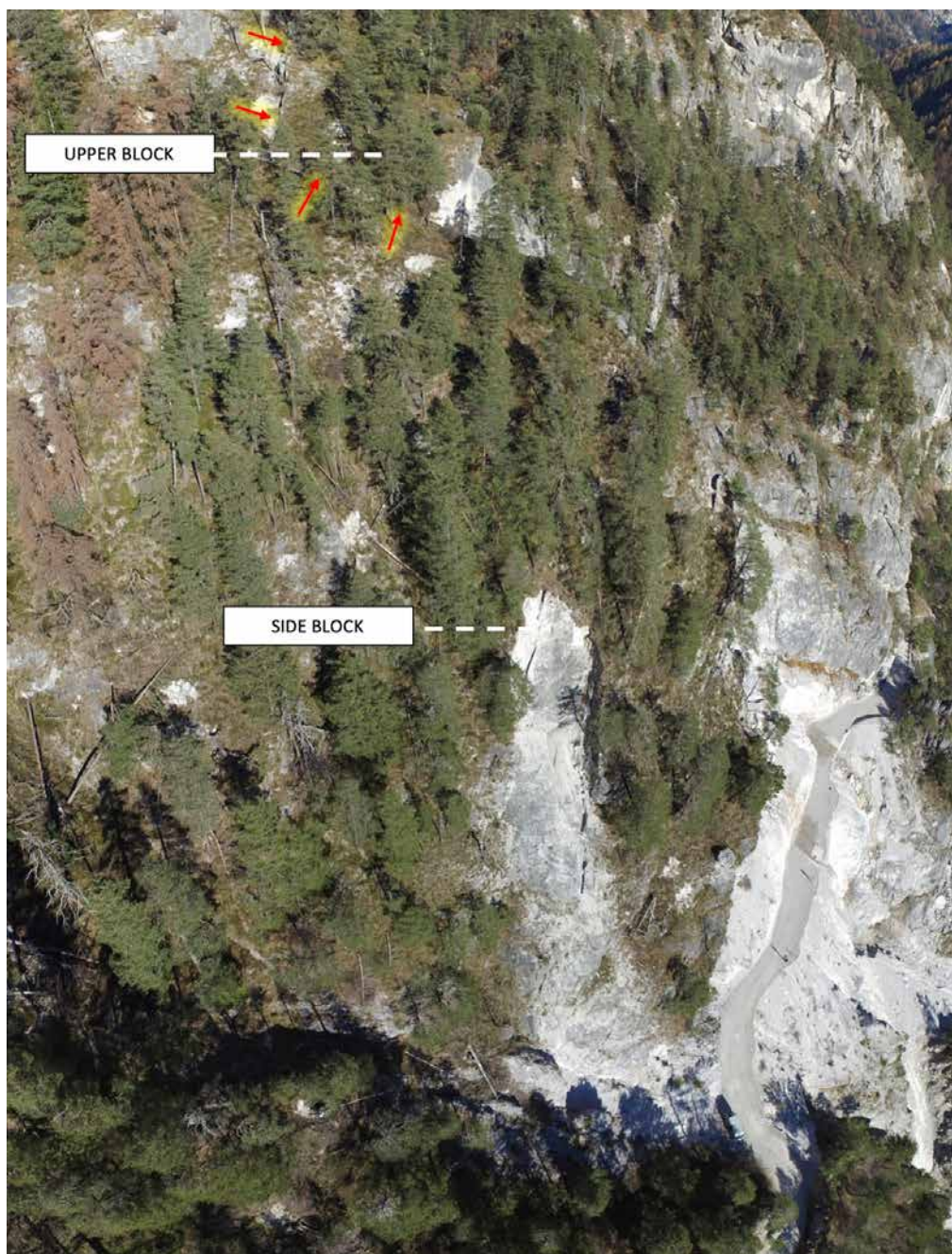
- [23] Božiček, B., Lojen, S., Dolenc, M., Vižintin, G. 2017. Impacts of deep groundwater monitoring wells on the management of deep geothermal Pre-Neogene aquifers in the Mura-Zala Basin, Northeastern Slovenia. Groundwater for sustainable development 5, 193-205.

APPENDICES

- Frontal view
- View towards the east
- View towards the west
- Top view



Appendix 2. View towards the east



Appendix 3. View towards the west



Appendix 4. Top view

S_BRICK: A CONSTITUTIVE MODEL FOR SOILS AND SOFT ROCKS

S_BRICK: KONSTITUTIVNI MODEL ZA ZEMLJINE IN MEHKE KAMNINE

Vladimir Vukadin

Institute for Mining, Geotechnology and Environment (IRGO)
Slovenčeva 93, 1000 Ljubljana, Slovenia

Vojkan Jovičić (corresponding author)

Institute for Mining, Geotechnology and Environment (IRGO)
Slovenčeva 93, 1000 Ljubljana, Slovenia
E-mail: vojkan.jovicic@irgo.si

DOI <https://doi.org/10.18690/actageotechslov.15.2.16-37.2018>

Keywords

structure, constitutive material models, soft rocks and hard soils, numerical modelling, destructuring

Ključne besede

struktura, konstitutivni materialni modeli, mehke kamnine in trde zemljine, numerično modeliranje, destrukturizacija

Abstract

Materials known in the literature as hard soils and soft rocks are widely spread, natural materials that are commonly encountered in engineering practise. It was demonstrated that some of these materials can be described through the general theoretical framework for structured soils set by Cotecchia and Chandler [14], which takes into account the structure as an intrinsic property present in all natural geological materials. Based on laboratory results and existing theoretical frameworks, the development of a constitutive model for structured materials was carried out. The model formulated in strain space named BRICK [27, 29] was chosen as the base model and was further developed by adding features to model both the structure and the processes of destructuring. The new model was named S_BRICK and was first presented on a conceptual level, in which the typical results of modelling structured and structureless (reconstituted) materials on different stress paths were compared within the solutions of the Cotecchia and Chandler [14] theoretical framework. The S_BRICK model was validated on three materials, i.e., Pappadai clay, North-Sea clay and Corinth marl, thus covering a wide range of natural, structured materials. The results showed that S_BRICK was able to successfully model the stress-strain behaviour typical for hard-soil and soft-rock materials, in general.

Izvleček

Materiali, ki so poznani v literaturi kot trde zemljine ali mehke kamnine, so široko razširjeni naravni materiali pogosto prisotni v inženirski praksi. Pokazano je, da se določeni tovrstni materiali lahko opišejo s pomočjo teorijskega okvirja za strukturirana tla, ki so ga razvili Cotecchia in Chandler [14], in sicer na ta način, da so upoštevali notranjo strukturo, ki je prisotna v vseh naravnih geoloških materialih. Razvoj konstitutivnega modela za strukturirane zemljine je bil narejen na podlagi rezultatov laboratorijskih raziskav in z uporabo obstoječih teorijskih okvirjev. Konstitutivni model BRICK [27, 29], ki je bil razvit v prostoru relativnih deformacij, je bil izbran za osnovni model in je nadgrajen z dodatnimi lastnostmi, da bi bil lahko uporaben za modeliranje strukture in tudi procesa destrukturizacije. Novi model, imenovan S_BRICK, je najprej predstavljen na konceptualnem nivoju, v katerem so tipični rezultati modeliranja strukturiranih in ne-strukturiranih (rekonstituiranih) materialov primerjani z rešitvami iz Cotecchia in Chandler-ovega [14] teorijskega okvirja. Model S_BRICK je validiran na tri materiale: pappadaiska glina, glina iz severnega morja in korintski lapor. Na ta način je validacija modela zajela široki razpon naravnih materialov. Rezultati so pokazali, da model S_BRICK lahko uspešno modelira napetostno-deformacijsko obnašanje, ki je tipično za trde zemljine ali mehke kamnine.

1 INTRODUCTION

The BRICK model, developed by Simpson [27, 29] for overconsolidated clays, was chosen to be the base model for the development of the constitutive model called S_BRICK, aiming to model structured materials such as hard soils and soft rocks. This was mainly due to the BRICK model's ability to model the non-linear, stress-strain response of soil and the recent stress-history effect [5], which are both the main features of the mechanical behaviour characterised by kinematic hardening.

In the first part of the paper the framework for structured soils developed by Cotecchia and Chandler [14] is presented together with a brief description of the original BRICK model. This is followed by an explanation of the S_BRICK model formulation, in which the additional features are given to account for the influence of the structure on the mechanical behaviour of natural materials. A particular feature of the S_BRICK model is its ability to model destructure. It was soon understood that the modelling of structured natural materials could not be successful without taking into account the processes of structure decay following the plastic deformation. The methodology of modelling destructure in S_BRICK is explained and the parameter determination procedure is given on a conceptual level.

Finally, the validation of the S_BRICK model was carried out on three natural materials: Pappadai clay, North-Sea clay and Corinth marl. While the Pappadai clay and the North-Sea clay are heavily overconsolidated clays and can be classified as hard soils, Corinth marl is a typical representative of soft rock, with a complex geological history and the resulting mechanical properties. Those three materials were chosen to demonstrate the ability of S_BRICK to cover the main features of the mechanical behaviour of a wide range of natural, structured materials.

2 THEORETICAL BACKGROUND

2.1 Structured materials

Kavvas [21] and Kavvas and Anagnostopoulos [22] suggested that the principles of soil mechanics could be applied to the modelling of hard soils and soft rocks as long as the behaviour of the natural material is not influenced significantly by large-scale discontinuities. It is widely accepted that, apart from including the important features of the mechanical behaviour of soils, such as nonlinearity, small strain stiffness and the influence

of volumetric and kinematic hardening, a constitutive model has to include the effects of structure and destructuring in order to describe the behaviour of natural geological materials [25, 10, 14, 23, 26, 7, 16, 2, 17, 11].

The origins of the structure in natural soils are complex and can be attributed to different processes and different physical and chemical conditions during and after sedimentation. Hence, there are many different classifications and definitions that take into account the different aspects of structure. Lambe and Whitman [24] stated that structure is a combination of the fabric and the bonding in which the fabric represents the arrangement of the soil particles and the bonding represents the chemical, physical or any other types of bonds between the particles. Bonding has predominant effects in rocks, while in soils the influence of fabric is more important. It is obvious that according to this definition, structure is present in both natural and reconstituted geological materials, because no matter how much material is remoulded or destructured, it still has some type of fabric. Nevertheless, from the mechanical point of view, the influence of structure in reconstituted materials is the benchmark reference state representing the lower bound for the strength and the stiffness of natural materials.

An example of the influence of structure on state boundary surfaces (SBSs) for undisturbed, partly destructured and reconstituted Pappadai clay is shown in Figure 1 (after Cotecchia and Chandler [14]). It can be seen in the q/p' diagram (p' is mean effective stress and q is the deviator stress) normalized with the mean effective stress p'_e (taken at an isotropic reconstituted normal compression line at the same specific volume as for the intact clay) that the influence of structure is manifested by the size of the SBSs, resulting in the higher strength and stiffness of the undisturbed material in comparison with the partly destructured or reconstituted Pappadai clay. Cotecchia and Chandler [14] and Kavvas and Anagnostopoulos [22] and the other authors differ on the classification and the mechanisms of the structure development, but they all nevertheless agree that the position of the in-situ state in volumetric space, i.e., the distance of the yield stress from the intrinsic compression line, controls the compression and the strength behaviour of natural soils. The intrinsic compression line here refers to the properties of reconstituted materials, representing the lower bound for the normal compression lines of natural materials.

The key element of the structure is stability, as Baudet [6] and Baudet and Stallebrass [7] emphasise, so that the stable structure is predominantly governed by the fabric, while the unstable structure is predominantly

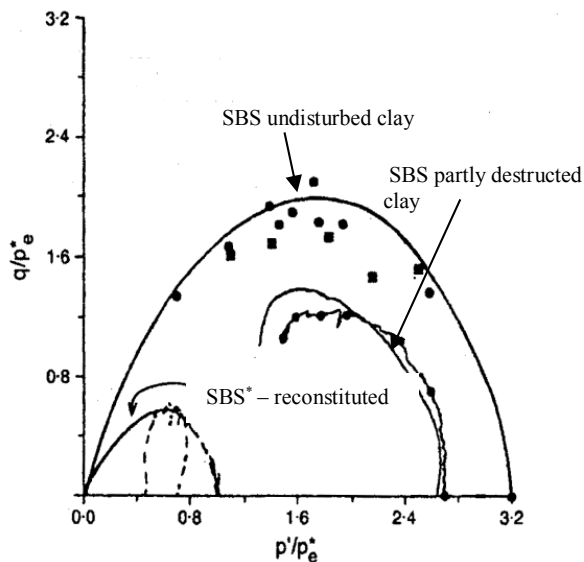


Figure 1. Influence of the structure on the SBS of undisturbed, partly destructured and reconstituted Pappadai clay (after Cotecchia & Chandler, [14]).

governed by the bonding. Destructuring is caused by the plastic straining and is responsible for the decreasing of the SBS, as shown in Figure 1, and thus a reduction in the strength and the stiffness of the natural soil. The materials that show a certain degree of destructuring are classified as meta-stable, in which both elements of the structure (fabric and bonding) are still present. According to Leroueil and Vaugan [25], yielding and hence the plastic straining, causing destructuring can result by

following shearing, compression and swelling stress paths inside the SBS. However, these mechanisms of destructuring are still not fully understood, which was and would be an obvious obstacle to the development of the models that simulate the behaviour of natural materials.

2.2 Theoretical frameworks

The proposed S_BRICK model was developed using the theoretical concepts of elasto-plasticity and critical state soil mechanics [30, 4] in a wider sense and the approach of Simpson [27] in developing the basic BRICK model. A further step in the model's development was made by using the theoretical framework for structured soils developed by Cotecchia and Chandler [14]. In this framework the influence of the structure (*S*) is quantified by the difference in the sizes of the SBSs of the structured and reconstituted materials, which are similar in shape. The framework is conceptually presented in Figure 2 in the q - p' - v space (v represents the specific volume), showing the two idealised boundary surfaces for reconstituted and structured materials. Cotecchia and Chandler [14] postulated that the parameter of shear sensitivity S_t , which is the ratio between the peak shear strengths of the natural or structured (q_{peak}) and the reconstituted material (q^*_{peak}), is equal to the parameter of stress sensitivity S_σ which is defined as the ratio of the effective stresses for natural and reconstituted soils, taken at the same specific volume for isotropic (p'_{ei}/p'^*_{ei}) or normal compression lines (p'_{eK0}/p'^*_{eK0}).

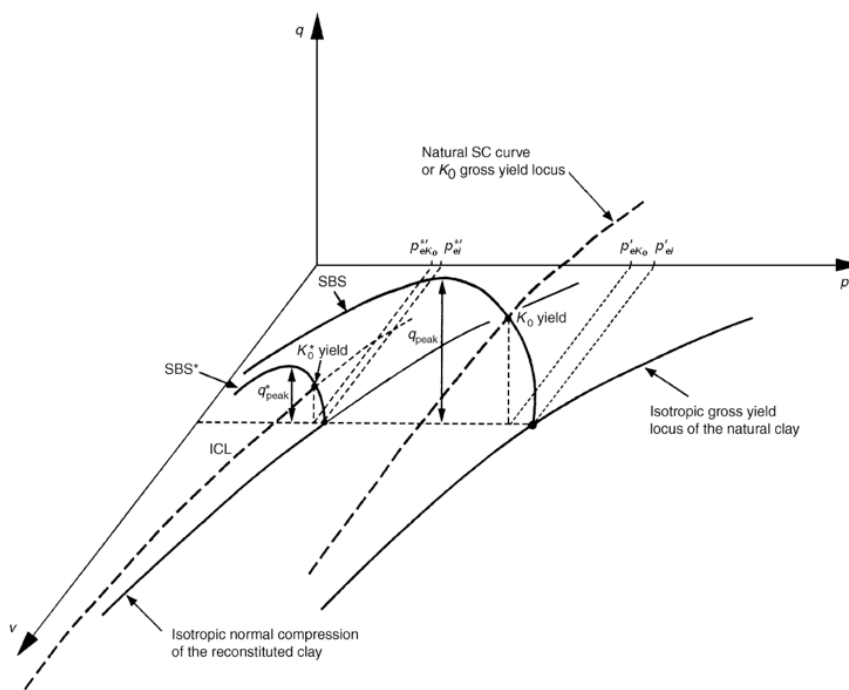


Figure 2. Theoretical framework for structured and reconstituted material in the q - p' - v space (after Cotecchia & Chandler, [14]).

The relationship is given by the following expression:

$$S = S_t = q_{peak} / q_{peak}^* = S_\sigma = p'_{ei} / p'_{ei}^* = p'_{eKo} / p'_{eKo}^* \quad (1)$$

The value of the parameter S for the reconstituted material is equal to 1; therefore, the SBSs of the reconstituted and structured materials should coincide when plotted together in the normalized space $q/(Sp'_e)^* - p'/(Sp'_e)^*$, which takes into account the structure (S) and the volume (p'_e). The framework was validated by Cotecchia and Chandler [14] for Sibari, Bothkennar and Pappadai clays. The theoretical framework was also subsequently validated by Baudet [6] and Baudet and Stallebrass [7] for different materials, ranging from soft to hard clays. Even though the data on soft rocks in the literature are not as extensive as those on soft and hard clays, there is enough evidence to suggest that the basic concepts of this theoretical framework can also be applied to soft rocks [18, 23, 1].

2.3 Basic concepts of the BRICK model

The constitutive model for the structured soils S_BRICK originates from the BRICK model developed by Simpson [27, 29]. The BRICK model was developed to model the behaviour of over-consolidated clays, but was also successfully used to model soft or normally consolidated soils. The model includes many important features of the soil behaviour, including isotropic and kinematic hardening, and can model the stress-strain nonlinearity and the recent stress-history effect [5]. The means of formulation for the BRICK model are such that it is not obvious how the BRICK model is related to the theoretical concept of critical state soil mechanics or how the model can be extended within the theoretical framework for structured soils developed by Cotecchia and Chandler [14]. An attempt is made to underline those features of the BRICK model so that the further development to the S_BRICK model can be understood. The background and the formulation of the BRICK model are given in detail by Simpson [27, 29] and a more updated version, which includes a 3D formulation, is given by Ellison et al. [15].

The BRICK model is formulated in the strain space defined by the six strain invariants ε_i ($i=1-6$) in which the first one represents the volumetric component and other five represent the deviatoric components of the strain. The main idea is explained by the analogy of bricks and strings shown in Figure 3a, in which a man (representing the current strain state) is pulling a certain, but definitive, number of bricks that are attached to him by strings of different lengths (representing the current strain path, causing a plastic deformation of different

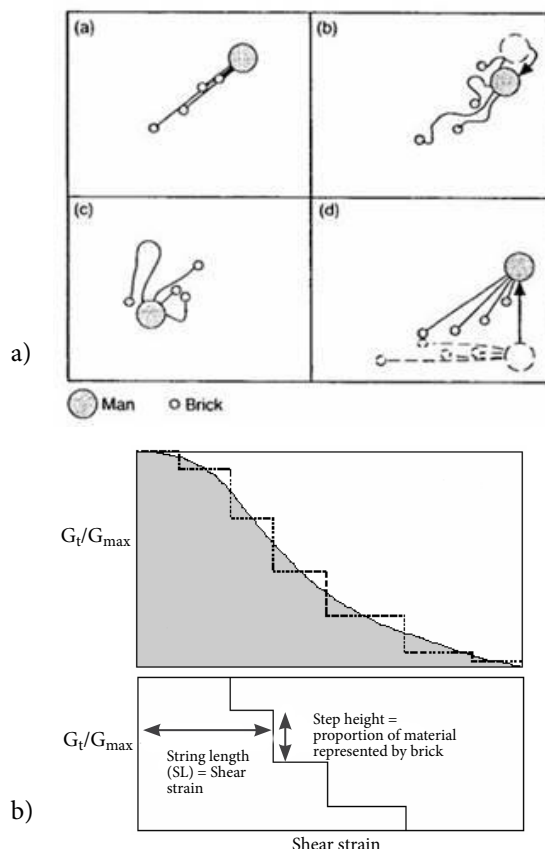


Figure 3. The concept of the BRICK model: a) brick and string analogy and b) discretization of the S-shaped curve (after Simpson, [27]).

magnitude). The analogy is essentially a way to discretise the decay of the tangent shear stiffness with the shear strain shown in Figure 3b in the shape of the normalised *S-shaped* curve. The strings (SL – string length) are given in a stepwise fashion, in which the height of each step indicates the proportion of the material being represented by a single brick. At very small strains the material is completely elastic, all the strings are slack and the bricks do not move. As the straining proceeds, the first brick starts to move, the plastic strain begins and there is a drop in the stiffness of the material. With continuous straining, more and more bricks are being pulled, there is more plasticity and there is a further drop in the stiffness until the material is fully plastic and the stiffness limits towards zero. When the stress path is changed initially, all the strings are slack, so that the immediate response is elastic. It should be noted though, that many stress paths starting from an in-situ state will not be fully elastic at small strains because some strings will remain taut. The plastic strain develops in the direction of the string orientation so that fully plastic behaviour does not occur until all the strings are all taut and aligned in the direction of the strain increment.

With the BRICK analogy, the concepts of non-linearity, recent stress history and kinematic hardening are all being accounted for. Simpson [27] also demonstrated that the area beneath the normalized *S-shaped* curve is equal to $\sin\phi'$, and thus determines the maximum angle of shearing resistance for the effective stresses ϕ' defining the strength response of the model. Simpson [28] also showed how the model could be viewed as a set of nested yield surfaces, expressed in the strain space.

The stiffness response of the BRICK model in the elastic range is accounted for by the parameter ι that represents the correlation of the elastic volumetric modulus with the mean effective stress. The *S-shaped* curve and the elastic parameter ι are additionally modified by a volumetric state parameter that accounts for the changes to the stiffness and the strength. Therefore, as for the other kinematic hardening models, the correct modelling of a stress history is of crucial importance for the correct model predictions. The state parameter ψ_B , an important feature of the BRICK model, is used to the same effect of accounting for isotropic hardening as is the overconsolidation ratio used in the theory of critical state soil mechanics. As will be explained later, the concept of state, which was defined in a similar way as proposed by Been and Jeffries [8], was used as a means to extend the BRICK model within the theoretical framework developed by Cotecchia and Chandler [14] for structured soils. The state parameter ψ_B in the BRICK model is given by the following expression:

$$\psi_B = \varepsilon_v - \varepsilon_{v0} - \lambda \ln(p' / p'_0) \quad (2)$$

In this expression, ψ_B represents the distance of the current volumetric-stress state given by p' (mean effective stress) and ε_v (volumetric strain) from the reference state

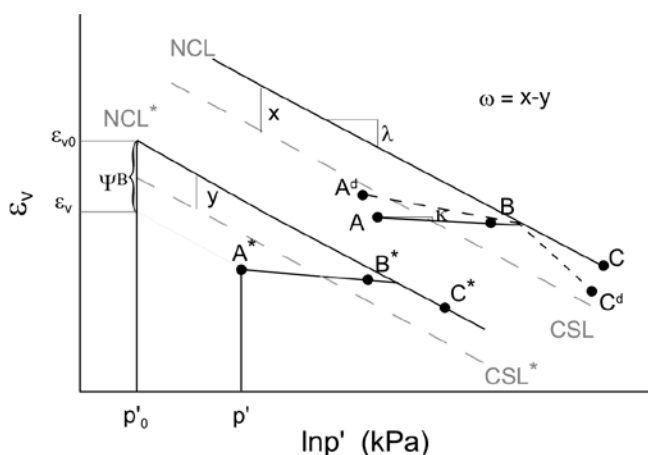


Figure 4. Concept of the state parameter ψ_B as modeled in BRICK, definition of the parameter ω , and locations of the necessary triaxial tests for the parameter determination for S_BRICK.

represented by the normal compression line defined by p'_0 , λ and ε_{v0} in the ε_v - $\ln p'$ plane, as shown in Figure 4. As it is assumed that the reconstituted material has not undergone any straining, ε_{v0} is set to zero and p'_0 is taken at the arbitrary (non-zero but small) value of 2 kPa. Simpson [27] introduced the influence of the state on stiffness and the strength using the parameter β , which he subsequently divided into two parameters, β_G and β_ϕ , so that the influence of the state on the stiffness and strength, respectively, is given by the following two expressions:

$$SL = SL_{current} \frac{(1 + \beta_\phi \psi_B)}{(1 + \beta_G \psi_B)} \quad (3)$$

$$\iota = \iota_{current} (1 + \beta_G \psi_B) \quad (4)$$

It is clear from Equation 3 that the string lengths (SLs) are influenced by both the parameters β_G and β_ϕ , which means that the influence on the stiffness and the strength is not fully decoupled. In total, the BRICK model requires eight parameters, from which five can be determined using conventional laboratory testing (λ , κ , ι , ν and the shape of *S* curve), one that can be used as a constant (μ -Drucker-Prager parameter defining the shape of a State Boundary Surface in Π -plane) and the two (β_G and β_ϕ) can be determined by back-analysing conventional laboratory tests through a trial-and-error process. It will be shown later that the values of most of the parameters fall into relatively narrow intervals, so the values given by Simpson [27, 29] for London clay, given in Table 1, could be used as suitable starting values for any other clay. Furthermore, the *S-shaped* curve, which is given in normalized form, seems to be similar for all hard-soils and soft-rock materials, which were the subject of this research, as will be demonstrated latter.

3 FORMULATION OF THE S_BRICK MODEL

The newly developed model was named S_BRICK to indicate the ability to model structured soils, while the original name was preserved, indicating that all the features of the BRICK model were preserved. A single-element program was developed as a tool for numerical simulations of soil behaviour using the S_BRICK model in 3D strain space.

3.1 Modelling of a structure

The influence of structure is accounted for by the introduction of the two new parameters α and ω . The first parameter α is used to proportionally increase or decrease the size of the string lengths (SLs) and thus of the area beneath the *S-shaped* curve. This has a direct

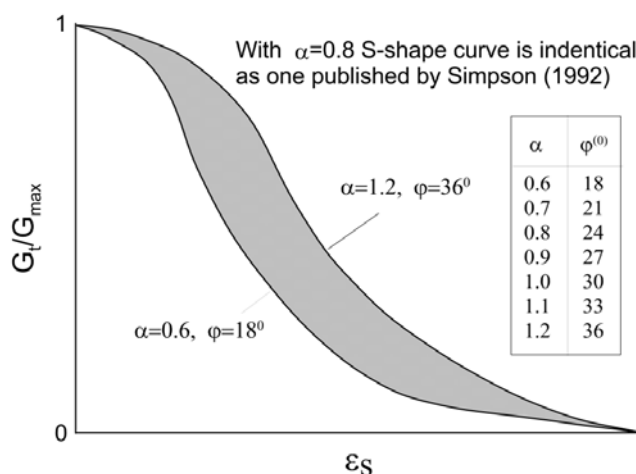
Table 1. S_BRICK parameters for natural and reconstituted London clay, Pappadai clay, North-Sea clay and Corinth marl.

Parameter	London clay	Pappadai natural	Pappadai reconstituted	North-Sea natural		North-Sea reconstituted	Corinth natural																						
				Cape shore	Ferder																								
Basic BRICK parameters																													
Λ	0.1	0.254	0.204	0.1	0.1	0.1	0.6																						
K	0.02	0.029	0.046	0.02	0.02	0.02	0.005																						
I	0.0041	0.0048	0.0048	0.0041	0.0041	0.0041	0.0041																						
β_G	4	4	4	4	4	4	4																						
β_φ	3	3	3	3	3	3	3																						
N	0.2	0.2	0.2	0.2	0.2	0.2	0.2																						
M	1.3	1.3	1.3	1.3	1.3	1.3	1.3																						
S-curve (as defined in BRICK and in S_BRICK for $\alpha=0.8$)	String Length																												
	<table border="1" style="width: 100%; border-collapse: collapse;"> <tr> <td>0.000083</td><td>0.00021</td><td>0.00041</td><td>0.00083</td><td>0.0022</td><td>0.0041</td><td>0.0082</td><td>0.021</td><td>0.041</td><td>0.08</td> </tr> </table>										0.000083	0.00021	0.00041	0.00083	0.0022	0.0041	0.0082	0.021	0.041	0.08									
	0.000083	0.00021	0.00041	0.00083	0.0022	0.0041	0.0082	0.021	0.041	0.08																			
<table border="1" style="width: 100%; border-collapse: collapse;"> <tr> <td colspan="10" style="text-align: center;">G_{tan}/G_{max}</td> </tr> <tr> <td>0.92</td><td>0.75</td><td>0.53</td><td>0.29</td><td>0.13</td><td>0.075</td><td>0.044</td><td>0.017</td><td>0.0035</td><td>0.0</td> </tr> </table>										G_{tan}/G_{max}										0.92	0.75	0.53	0.29	0.13	0.075	0.044	0.017	0.0035	0.0
G_{tan}/G_{max}																													
0.92	0.75	0.53	0.29	0.13	0.075	0.044	0.017	0.0035	0.0																				
S_BRICK parameters defining structure and destructurisation																													
α/α_k		0.7/0.6	0.6/0.6	0.85/0.85	0.85/0.85	0.85/0.85	1.1/1.1																						
$\varphi(^{\circ})$	21	21	18	25.5	25.5	25.5	33																						
ω/ω_k	-	0.12/0	0/0	1.8/0	1.2/0	0.06/0	1.0/0																						
x^c_1/x^c_2	-	20/80	0/0	0/200	0/500	0/0	0/3000																						
y^c_1/y^c_2	-	0/0	0/0	0/0	0/0	0/0	0/1000																						
x^{sh}_1/x^{sh}_2	-	0/0	0/0	0/900	0/300	0/0	0/3000																						
y^{sh}_1/y^{sh}_2	-	0/0	0/0	0/1000	0/450	0/0	0/3000																						
x^{sw}_1/x^{sw}_2	-	0/0	0/0	0/200	0/500	0/0	0/0																						
y^{sw}_1/y^{sw}_2	-	0/0	0/0	0/0	0/0	0/0	0/0																						

influence on the value of the maximum angle of the shearing resistance and hence the strength response of the model. As indicated earlier, the normalized *S-shaped* curve for London clay was taken as a reference shape. The parameter α is implemented by modifying the string lengths using the following expression:

$$SL = SL_{current} \frac{(1 + \beta_\varphi \psi_B)}{(1 + \beta_G \psi_B)} \alpha \quad (5)$$

The lower and upper range for the parameter is defined so that the maximum angle of the shearing resistance φ ranges from 18° ($\alpha=0.6$) to 36° ($\alpha=1.2$), which is considered as a reasonable range of φ for natural materials, which can be easily extended at both ends. With a value $\alpha=0.7$, S_BRICK uses the same *S-shaped* curve as the basic BRICK model defined by Simpson [27]. The influence of the parameter α is graphically presented in Figure 5 for $\psi_B=0$, together with its proposed range of values.

**Figure 5.** Influence of the parameter α on *S-shaped* curve and its characteristic values.

The second parameter ω modifies the ψ_B parameter to account for the influence of structure. The definition of ω is graphically presented in Figure 4. It is best understood as an increase of the distance, in terms of volumetric strain, between the normal compression line and the critical state line of the structured material in comparison with that of the reconstituted material. In a numerical sense, the effect of parameter ω is to increase the apparent overconsolidation of the soil. It is used to modify Equation 2 with the following expression:

$$\psi_B = \varepsilon_v - \varepsilon_{v0} - \lambda \ln(p' / p'_0) + \omega \quad (6)$$

It is evident from Equations 3 and 4 that the state parameter influences both the ι parameter (elastic stiffness) and the string lengths (SLs) of the normalized *S-shaped* curve (strength) so there would be inevitably some overlapping of the influences of the parameters α and ω on the model behaviour. However, the influence of the parameter ω on ι and hence the stiffness is larger than the influence on the *S-shaped* curve and hence the strength because the *S-shaped* curve is modified by the ratio of the state parameters (Equation 3). The parameter ω is therefore the key parameter for modelling the stiffness increase and the parameter α is the key parameter for modelling the strength increase caused by the presence of structure.

3.2 Modelling of destructuring

Destructuring is modelled using the both parameters α and ω . They are given in the form of normalised exponential functions of strains to account for the presumed logarithmic nature of the destructuring [18, 23]. The rates of destructuring are made dependent on the sum of the volumetric and shear components of the plastic strains, as shown in the following two expressions:

$$\alpha_i^{c,sh,sw} = \alpha_k + (\alpha - \alpha_k) \exp \left[- \left(x_1^{c,sh,sw} (\varepsilon_v^{pl} + \delta \varepsilon_v^{pl}) + y_1^{c,sh,sw} (\varepsilon_s^{pl} + \delta \varepsilon_s^{pl}) \right) \right] \quad (7)$$

$$\omega_i^{c,sh,sw} = \omega_k + (\omega - \omega_k) \exp \left[- \left(x_2^{c,sh,sw} (\varepsilon_v^{pl} + \delta \varepsilon_v^{pl}) + y_2^{c,sh,sw} (\varepsilon_s^{pl} + \delta \varepsilon_s^{pl}) \right) \right] \quad (8)$$

in which the symbols represent the following:

α, ω	initial values of parameters for natural materials
α_k, ω_k	final values of parameters for natural materials that were destructured
α_k^*, ω_k^*	values of structure parameters for reconstituted materials

$\alpha_i^{c,sh,sw}, \omega_i^{c,sh,sw}$	current values of structure parameters in compression (c), shear (sh) or swelling (sw)
$\varepsilon_v^{pl}, \varepsilon_s^{pl}$	volumetric and shear component of plastic strain
$\delta \varepsilon_v^{pl}, \delta \varepsilon_s^{pl}$	increment of volumetric and shear component of plastic strain
$x_1^{c,sh,sw}, y_1^{c,sh,sw}$	parameters that quantify influence of volumetric and deviatoric plastic strain on destructuring of parameter α
$x_2^{c,sh,sw}, y_2^{c,sh,sw}$	parameters that quantify influence of volumetric and deviatoric plastic strain on destructuring of parameter ω

Parameters α_k^* and ω_k^* are not implicitly shown in Equations 7 and 8. They are used in the model to represent the structure in reconstituted materials and also implicitly for the materials with unstable structures, for which α_k and ω_k in the destructuring are approaching, or are equal to α_k^* and ω_k^* . Destructuring in S_BRICK is implemented separately by introducing different parameters x_1, x_2 and y_1, y_2 , for shearing, compression and swelling. The decoupling of the destructuring on the volumetric and shear components of strain at different stress paths gives an additional flexibility to the model. It is also assumed that the destructuring in the shearing is governed by both volumetric and deviator components of the plastic strain.

3.3 Parameter determination for structure and destructuring

For a complete parameter determination three drained and three undrained triaxial shearing tests and one triaxial compression test should be carried out on both the natural and the reconstituted material, which makes fourteen triaxial tests in total. As will be shown later, this number can be significantly reduced by the robustness of the model. The triaxial compression tests should be carried out to sufficiently high stresses so that destructuring of the natural material in compression can be determined. Triaxial tests should include measurements of the stiffness at very small strains and should be carried out at the different initial states shown in Figure 4, so that the material response is obtained for the overconsolidated (A, A*), normally consolidated (B, C, B*, C*) and destructured states (A^d, C^d). The asterisk sign * is used here to denote the states of the reconstituted material, while the term destructured is used to denote the state in which the parameters α_k and ω_k are approaching or are equal to α_k^* and ω_k^* .

The following procedure is developed for the determination of the parameters for the S_BRICK model:

- The geological stress history of the material should be modelled by taking into account the parameters α and ω , which describe the structure. This is necessary for all the kinematic hardening models, since the model response is governed by the initial state and the recent stress-history effects.
- From the drained triaxial tests starting from states A* and C* (see Figure 4) on the reconstituted material, a maximum angle of shearing resistance, which is here attributed to the critical state angle, is obtained and α^*_{k} is determined, yielding the values of φ , as explained by Simpson [27], which are given in the table in Figure 5.
- Parameter ω^*_{k} is always set to zero for reconstituted materials.
- From the drained triaxial tests starting from states A and B the critical state angle for the natural material is obtained and the starting value for α is determined based on the values given in the table in Figure 5.
- From the triaxial tests starting at state C^d the critical state angle is obtained for natural material destructured during compression and a final value α_k is determined based on the values given in the table in Figure 5. If the material has completely lost its structure, α_k is equal to α^*_{k} .
- Input parameters ω and ω_k are determined with a trial-and-error process so that the measured G_{max} values are reproduced by the model for all three tests starting at states A, B and C. As already indicated, if the material has no structure, ω_k is set to zero.
- From the drained triaxial shearing tests starting at states A and C, the destructuration parameters for shearing x^{sh}_1 , x^{sh}_2 , y^{sh}_1 and y^{sh}_2 are determined through a comparison of the model's prediction and measured values in q - ε_a and G - ε_s diagrams using a trial-and-error process. Because the volumetric deformations and hence destructuring due to volumetric deformation in shearing are prevented in undrained stress paths, the parameters y^{sh}_1 and y^{sh}_2 are determined from undrained tests. These values can be used to determine the volume change and are then used in drained tests to obtain the parameters x^{sh}_1 and x^{sh}_2 .
- From the results of the isotropic compression on natural material between the state points B and C^d, the destructuration parameters for the compression x^c_1 and x^c_2 can be obtained. Similarly, the parameters for swelling can be obtained for recompression (x^{sw}_1 and x^{sw}_2) between the states B and A.

Using the proposed parameter-determination procedure, a unique set of parameters is obtained for a particular material. As will be shown later, the stress-strain behaviour was modelled to a high degree of accuracy for Pappadai clay, for which the procedure was strictly

followed, and to some degree also for Corinth marl with a similar result. However, not all the materials are usually studied in such detail and many of the required tests might not be available. It is demonstrated later, on the example of North-Sea clay that a satisfactory result can also be obtained in such a case.

To summarise, the full implementation of structure and destructuring as implemented here requires the determination of the additional sixteen parameters in total. As will be demonstrated later, this number can be significantly reduced due to the robustness of the model. Four of them (α , α_k , ω and ω_k) represent the structure and twelve (x_i , y_i)^{c,sh,sw} represent the rate of destructuration in compression, swelling and shearing. A volumetric component of destructuring is present in all the drained stress paths, while shear components are present in all but the isotropic compression and swelling stress paths. It is still not clear whether or not the shear components of the plastic strains have a noticeable influence on stress paths with no significant change in the deviator component, for example, in the normal compression and the recompression stress paths. Amorosi and Kavvas [1] argue that for those stress paths only isotropic hardening and destructuring due to volumetric plastic strain have a noticeable effect. If this is the case, then the number of necessary parameters could be reduced to twelve. It is reasonable to expect that not all the types of destructuring are present for a dominant stress path, so the necessary number of total additional parameters for destructuring can be as low as four. The modelling of destructuring is implemented in such a way that the model parameters that are not significant can be omitted without hindering the model's behaviour.

4 PRESENTATION OF THE S_BRICK MODEL ON A CONCEPTUAL LEVEL

The capabilities of the S_BRICK model to simulate the structure and destructuring are presented by comparing the numerical results of the two conceptual materials taken at the different stress-strain paths for the two different states. Both materials have all the basic parameters equal, and they are the same as parameters given for London clay [27], which are summarised in Table 1, except for the amount of structure modelled. Material B represents the material with the stronger structure ($\alpha^B=1.1$ and $\omega^B=0.5$) and material A represents the material with the weaker structure ($\alpha^A=0.7$ and $\omega^A=0.0$). Using the structure parameters given for material A, the S_BRICK model is basically reduced to being the same as the basic BRICK model for London clay [27].

4.1 Results of the modelling of structure on a conceptual level using S_BRICK

The influence of the structure parameters α and ω on the increase in strength, stiffness and the SBS is presented by comparing the S_BRICK predictions for materials A and B. The purpose of showing the comparison is to demonstrate that S_BRICK is capable of modelling the main features of the theoretical framework for structural soils proposed by Cotecchia and Chandler [14].

S_BRICK predictions for stress paths that comprise normal compression, swelling, and drained triaxial shearing for materials A and B are shown in the v - $\log p'$ plane in Figure 6. The predictions of the normal compression lines (NCLs) and the critical state lines (CSLs) for both materials are also shown in the figure. The numerical triaxial tests were taken at different states (OCR varies from 1 to 10). It is evident that the CSL^B and NCL^B lie to the right of the CSL^A and NCL^A , as is expected for the material of stronger structure. It is clear that the distance between the CSL^B and NCL^B is greater than the distance between CSL^A and NCL^A , which is also expected for a material of stronger structure. Furthermore, it can be observed that S_BRICK made a prediction, which can be interpreted for each material as an almost unique position of CSL, regardless of the state in which the shearing tests were modelled. Therefore, the unity of the position of the CSL line was anticipated in the continuation on a conceptual level to interpret the other data.

The results for different drained shearing stress paths in the q - p' space for normally consolidated material

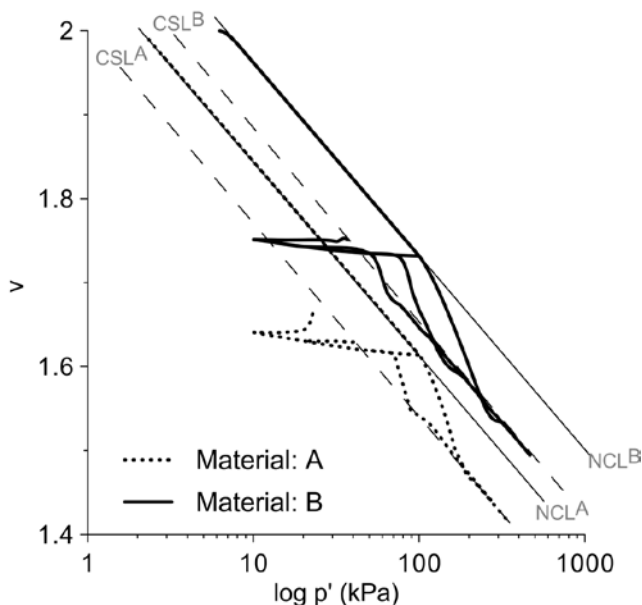


Figure 6. S_BRICK predictions of normal compression and swelling with drained triaxial shearing taken at different states for the materials A and B.

(OCR=1) and overconsolidated material (OCR=10) are shown in Figure 7. It was demonstrated that the material with a stronger structure (B) reached higher peak deviatoric stresses than the material with a weaker structure (A), regardless of the direction of the stress path and the state at which they were started. The stress paths in compression produced higher inclinations for the CSL lines than in the extension, which is expected. For the model of the over-consolidated test the increase of the peak deviatoric stress due to the over-consolidation and subsequent softening towards the CSL line is also evident. It was also observed, but not shown here, that the material with the stronger structure (B) has higher stiffness in the range from very small (i.e., below 0.001%) to large strains (i.e., above 1%) in both compression and extension.

The SBSs predicted by the model for both materials are shown by the dotted lines in Figure 8a, in which the results from the triaxial shearing at different levels of over-consolidation are presented. The results are shown as a normalized plot in the $q/p_e^A - p'/p_e^A$ plane, where p_e^A represents the equivalent pressure taken on a normal compression line of the material A. (The 50% destructurisation case shown in the figure will be considered later.) It is evident that the material B has a much larger SBS than the material A, which is expected for a material with a stronger structure. In Figure 8b the results are further normalized with the inclusion of structure (S) in the $q/Sp_e^A - p'/Sp_e^A$ plane. It can be seen that the normalised SBSs of the materials A and B coincide, as suggested by the theoretical framework for structured materials, given by Cotecchia & Chandler [14].

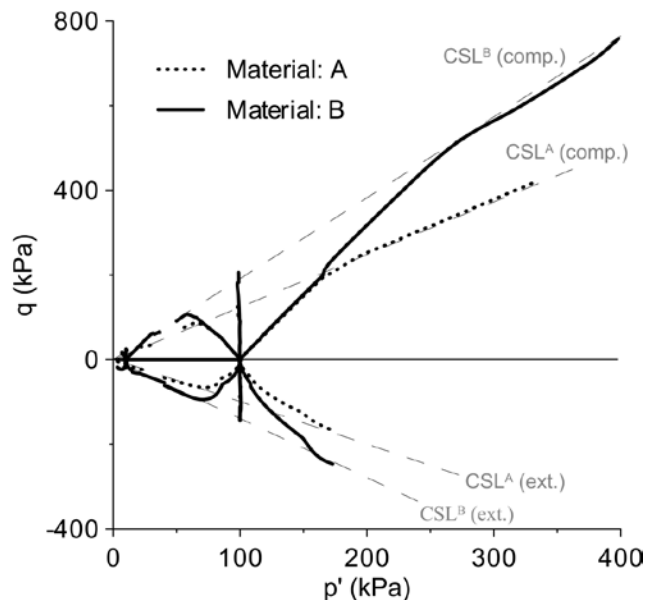


Figure 7. S_BRICK predictions of drained triaxial shearing taken at different directions for the normally consolidated and overconsolidated state (OCR=10) for the materials A and B.

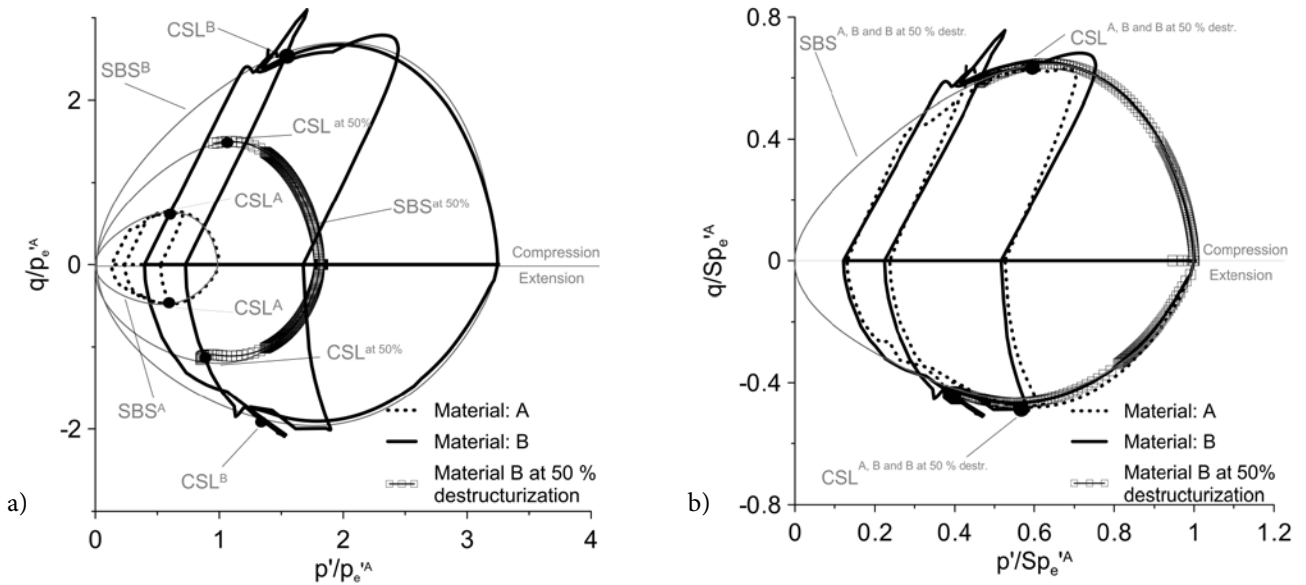


Figure 8. State boundary surfaces predicted by S_BRICK for materials A, B and material B with 50% destructurisation before shearing in: (a) $q/p_e^A - p'/p_e^A$ plot and (b) $q/Sp_e^A - p'/Sp_e^A$ plot.

4.2 Results of the modelling of destructuring on a conceptual level

The results of destructuring as modelled by S_BRICK in compression, swelling and shearing are shown by comparing the same two conceptual materials A and B. The results of destructuring in compression are shown in Figure 9a, where the parameters α and ω were reduced at different rates to 50 % of the initial values for the

material B ($\alpha_k^B=0.9$ and $\omega_k^B=0.25$). For demonstration purposes, the parameters x_i^c, y_i^c ($i=1,2$), describing the rate of destructuring in normal compression, are the same for the volumetric and the deviatoric component. The values that were used are $x_i^c, y_i^c=1000$ for the fastest rate of destructuring; $x_i^c, y_i^c=500$ for the intermediate rate and $x_i^c, y_i^c=200$ for the slowest rate of destructuring. It is evident from Figure 9a that all three tests reach the normal compression line that lies in-between the normal

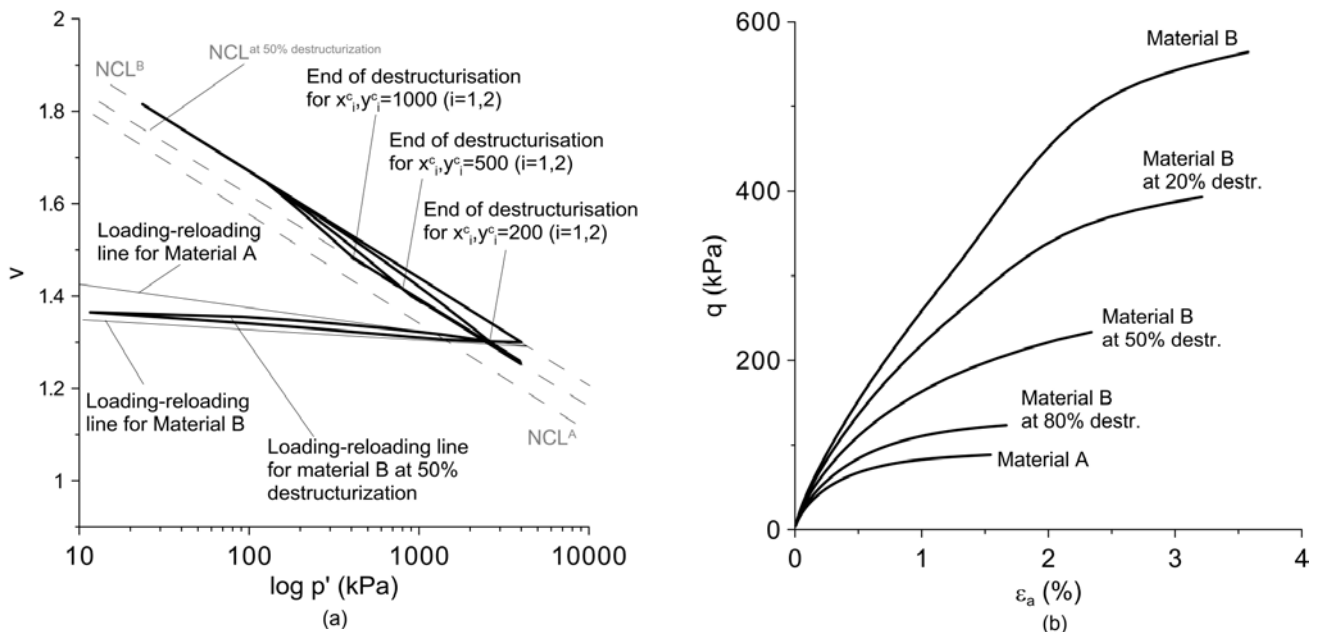


Figure 9. Different rates of destructuring at normal compression and destructuring in swelling modeled with S_BRICK (a) and different levels of destructuring for the triaxial shearing modeled with S_BRICK (b).

compression lines for materials A and B, but at different rates, as expected.

The modelling of destructuring in swelling is also presented in Figure 9a, in which the structure parameters α and ω for the material B were again allowed to reduce to 50 % of the initial values. The swelling line of the destructured material is presented together with the normal compression and swelling lines of the materials A and B. It can be seen that the slope of the swelling line of the destructured material lies in-between the swelling lines of the materials A and B. Furthermore, it can be seen that the material destructured in swelling reaches the same normal compression line after recompression as materials that were destructured in compression. The results of a triaxial shearing test after destructuring in compression are also shown in Fig 8 in the form of normalised plots. In Figure 8a, the SBS for material B at 50 % destructuring clearly lies in-between the SBSs for materials A and B, while in Figure 8b they all coincide, as one would expect according to the theoretical framework.

Finally, the modelling of destructuring in shearing is presented in Figure 9b, where the structure parameters for material B have been allowed to reduce for 20, 50 and 80%. A clear trend of reducing the peak deviator value from material B towards material A can be seen with the increasing amount of destructuring.

5. THE S_BRICK PREDICTION OF STRESS STRAIN BEHAVIOUR OF PAPPADAI CLAY, NORTH SEA CLAY AND CORINTH MARL

The S_BRICK model was validated using the laboratory results from the three different materials, which could be classified as hard soils and soft rocks according to their strength and mechanical behaviour. The Pappadai clay, North Sea clay and Corinth marl were chosen to demonstrate the ability of the S_BRICK model to cover a wide range of structured materials. The key parameters of the S_BRICK model for each natural material are given in Table 1. All the other necessary parameters for the S_BRICK model were taken as constants and were the same as the parameters for the BRICK model of London clay [27]. A list and description of the validated laboratory tests from Pappadai clay, North-Sea clay and Corinth marl are presented in Table 2.

5.1 S_BRICK prediction of the stress strain behaviour of Pappadai clay

Pappadai clay has been extensively studied over the years and its behaviour is well documented [13, 12, 14]. It is a hard over-consolidated clay with a weak cementation. According to Cotecchia and Chandler [13], the geological history of Pappadai clay followed four stages: 1) normal consolidation with the structure formation at the end

Table 2. List and description of validated laboratory tests from Pappadai clay, North-Sea clay and Corinth marl.

Pappadai clay			North Sea clay			Corinth marl		
Test label and type	p' (kPa) prior to shearing	OCR prior to testing	Test label and type	p' (kPa) prior to shearing	OCR prior to testing	Test label and type	p' (kPa) prior to shearing	OCR prior to testing
TN-14-D	500	3.4	TT-1-D	10	31	cd-98-D	98	13.3
TN-15-D	800	2.1	TT-2-D	25	16	cd-294-D	294	4.4
TN-16-D	1300	1.3	TT-3-D	50	8	cd-500-D	500	2.6
TN-17-D	2500	1	TT-4-D	760	1	cd-3000-D	3000	1
TN-18-D	1500	1.1	TT-5-D	10	70	cd-6000-D	6000	1
TN-20-D	250	6.8	TT-6-D	25	28	cd-56-U	56	23.2
TN-5-U	700	2.4	TT-7-D	50	14	cd-315-U	315	4.1
TN-6-U	300	5.7	TT-8-D	700	1	cd-550-U	550	2.4
TN-7-U	500	3.4	TT-9-D	10	86	cd-3000-U	3000	1
TN-10-U	1300	1.3	TT-10-D	25	34	cd-5000-U	5000	1
TN-11-U	1600	1.1	TT-11-D	50	17			
TN-12-U	3800	1	TT-12-D	860	1			
TN-21- K_0		1	TT-2r-D	25	13			
			TT-12r-D	800	1			

D- Drained triaxial shearing

U- Drained triaxial shearing

K_0 -Triaxial K_0 compression test

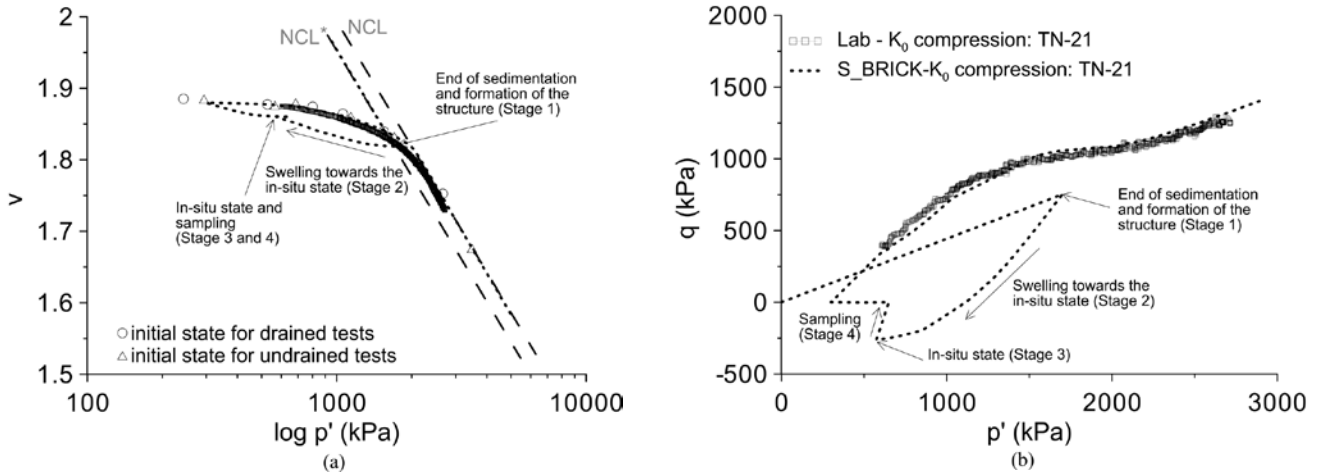


Figure 10. S_BRICK prediction of Pappadai clay history in normal compression in: (a) v - $\log p'$ (b) q - p' plots.

of sedimentation, 2) overconsolidation, 3) desiccation, oxidation and weathering and 4) unloading caused by the rise of the water table to the present level. The geological

history of Pappadai clay, modelled by S_BRICK, is shown in Figure 11, along with the Cotecchia and Chandler [13] interpretation in both v - $\log p'$ and q - p' planes.

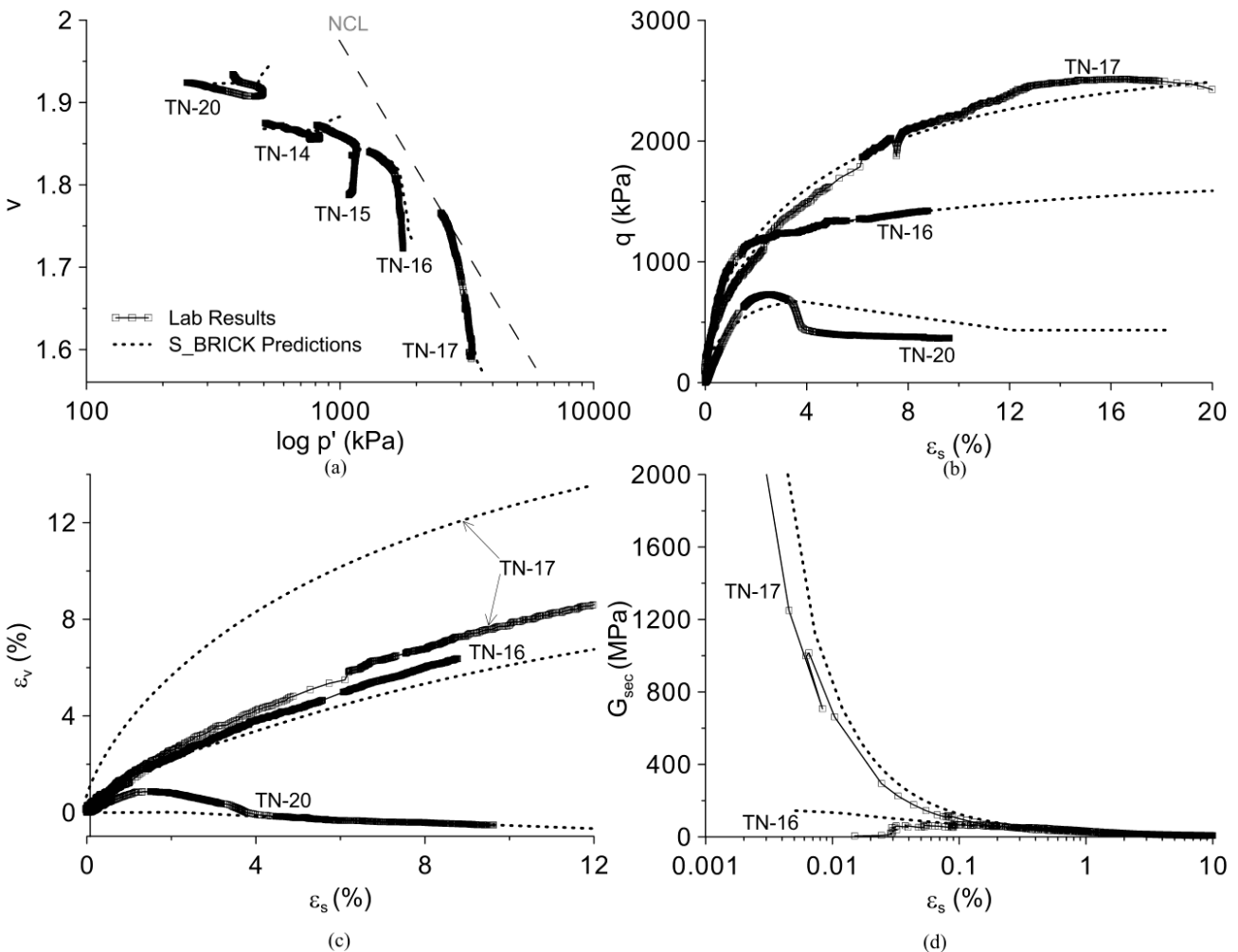


Figure 11. S_BRICK prediction of Pappadai clay behavior for drained triaxial shearing in: (a) v - $\log p'$, (b) q - ϵ_s , (c) ϵ_v - ϵ_s and (d) G_{sec} - ϵ_s plots.

The laboratory tests were carried out by Cotecchia and Chandler [13] on block samples taken from a single depth of 25 m. The material had undrained shear strength measured at around 500 kPa and was over-consolidated with $OCR=3$. Validation by the S_BRICK model was carried out using six drained and six undrained triaxial shear tests on natural clay (samples TN-6 to TN-20) with the OCR ranging from 1 to 7. The normal compression test was taken on both natural (sample TN-21) and reconstituted clay. The locations of the states of the samples prior to the drained and undrained shearing are shown in Figure 11a.

The key parameters for Pappadai clay, given in Table 1, were derived from the available laboratory data from the natural and reconstituted samples. Parameters λ and κ were derived from the compression tests on natural and reconstituted samples. The basic shape of the normalized *S-shape* curve, the parameters β_G and β_ϕ and the parameter ι were taken from the values published for London clay by Simpson [27, 29]. Based on the measured values of G_{max} in Pappadai clay the value of parameter ι was subsequently determined. The parameters for modelling the structure were derived following the previously explained procedure by using the three triaxial drained tests TN-20 (test from state A), TN-18 (test from state B) and TN-17 (test from state C). A critical state angle for the reconstituted ($\varphi_{cs}^*=18^\circ$) and the natural clay ($\varphi_{cs}=21^\circ$), given by Cotecchia and Chandler [14], was taken, leading to the values of $\alpha^*=0.6$ and $\alpha=0.7$. The values of α_k , ω and ω_k were also determined using the procedure previously explained. The numerical procedure of the modelled strength and stiffness response gave an indication that the destructuring was certainly present in compression, while in recompression and shearing no destructuring was evident, so it was not accounted for. Consequently, only six additional parameters were necessary to take into account the structure and destructuring of Pappadai clay using the S_BRICK model.

For the S_BRICK model, as for the other kinematic hardening models, it was necessary to model the geological history of the Pappadai clay in order to arrive at the current in-situ state. The sedimentation was modelled with the parameters for the reconstituted clay and at the end of sedimentation phase (formation of structure), the parameters describing the structure were added. Swelling to the in-situ state and sampling was therefore modelled using the parameters for the natural clay. This was the starting point for all the further A-class predictions of the results of laboratory tests, i.e., no changes to any S_BRICK parameters were made from this point onwards.

The S_BRICK predictions of the stress and strain behaviour of the drained triaxial shearing of Pappadai clay are shown in Figure 11. The figure shows separately (a) the compression behaviour in the $\nu\text{-log}p'$ plane, (b) the mobilisation of the deviator stress q with the shear strain ε_s , (c) the variation of the volumetric strain e_v with the shear strain ε_s and (d) the degradation of the secant shear modulus G_{sec} against the logarithmic shear strain ε_s . For clarity, only the three tests TN-20 ($OCR=6.8$), TN-16 ($OCR=1.3$) and TN-17 (NC, $OCR=1.0$) are shown in Figure 11b-d, while the results of the tests of the other samples were qualitatively similar. It can be seen that S_BRICK gave generally excellent predictions of the strength and stiffness behaviour for the entire range of deformations, regardless of the level of overconsolidation. Somewhat less successful were the predictions of the post-peak softening (Figure 11b) and the volumetric behaviour of the sample TN-17 in which the volumetric response was clearly over-predicted. As can be seen from Figure 11a, the sample TN-17 was isotropically consolidated beyond the initial SBS, so a destructuring in compression was modelled, which could be a reason for the over-prediction of the volumetric response. When a normalization of a p' - q plane is applied, dividing p' and q by p_e^* , it can be seen in Figure 12a that S_BRICK correctly predicts the position of the stress path for TN-17, which lies in between the SBS for the natural and reconstituted clay, while all the other results also correctly predict the shape of the SBS for the natural Pappadai clay. When further normalization, that includes the structure (S) is applied (Figure 12b), the SBS for the natural, reconstituted and destructured clay coincides for all the S_BRICK predictions as well as for the samples of Pappadai clay.

The undrained shearing tests were also modelled using the same set of parameters given in Table 1 for Pappadai clay. The S_BRICK predictions of the stress and strain behaviour of the undrained triaxial test are shown in Figure 13a-d in the following diagrams: (a) compression behaviour in the $\nu\text{-log}p'$ plane, (b) mobilisation of the deviator stress q with the mean effective stress p' , (c) mobilization of the deviator stress q with the shear strain ε_s and (d) degradation of the secant shear modulus G_{sec} against the logarithmic shear strain ε_s . For clarity, only the three tests TN-7 ($OCR=3.5$), TN-10 ($OCR=1.3$) and TN-12 (NC, $OCR=1.0$) are shown, while the results of the tests of the other samples were qualitatively similar. Generally, it can be concluded that the S_BRICK model gave good predictions of the undrained shear strength and stiffness decay with the deformation of the Pappadai clay samples. It was slightly less successful in modelling the post peak behaviour (Figure 13c) and it predicted somewhat different stress paths in the q - p' plane (Figure 13b) for the over-consolidated samples. When the normalization for p_e^* (Figure 14a) is applied, it can

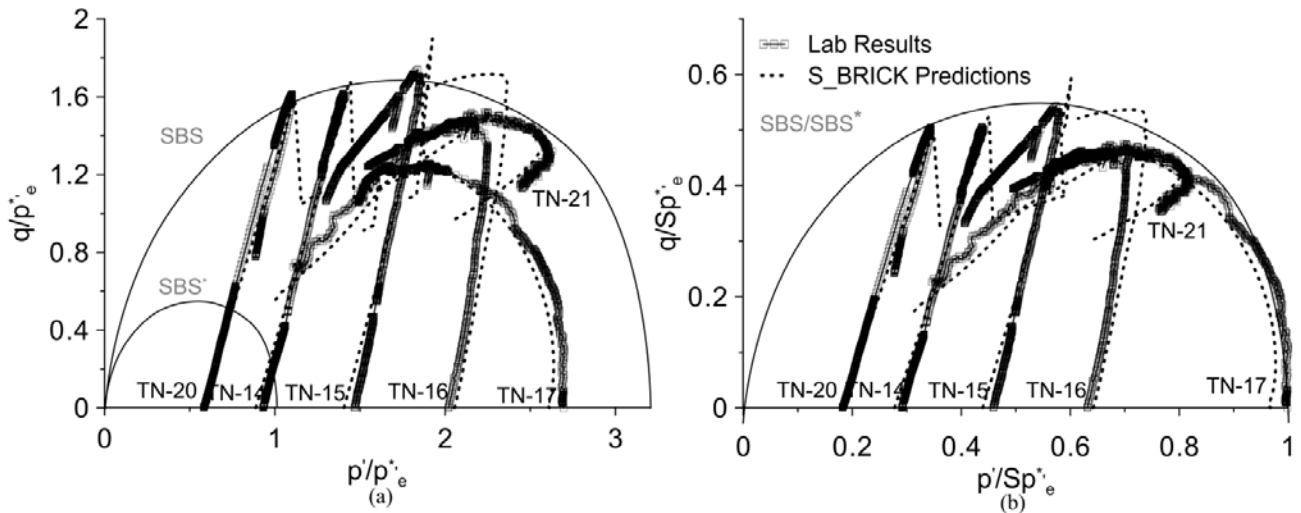


Figure 12. Laboratory and numerical results for drained triaxial tests on Pappadai clay in: (a) $q/p'_e - p'/p'_e$ and (b) $q/Sp'_e - p'/Sp'_e$ plots.

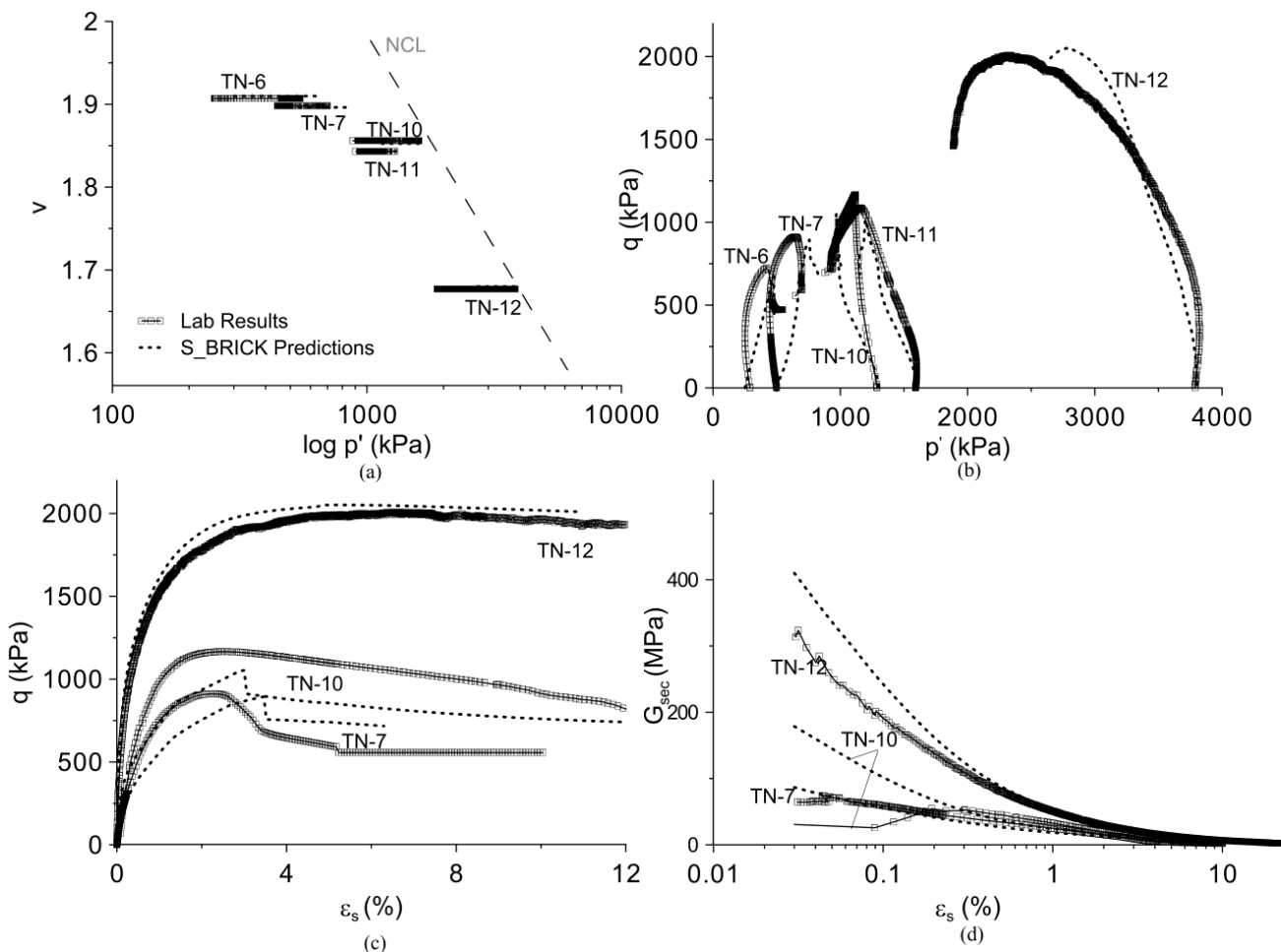


Figure 13. S_BRICK prediction of Pappadai clay behavior for undrained triaxial shearing in: (a) $v - \log p'$, (b) $q - p'$, (c) $q - \epsilon_s$ and (d) $G_{sec} - \epsilon_s$ plots.

be seen that the test TN-12 lies inside the SBS for the natural clay, which is attributed to the destructuration that occurred during compression. Similarly as for the

drained results, when further normalization with the structure parameter S (Figure 14b) is applied, all the results coincide within the boundaries of a single SBS.

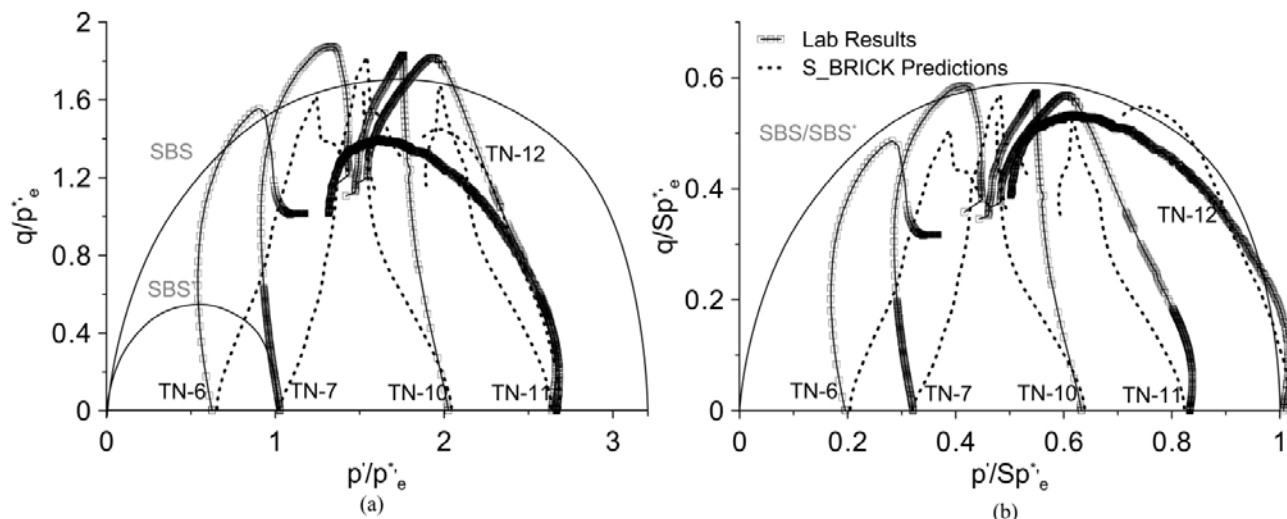


Figure 14. Laboratory and numerical results for undrained triaxial tests on Pappadai clay in: (a) $q/p^*_e - p/p^*_e$ and (b) $q/Sp^*_e - p/Sp^*_e$ plots.

5.2 S_BRICK prediction of the stress-strain behaviour of stiff North-Sea clay

The stress-strain behaviour of North-Sea clay was investigated by Jovičić et al. [20]. The investigated clay samples were taken from depths between 15 and 75 m from two different formations: the Cape Shore formation (depths between 15 and 40m) and the Ferder formation (depths between 40 and 75m). According to Johnson et al. [19] the clays from both formations are generally similar, but distinguished mainly by the values of the high undrained shear strengths found at the top of the formations (Figure 15), which is the result of breaks in the depositional sequence. A high calcium content (up to 13%) and a high undrained shear strength strongly suggested that the material is cemented.

Jovičić et al. [20] reported drained triaxial tests investigating the strength and stiffness of two reconstituted (TT-2r and TT-12r) and twelve natural samples (TT-1 to TT-12) of the clay. The tests were carried out at in-situ stresses and also when swelled back to effective stresses as low as 10 kPa. In addition to the laboratory testing, the paper reported class-A predictions (e.g., using a single set of pre-determined parameters) of the behaviour of the North-Sea clay using the basic BRICK model. As a continuation of their work, a set of class-A predictions of those tests were subsequently modelled using the S_BRICK model and compared with the laboratory data and the prediction of the basic BRICK model.

The input parameters for modelling North Sea clay, taken from Jovičić et al. [20], are shown in Table 1. The procedure for the determination of the parameters describing the structure could not be followed in full in this case as the tests were not originally designed for

that purpose. The adopted approach was to model the amount of overconsolidation for each individual sample in accordance with the estimated level of additional overburden (Figure 15) at the depth of the sampling. The

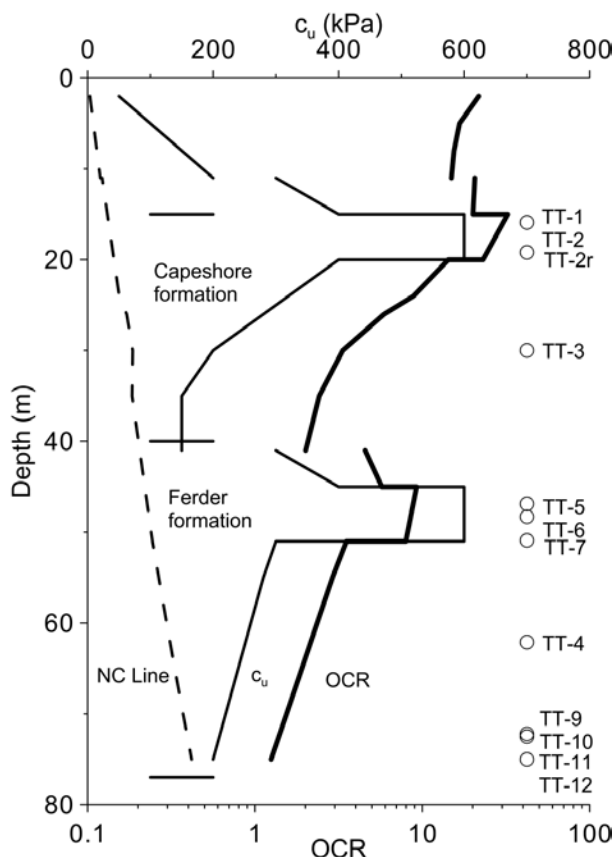


Figure 15. North-Sea clay undrained shear strength profile with sample location and estimated OCR profile (after Jovičić et al. [20]).

difference in the approach taken by Jovičić et al. [20] was that the influence of the structure was accounted for, so that realistic levels of the estimated over-consolidation, based on the measured values of undrained shear strength, could have been used.

The parameters α^* and ω^* were determined from the critical state angle of the shearing resistance for the reconstituted clay, which were obtained from the two triaxial shearing tests on reconstituted samples. Based on the available results, the parameter α was taken to be the same as for the reconstituted material and the parameter ω was determined by taking into account the small strain stiffness response of the clay. The parameter ω_k was determined by matching the strength and stiffness at the critical state after the destructurisation was finished. Since no study of the influence of compression and swelling on the destructurisation was carried out for the North Sea clay, it was first estimated that only a destructurisation in shearing is present. However, even with the structure and the destructurisation in shearing taken into account, it was still not possible to satisfactorily reproduce the stress-strain response of the soil. It was concluded that the North-Sea clay has probably a structure that is sensitive to both swelling and compression, to which the samples were exposed during sampling and subsequent shearing stress paths. This was particularly relevant for the samples that were swelled to low confining pressures. The parameters for describing the destructurisation both in swelling and compression were determined through a trial-and-error process. For the samples taken from the Cape Shore and Ferder formations different parameters describing the structure and destructurisation were obtained, as can be seen from Table 1, with the Cape Shore formation featuring a stronger structure.

Most of the shear tests in the original laboratory programme were taken after the swelling to a low effective stress. From the Cape Shore formation, four samples were modelled: TT-1 (sheared from $p'=8$ kPa, OCR=31), TT-2 (sheared from $p'=25$ kPa, OCR=16), TT-3 (sheared from $p'=50$ kPa, OCR=8) and reconstituted clay TT-2r (sheared from $p'=25$ kPa, OCR=12). From the Ferder formation nine samples were modelled, but for clarity only the results from the four samples are shown: TT-12 (sheared from $p'=800$ kPa, NC), TT-8 (sheared from $p'=650$ kPa, NC), TT-11 (sheared from $p'=200$ kPa, OCR=3.2), and TT-6 (sheared from $p'=25$ kPa, OCR=28). The S_BRICK prediction of the triaxial shearing tests of the samples from the Cape Shore and Ferder formations are shown in Figure 16 and Figure 17, respectively. Each figure shows separately (a) the variation of the deviator stress q and the axial strain ε_a , (b) the variation of the volumetric strain ε_v , with the

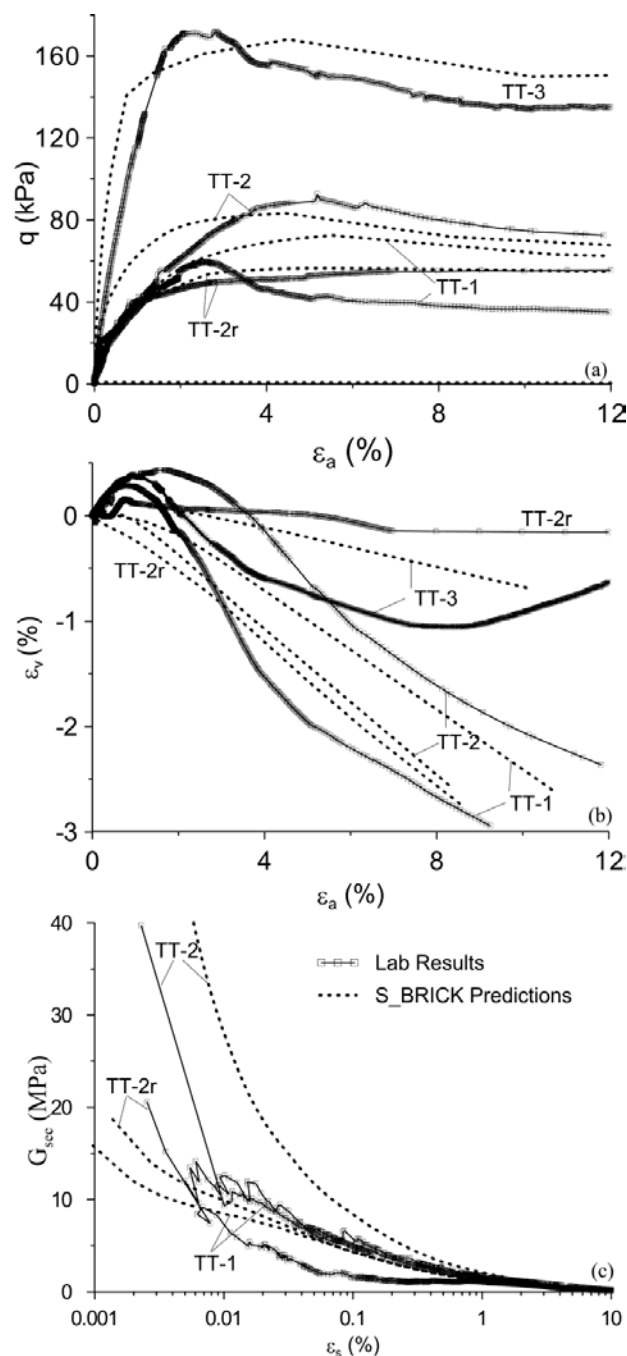


Figure 16. S_BRICK prediction of North-Sea clay behavior for drained triaxial shearing (Cape Shore formation – depth 15-30m) in: (a) q - ε_a , (b) ε_v - ε_a and (c) G_{sec} - ε_s plots.

axial strain ε_a and (c) the degradation of the secant shear modulus G_{sec} against the logarithmic shear strain ε_s .

It can be seen from the figures that the S_BRICK model has reasonably well reproduced behaviour for the samples of both clays, and also for the reconstituted material. The peak deviator stresses shown in Figure 16a and Figure 17a were correctly predicted; however,

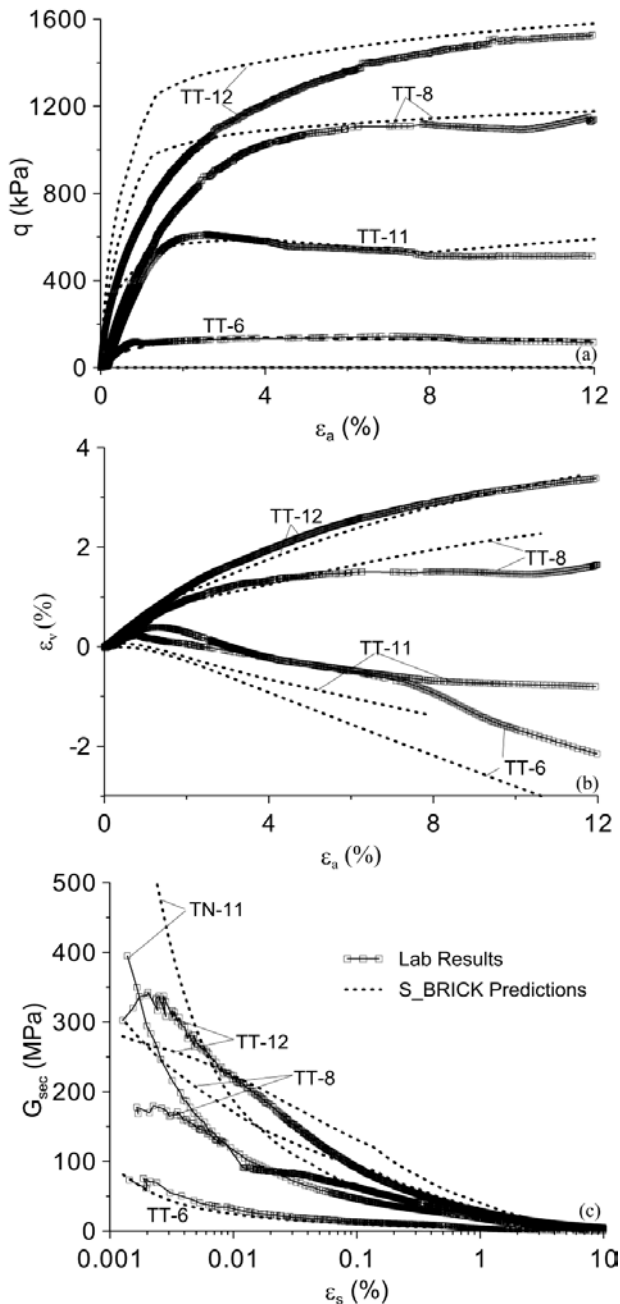


Figure 17. S_BRICK prediction of North-Sea clay behavior for drained triaxial shearing (Ferder formation– depth 45-75m) in: (a) q - ϵ_a , (b) ϵ_v - ϵ_a and (c) G_{sec} - ϵ_s plots.

the model gave a somewhat stiffer response, which can be clearly seen in Figures 16c and 17c, in which the shear stiffness degradation is shown. The volumetric behaviour shown in Figure 16b and Figure 17b, has been generally well predicted, with the model correctly predicting dilation or contraction. When comparing the results published by Jovičić et al. [20] on the same set of laboratory data using the basic BRICK model without

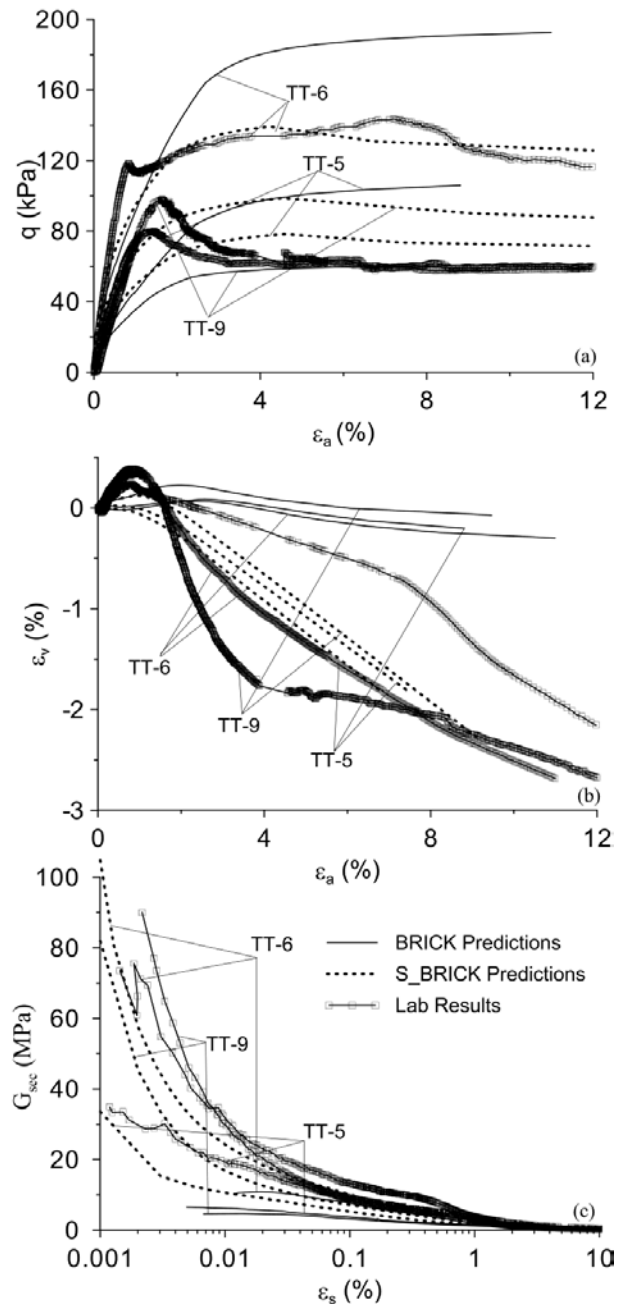


Figure 18. Comparison between S_BRICK and BRICK predictions of North-Sea clay behavior for drained triaxial shearing in: (a) q - ϵ_a , (b) ϵ_v - ϵ_a and (c) G_{sec} - ϵ_s plots (BRICK predictions after Jovičić et al. [20]).

structure, a significant improvement can be observed using S_BRICK, as it can be seen in Figure 18. The S_BRICK prediction of the peak deviator strength falls within the range $\pm 15\%$, when comparing to the laboratory results, while the BRICK prediction falls well below that (Figure 18a). Also, a significantly better prediction was obtained when comparing the shear moduli at different strain magnitudes, ranging from 0.001% to 1%

(Figure 18c). The motivation for the development of the S_BRICK model was to improve the predictions of the BRICK model for the behaviour of North Sea clay. These results clearly demonstrate the necessity for the structure to be accounted for in the constitutive modelling of this natural material [31, 32].

5.3 S_BRICK prediction of the stress-strain behaviour of Corinth marl

The S_BRICK prediction of the stress-strain behaviour of Corinth marl was based on the published data from the literature [3,9,10]. According to the different authors, Corinth marl is heavily cemented, predominantly carbonate material (up to 75 % of the carbonate content), for which the cementation occurred at the end of the sedimentation. The investigated Corinth marl was taken from a depth of 60m, at the base of the Corinth canal. The samples had a measured high, undrained shear strength ($c_u=2000$ kPa), and were overconsolidated (OCR=2.5) in the in-situ state. The S_BRICK model was validated using the laboratory results from the five drained and the five undrained triaxial shear tests, with the OCR varying between 1 and 24 and on one normal compression test.

The parameters λ and κ given in Table 1 were taken from Burland et al. [10]. The previously explained procedure was followed to determine the parameters ω and ω_k . The procedure was based on the three triaxial drained tests cd98 (test from state A), cd3000 (test from state B) and cd6000 (test from the state C). The critical state angle of the shearing resistance of 33.4° given by Anagnostopoulos et al. [3] was used, yielding a value for $\alpha=1.1$. The analysis of the available data showed that the destructuring was present both in compression and in shearing. The influence of the deviatoric component was

determined from the undrained tests, and the influence of the volumetric component from the drained tests.

As with the Pappadai clay, the stress history was modelled comprising sedimentation, formation of the structure, overconsolidation to the in-situ state and subsequent sampling and consolidation. The results of the S_BRICK prediction are shown in Figure 19: a) in the $v\text{-log}p'$ plane and b) in the $q\text{-}p'$ plane. It can be seen that the S_BRICK model correctly predicted both the normal compression line for the reconstituted (NCL*) and natural (NCL) Corinth marl. It also correctly predicted the compression and the recompression behaviour as well as the yielding pressure in compression, given by Bressani [9].

The Class-A predictions of the S_BRICK model are shown in Figure 20, along with the results of the drained tests on the three samples: cd98 (sheared from $p'=98$ kPa, OCR=13.3), cd294 (sheared from $p'=294$ kPa, OCR=4.4) and cd500 (sheared from $p'=500$ kPa, OCR=2.6). The figure shows: (a) the variation of the deviator stress q with the axial strain ε_a , (b) the variation of the volumetric strain ε_v with axial strain ε_a and (c) the degradation of secant shear modulus G_{sec} against the logarithmic axial strain ε_a . It can be observed that the S_BRICK model has correctly predicted the peak deviator stress (Figure 20a) and the mobilisation of the stiffness with the shear strain (Figure 20c). The stiffness degradation prediction was good, but the comparison is hampered by the limitation of the available laboratory data with the stiffness measured only up to 0.1%. The prediction of the volumetric behaviour shown in Figure 20b was generally good, with the model correctly predicting the dilative or contracting behaviour. The results from the prediction of the undrained shearing are shown in Figure 21 in the form of a $q\text{-}p'$ plot. The five tests

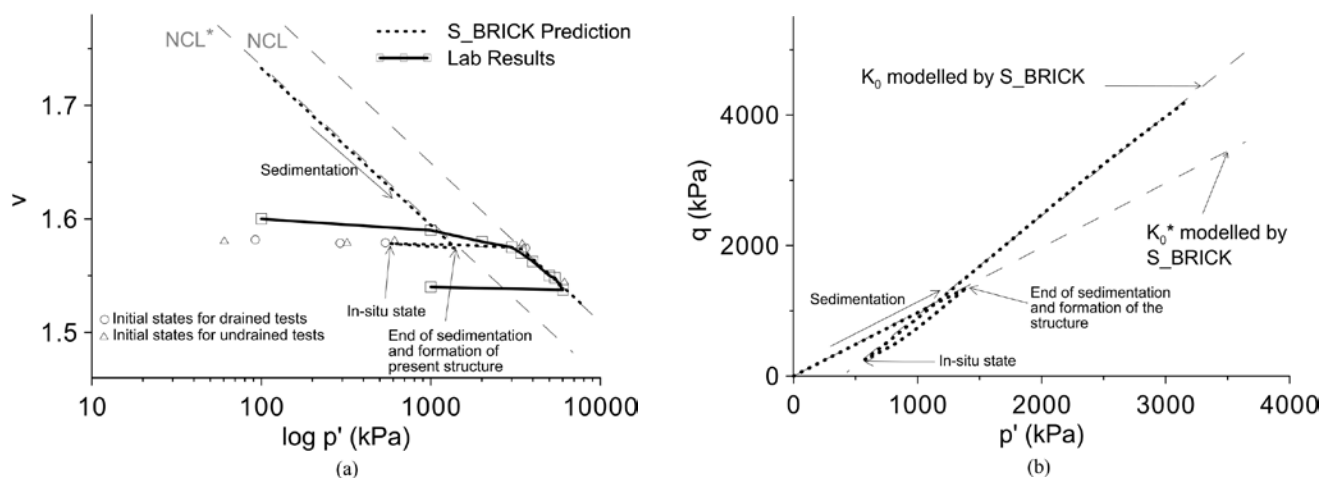


Figure 19. S_BRICK prediction of Corinth marl history in normal compression (a) $v\text{-log}p'$ (b) $q\text{-}p'$ plots.

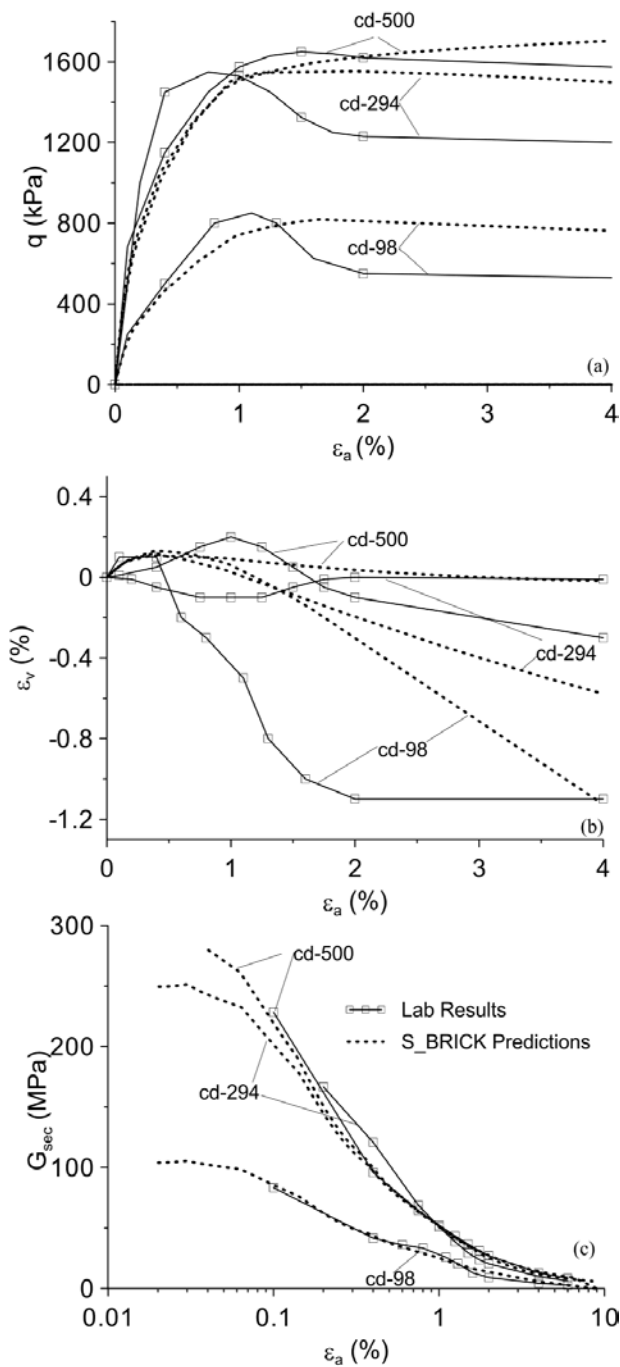


Figure 20. S_BRICK prediction of Corinth marl behavior for drained triaxial shearing in: (a) q - ε_a , (b) ε_v - ε_a and (c) G_{sec} - ε_s plots.

were carried out on samples taken from the heavily over-consolidated states (sheared from $p' = 56$ kPa, $OCR = 23$) up to the samples consolidated well beyond the yielding pressure (sheared from $p' = 5000$ kPa) in compression. It can be seen that S_BRICK correctly predicted the undrained shear strength and also the undrained shear-stress paths for both the overconsolidated and normally consolidated samples for the full range of stresses.

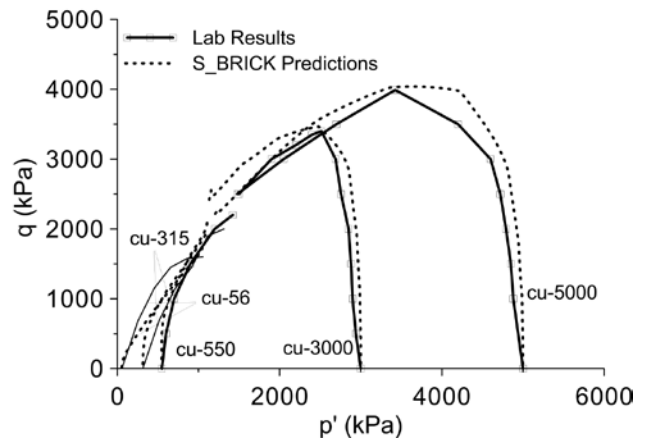


Figure 21. S_BRICK prediction of Corinth marl behavior for undrained triaxial shearing in q - p' plot.

5.4 Discussion

The analysis of the prediction using the S_BRICK model demonstrated that the model was able to predict correctly the main features of the stress-strain behaviour of the three completely different, natural, structured materials. For Pappadai clay and Corinth marl the excellent predictions of the compression behaviour in the v - $\log p'$ plane were obtained, with the S_BRICK model essentially correctly predicting the normal compression lines for both the reconstituted and natural material. The condition for this was the correct estimates of the geological histories of the two materials, which were in this case available from the work of the other authors. For all the materials the best results were obtained when predicting the peak strengths in the drained triaxial tests, with an average deviation of less than 5% and a maximum deviation of no more than 15%, which was derived only for the very heavily over-consolidated samples of North-Sea clay (TT-1 and TT-10). The undrained shear strengths were also successfully predicted, with an average deviation of under 10%. The analysis of the shear modulus degradation with the strain at a very small strain level (i.e., below 0.001%) was possible only for the North-Sea clay, due to the lack of the laboratory results for the other materials in the range of the small strains. More than half of the predicted shear moduli for all the twelve samples taken at the different strain magnitudes, ranging from very small strains of 0.001% to large strains at 1%, fall within the range of $\pm 25\%$ difference from the measured values in the laboratory. For both the Pappadai clay and the Corinth marl the prediction was satisfactory for the small (i.e., between 0.01% and 0.1%) but better for the middle strain range (i.e., between 0.1% and 1%) and also at large strains at 1% and above. It is therefore conclusive that the modelling of the shear modulus degradation with the strain at

the middle-to-large strain level was generally accurate for all the three materials.

The least successful aspect of the S_BRICK predictions was the volumetric strains. In general, the drained peak strength values were predicted at strains that were somewhat larger than those measured in the laboratory. The model correctly predicts the dilative or contractive response, but the amount of contraction or dilation is not always accurately predicted. In undrained shearing this is also reflected in the prediction of the undrained stress paths. However, the volumetric component of the deformation is a complex phenomenon and the modelling of the volumetric deformation requires more research and a better understanding of the volumetric behaviour in compression, swelling, reloading and shearing.

6 CONCLUSIONS

A model for structured soils named S_BRICK was developed from the basic BRICK model originally published by Simpson [27, 29]. The capabilities of S_BRICK to model the structure and the destructuring were first demonstrated on a conceptual level within the boundaries of the theoretical framework for structured soils developed by Cotecchia and Chandler [14]. It was shown that the S_BRICK model, extrapolating the concept of the state parameter originally set in the BRICK model, can describe all the main features of the framework for the behaviour of the structured soils. The model also includes the behaviour of the reconstituted materials, as it contains unchanged elements from the original BRICK model.

The S_BRICK model was validated on three natural materials, i.e., Pappadai clay, North-Sea clay and Corinth marl, featuring different origins, geological history, mineralogy, type of structure and over-consolidation. It was shown that S_BRICK was able to successfully capture the stress-strain behaviour typical for those natural structured materials. It can be concluded that S_BRICK, which in itself contains the complete BRICK model, has a universal potential to model a wide range of natural clay soils, including normally consolidated and over-consolidated clays, as well as hard soils and soft rocks.

In its widest form the new model requires a total of 16 additional parameters to describe the structure and destructuring. However, it was demonstrated that for the successful validation of the behaviour of natural materials, only six to seven additional parameters were necessary. In the case of Pappadai clay, which was the most researched material in terms of the origin of struc-

ture and destructuring, the predictions were the most accurate and in the best agreement with the theoretical framework for the structured materials. The validation of the North-Sea clay behaviour has also shown that the model is sufficiently robust, even though the geological history is not fully understood, to predict satisfactorily the behaviour of two different formations and without all the necessary tests for the parameter determination. The validation of the behaviour of Corinth marl was more successful, as the origin of the structure and over-consolidation were better understood than that of the North Sea clay.

Additional work on the model still has to be done with regards to the prediction of the volumetric behaviour and the destructuring. The mechanisms of destructuring and the development of the volumetric strains are both clearly affected by the type of plastic strains and are likely to be different in compression, swelling, reloading and shearing. This subject clearly requires more fundamental research on the theoretical and practical levels in the laboratory. The results of the research demonstrate that different causes of the development of volumetric strains were the aspects of the validation that proved to be the most difficult to achieve using the S_BRICK model.

Acknowledgments

Development of the S_BRICK model was sponsored by the Slovenian Research Agency (ARRS) as a part of a sponsored PhD study and the research project "Development and implementation of a constitutive model for Soft Rocks and Hard Soils, contract No. L2-7036. The authors are deeply indebted to Brian Simpson for his insights and encouragements during the course of the research. The authors are grateful to Federica Cotecchia and Politecnico di Bari for making the results of laboratory test of Pappadai clay available for the numerical validation and research. The authors are also thankful to Kirk Ellison for his in-depth comments and insights in the draft version of the paper.

REFERENCES

- [1] Amorosi, A., Kavvas, M.A. 2002. Critical review of the State Boundary Surface concept in light of advanced constitutive modelling. In Numerical Models in Geomechanics: Proceedings of the 8th International Symposium, NUMOG VIII, Rome, 10–12 April 2002. Edited by G.N. Pande and S.

- Pietruszczak, A.A. Balkema, Rotterdam, The Netherlands. pp. 85–90.
- [2] Amorosi, A., Rampello, S. 2007. An experimental investigation into the mechanical behaviour of a structured stiff clay. *Géotechnique* 57, 2, 153-166. <https://doi.org/10.1680/geot.2007.57.2.153>
- [3] Anagnostopoulos, A.G., Kalteziotis, N., Tsiamboas, G.K., Kavvadas, M. 1991. Geotechnical properties of the Corinth canal marls. *Geotechnical and Geological Engineering* 9, 1, 1-26. <https://doi.org/10.1007/BF00880981>
- [4] Atkinson, J.H., Bransby, P.L. 1978. *The Mechanics of Soils: An introduction to Critical State Soil Mechanics*. McGraw-Hill.
- [5] Atkinson, J.H., Richardson, D., Stallebrass, S.E. 1990. Effect of recent stress history on the stiffness of overconsolidated soil. *Géotechnique* 40, 4, 531-540. <https://doi.org/10.1680/geot.1990.40.4.531>
- [6] Baudet, B.A. 2001. *Modelling effects of structure in soft natural clays*. PhD thesis. City University, London.
- [7] Baudet, B.A., Stallebrass, S.E. 2004. A constitutive model for structured clays. *Géotechnique* 54, 4, 269-278. <https://doi.org/10.1680/geot.2004.54.4.269>
- [8] Been, K., Jeffries, M.G. 1985. A state parameter for sands. *Géotechnique* 35, 1, 99-112. <https://doi.org/10.1680/geot.1985.35.2.99>
- [9] Bressani, L.A. 1993. *The secant stiffness behaviour of Corinth Marl*. *Geotechnical Engineering of Hard Soils and Soft Rocks*, Athens Greece, Ed. Anagnostopoulos, A. G. et al., Rotterdam, Balkema, 391-396.
- [10] Burland, J.B., Rampello, S., Georgiannou, V.N., Calabresi, G. 1996. A laboratory study of the strength of four stiff clays. *Géotechnique* 46, 3, 491-514. <https://doi.org/10.1680/geot.1996.46.3.491>
- [11] Clayton, C.R.I., Priest, J.A., Rees, E.V.L. 2010. The effect of hydrate cement on the stiffness of some sands. *Géotechnique* 60, 6, 435-445. <https://doi.org/10.1680/geot.2010.60.6.435>
- [12] Cotecchia, F. 1996. *The effects of structure on the properties of an Italian Pleistocene clay*. PhD Thesis, Imperial College, London.
- [13] Cotecchia, F., Chandler, R.J. 1995. Geotechnical properties of the Pleistocene clays of the Pappadai Valley, Taranto, Italy. *Quarterly Journal of Engineering Geology* 28, 5-22. <https://doi.org/10.1144/GSL.QJEGH.1995.028.P1.02>
- [14] Cotecchia, F., Chandler, R.J. 2000. A general framework for the mechanical behaviour of a clays. *Géotechnique* 50, 4, 431-447. <https://doi.org/10.1680/geot.2000.50.4.431>
- [15] Ellison, K.C., Kenichi, S., Simpson B. 2012. A strain space soil model with evolving stiffness anisotropy. *Géotechnique* 62, 7, 627-641. <https://doi.org/10.1680/geot.10.P095>
- [16] Ferreira, P.M.V., Bica, A.V.D. 2006. Problems in identifying the effects of structure and critical state in a soil with transitional behaviour. *Géotechnique* 56, 7, 445-454. <https://doi.org/10.1680/geot.2006.56.7.445>
- [17] Gasparre, A., Nishimura, S., Minh, N.A, Coop, M.R., Jardine, R.J. 2007. The influence of structure on the behaviour of London clay. *Géotechnique* 57, 1, 19-31. <https://doi.org/10.1680/geot.2007.57.1.19>
- [18] Gens, A., Nova, R. 1993. Conceptual bases for a constitutive model for bonded soils and weak rocks. *Geotechnical Engineering of Hard Soils-Soft Rocks*, Athens, Greece, eds. Anagnostopoulos, A.G. et al., Rotterdam: Balkema, 485-494.
- [19] Johnson, H., Richards, P.C., Long, D., Graham, C.G. 1993. *The geology of the Northern North Sea*. British Geological survey, United Kingdom Offshore Regional Report. HMSO, London.
- [20] Jovičić, V., Coop M., Simpson, B. 2006. Interpretation and modelling of deformation characteristics of a stiff North Sea clay. *Can. geotech. j.* 43, 4, 341-354. <https://doi.org/10.1139/t06-007>
- [21] Kavvadas, M. 2000. General report: Modelling the soil behaviour – Selection of soil parametres. *The Geotechnics of Hard Soils-Soft Rocks*. (Ed. Evangelista & Picarelli), Balkema, 1441-1481.
- [22] Kavvadas, M., Anagnostopoulos, A.G. 1998. A framework for mechanical behaviour of structured soils. *The Geotechnics of Hard Soils – Soft Rocks*, Ed. Evangelista, A., et al., Rotterdam: Balkema, 591-601.
- [23] Kavvadas, M., Amorosi, A. 2000. A constitutive model for structured soils. *Géotechnique* 50, 3, 263-273. <https://doi.org/10.1680/geot.2000.50.3.263>
- [24] Lambe, T.W., Whitman, R.V. 1969. *Soil Mechanics*. New York: John Wiley & Sons Inc.
- [25] Leroueil, S., Vaughan, P.R. 1990. The general and congruent effects of structure in natural soils and weak rocks. *Géotechnique* 40, 3, 467–488. <https://doi.org/10.1680/geot.1990.40.3.467>
- [26] Rouainia, M., Wood, M.D. 2000. A kinematic hardening model for natural clays with loss of structure. *Géotechnique* 50, 2, 153-164. <https://doi.org/10.1680/geot.2000.50.2.153>
- [27] Simpson, B. 1992. Retaining Structures: displacement and design. 32nd Rankine Lecture: *Géotechnique* 42, 4, 541-576. <https://doi.org/10.1680/geot.1992.42.4.541>

- [28] Simpson, B. 2001. Engineering needs. Proc. 2nd Int. Symp. on Pre-failure Deformation Characteristics of Geomaterials, Torino, volume 2, 1011-1026 (Eds M. Jamiolkowski, R. Lancellotta, D.Lo Presti), Lisse, Swets & Zeitlinger. .
- [29] Simpson, B. 2001. BRICK 17, GEO suite for windows. Published on: http://www.oasys-software.com/product/downloads/geo/brick_Nov01.pdf
- [30] Schofield, A.N., Wroth, C.P. 1968. Critical State Soil Mechanics. Maidenhead: McGraww-Hill.
- [31] Vukadin, V. 2004. Development of the constitutive model for Soft Rocks and Hard Soils, PhD thesis, University of Ljubljana, Ljubljana.
- [32] Vukadin, V. 2007. Modelling of the stress-strain behaviour in Hard Soils and Soft Rocks, Acta Geotechnica Slovenica 4, 2, 4-15.

LOADING AND UNLOADING TEST OF HARD ROCK AND ITS ELASTOPLASTIC DAMAGE COUPLING MODEL

OBREMENILNI IN RAZBREMENILNI PREIZKUS TRDNIH KAMNIN IN NJIHOV ELASTOPLASTIČNI MODEL POŠKODBE KONTAKTA

Zhen Li (*corresponding author*)

Henan Polytechnic University,
School of Civil Engineering,
Jiaozuo, Henan 454000, China
E-mail: zhenli@hpu.edu.cn

Dongdong Zhang

Yankuang Group Company Limited,
Yanzhou Coal Ordos Neng Hua Company Limited,
Ordos, Inner Mongolia Autonomous Region
017000, China

Shuang Zhao

Yankuang Group Company Limited,
Yanzhou Coal Ordos Neng Hua Company Limited,
Ordos, Inner Mongolia Autonomous Region
017000, China

DOI <https://doi.org/10.18690/actageotechslov.15.2.38-46.2018>

Keywords

high stress; hard rock; loading and unloading test; coupling model

Ključne besede

visoka napetost; trdna kamnina; obremenilni in razbremenilni preizkus; model kontakta

Abstract

Deep-buried engineering and test results show that hard rocks behave as part of an elastoplastic damage coupling process. The coupling effect can contribute to the weakness of the surrounding rocks and the extension of the water channels. As a result, the coupled elastoplastic damage model is the basis for a stability analysis in deep engineering. In this paper loading and unloading tests were conducted on T_{2b} marble in the Jinping II hydropower station. Based on the tests the effects of the confining pressure on the strength, the failure strain and the dilation were analyzed. According to the plastic shear failure and the parameters weakness mechanism, the damage-evolution function reflecting the weakness character, the loading function and the plastic potential function regarding plastic hardening were proposed. The activation of the damage and plastic process was then studied. The coupled elastoplastic damage model was finally established. Through simulating the test curve, the proposed model was verified. This model could play an important role in the stability analysis of deep-buried hard-rock engineering.

Izvleček

Globoko vkopani inženirski objekti in rezultati preizkusov kažejo, da se trdne kamnine obnašajo kot del elastoplastičnega procesa poškodbe kontakta. Vpliv na intaktnost kontakta lahko prispeva k šibkosti okoliških kamnin in razširitvi vodnih kanalov. Rezultat tega je, da je elastoplastični model poškodbe kontakta osnova za analizo stabilnosti pri globoko vkopanih inženirskih objektih. V prispevku smo na marmorju T_{2b} na hidroelektrarni Jinping II izvedli obremenilne in razbremenilne preizkuse. Na podlagi preizkusov smo analizirali učinke hidrostatskega tlaka na trdnost, specifično deformacijo pri porušitvi in dilatacijo. Glede na plastično strižno porušitev in mehanizem slabosti parametrov smo predlagali funkcijo razvijanja poškodb, ki odraža značilnost šibkosti, obremenilno funkcijo in funkcijo plastičnega potenciala pri plastičnem utrjevanju. Nato smo proučevali aktivacijo poškodb in plastičnih procesov. Končno je bil ugotovljen povezani model elastoplastične poškodbe. Predlagan model je bil preverjen s simulacijo preizkusne krivulje. Ta model bi lahko imel pomembno vlogo pri analizi stabilnosti globoko vkopanih inženirskih objektov v trdnih kamninah.

1 INTRODUCTION

To deal with the potential problems associated with a shortage of energy supply, many hydropower stations and transportation tunnels are being built in China, implementing the western development strategy project. The huge rock engineering located in high mountains in the west of China, have characters such as deep buried, high stress and long span. For example, the diversion tunnel in the Jinping II hydropower station has a maximum length of 16.6km, an excavation diameter of 13m, a general buried depth of 1500~2000m and a maximum buried depth exceeding 2500m. In this case its high initial geostress and water pressure add difficulties to the construction. Besides these, the diversion tunnel goes through the Jinping mountain and various rock layers. The rock mass has many fractures and water flowing structures. The maximum water pressure exceeds 10MPa[1]. During the excavation of the auxiliary tunnels, the rockburst and water gushing problems resulted in a lot of loss and damage (see Fig.1) [2]. Therefore, the disaster prevention and control in the high geostress and water pressure are the key problems in the construction of deep buried tunnels.



Figure 1. Rock-burst and water-gushing problems in deep buried hard rock in the Jinping II hydropower station: (a) strong rock burst (b) high-pressure and large-volume groundwater infiltration.[2].

In the case of high geostress, the behavior of hard rock has its special characters: a) it has the ductility characters in high confining pressure in contrast to the brittleness in the low confining pressure[3]; b) the Mohr-Coulomb criterion applying to the shallow buried rock cannot be used in the deep buried rock with non-linear characters[4]; and c) the elastoplastic deformation becomes more complex. Under the applied force, the microfissures extend and penetrate. On one hand, the strength of the surrounding rock weakens with additional strain generation. On the other hand, the connected fissures act as the water-gutting channels. Therefore, the plastic deformation and damage to the rock have a coupling effect. The coupled elastoplastic damage analysis is the basis for solving the stability problem of deep buried tunnels.

In the triaxial test the microfissures propagate with the increasing load. Material damage accumulates due to the plastic process. Meanwhile, the damage leads to further irreversible plastic deformation, a non-linear constitutive relationship, a strain-softening material and dilation. These mechanical phenomena can be viewed as the coupling effect of damage and plasticity, which is described by continuum damage mechanics and plasticity theory, respectively[5]. Salari et al.[6] formulated a constitutive model in the framework of continuum thermodynamics using internal variables. Chiarelli et al.[7] proposed that the plastic deformation and anisotropy damage are coupled using a triaxial test with claystones. Zhu et al.[8] formulated a micromechanics-based constitutive model for granular materials like sands under a relatively low confining pressure. Zhou and Zhu[9] developed an elasto-plastic damage constitutive model with double yield surfaces for the soft rock.

The existing research was mostly focused on the elastoplastic damage coupling problems in soft rock, while research on the hard rock with deep buried high stresses is still not sufficient. In this paper we made an analysis of the mechanical behavior of the hard rock based on the test results. The coupled elastoplastic damage model was proposed and validated. The work acts as the basis for a study on the weakening process of the surrounding rocks and the formulation of water-gushing fissures.

2 TEST ANALYSIS

2.1 Test methods and results

The standard cylinder marble samples with sizes of 50×100 mm were made from the marble core buried 2500 m underground in the Jinping II hydropower station diversion tunnel in the Sichuan province of

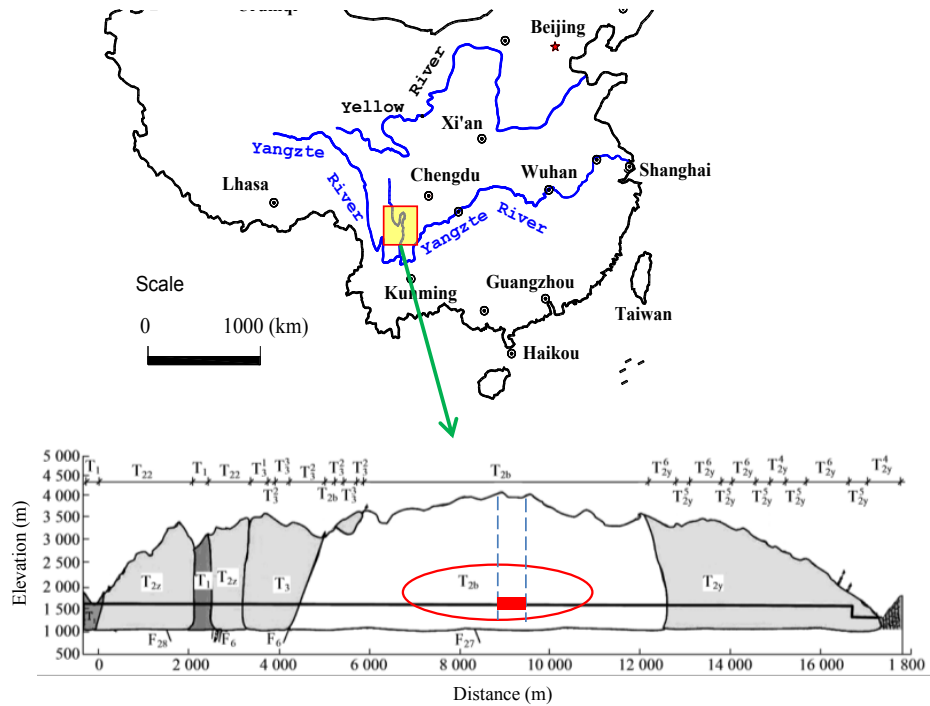


Figure 2. Location of the T_{2b} marble in the Jinping II hydropower station.

China (see Fig.2). For the purposes of getting the elastic parameters at a different loading stage, a loading-unloading triaxial test was conducted on the MTS815.03 test machine. In order to avoid the sudden energy release and brittle failure caused by post-peak unloading of rock in an unstable state, a special control method was used (see Fig.3). The confining pressure was increased by 1 MPa, followed by an unloading process during which the extra confining pressure was again decreased.

The loading process is controlled by deformation and the loading rate is 0.06 mm/min. The unloading process is controlled by the axial stress and the unloading rate is 26MPa/min. At the end of each unloading the deviatoric pressure is close to 5MPa. Fig.4 shows the stress-strain

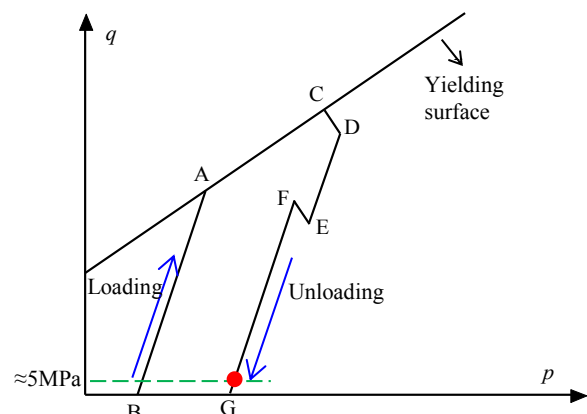


Figure 3. Loading and unloading stress path in the p - q plane.

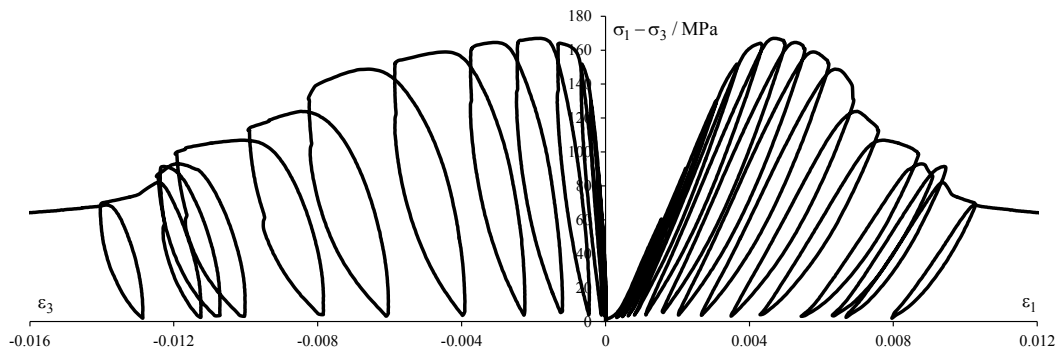


Figure 4. Loading and unloading stress-strain curve under the confining pressure of 5MPa.

curve under the 5MPa confining pressure. The elastic modulus decreases, while the plastic deformation increases with the loading process. As is well known, the weakness of the elastic modulus is related to the evolution of the damage. Thus, the elastoplastic damage evolution is accompanied by the loading process of the T_{2b} marble. Fig.5 shows the envelope line for the loading-unloading test curve. The envelope line also stands for the yield surface before the yield and the subsequent yield surface after the yield.

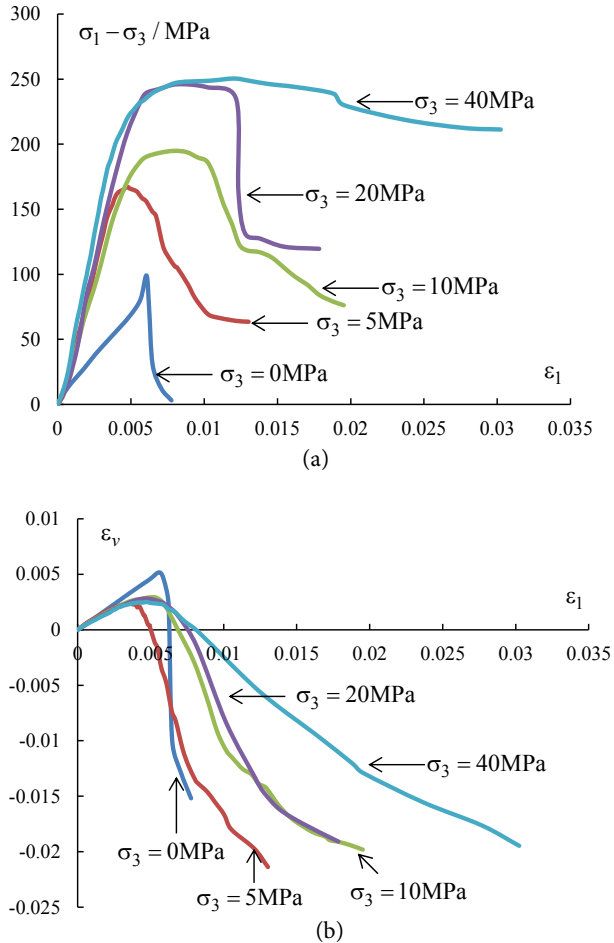


Figure 5. Envelope line of the loading-unloading test curve of the T_{2b} marble: (a) axial stress–axial strain curve. (b) volumetric strain–axial strain curve.

2.2 Test result analysis

The plastic characters in the loading process can be seen from Fig.5: a) The stress-strain test curve is approximately linear under a low confining pressure. The elastic deformation at failure increases with the increasing confining pressure. After a threshold the test curve shows obvious non-linearity and plasticity. b) The confining pressure influences the strength and the

deformation. With the increasing confining pressure, the strength and axial strain increases, while the volumetric strain seems restrained. c) In the case of a low confining pressure, the sample fails in a strain softening character, while strain hardening shows for the high confining pressure. d) There is a transition from volumetric compression to dilation. At first, the micro-fissures were compressed. Then the loading propagates the cracks after a threshold and dilation occurs. However, with the increasing confining pressure, the dilation is slow to happen and appears to be suppressed.

In the meantime, the fissures in the T_{2b} marble have such a sequence of evolution due to damage: a) Under low applied loading stress, the microcracks are compressed and the volume decreases. b) With the increasing loading stress, local instability leads to mesoscopic fracture. c) Mesoscopic fracture propagates and extends. d) The mesoscopic fracture develops into the penetrating crack and the sample fails.

To sum up, there is a coupling elastoplastic and damage effect in the loading process of the T_{2b} marble. When the load is not large enough, the microfissures are compressed and the material is elastic. With the increasing loading pressure, cracks propagate and dislocation occurs. Plastic deformation induces damage and, conversely, there is a further development of the plastic deformation. Therefore, it is necessary to use the coupled elastoplastic damage theory in the loading analysis of the T_{2b} marble[10].

3 ELASTOPLASTIC DAMAGE-COUPLING MODEL

There is no obvious anisotropic character in T_{2b} marble. So the isotropic theory is used in the analysis. It is presumed that the weakness due to the mesoscopic fissures can be described by the macroscopical isotropic damage. The damage process is defined by the damage variable in a scalar form. Under isothermal conditions, the state variables in the loading process are listed as the total strain tensor ϵ , the damage variable ω , the elastic strain tensor ϵ^e and the plastic strain tensor ϵ^p . The full variable form and incremental form of strain can be expressed

$$\epsilon = \epsilon^e + \epsilon^p, d\epsilon = d\epsilon^e + d\epsilon^p \quad (1)$$

It is assumed that there is a thermodynamic potential coupling the damage and plasticity. The thermodynamic potential can be expressed as

$$\psi = \frac{1}{2} \epsilon^e : \mathbb{C}(\omega) : \epsilon^e + \psi_p(\kappa, \omega) \quad (2)$$

where ψ_p is the thermodynamic potential describing the strain hardening of the damaged material. κ is the internal variable for plastic hardening, which can be described by the plastic deformation, such as the plastic strain or the equivalent plastic shear strain. $\mathbb{C}(\omega)$ is the fourth order of the elastic tensor. For isotropic material, $\mathbb{C}(\omega)$ is expressed as [11]

$$\mathbb{C}(\omega) = 2G(\omega)\mathbb{K} + 3K(\omega)\mathbb{J} \quad (3)$$

where G and K are the shear modulus and bulk modulus, respectively. \mathbb{K} and \mathbb{J} are the isotropic fourth tensor, which can be expressed as

$$\mathbb{K} = \mathbb{I} - \mathbb{J}, \mathbb{J} = \frac{1}{3} \delta \otimes \delta \quad (4)$$

where δ is a second-order unit tensor. \mathbb{I} is a symmetric fourth-order unit tensor. For a second-order tensor E , we have $\mathbb{J} : E = \frac{1}{3}(trE)\delta$, $\mathbb{K} : E = E - \frac{1}{3}(trE)\delta$.

The partial derivative operation is done with equation (2) and we have

$$\sigma = \frac{\partial \Psi}{\partial \varepsilon^e} = \mathbb{C}(\omega) : \varepsilon^e \quad (5)$$

Considering the damage to the elastic parameters, thus equation (5) can be rewritten in incremental form as

$$d\sigma = \mathbb{C}(\omega) : d\varepsilon^e + \frac{\partial \mathbb{C}(\omega)}{\partial \omega} : \varepsilon^e d\omega \quad (6)$$

3.1 Damage description

In the framework of the irreversible energy, many damage models have been established. In these models, the damage evolution is determined by the evolution function with a damage variable. The test shows that there is a shear bond penetrating the sample and particles slide along the microcrack with damage evolution. Thus, in this paper the damage driving force Y_ω is

$$Y_\omega = \int \sqrt{\frac{2}{3} de : de} \quad (7)$$

where de is the incremental form of deviatoric strain expressed as $de = d\varepsilon - \frac{1}{3}(trd\varepsilon)\delta$.

Inspired by the damage model proposed by Mazars[12], in this paper the damage evolution function is

$$f_\omega = \omega - \omega_{\max} \left(1 - \frac{1}{\exp[B_c(Y_\omega - Y_{\omega 0})]} \right) = 0 \quad (8)$$

where ω_{\max} is the maximum damage variable. The parameter B_c controls the kinetics of the compressive damage

and can be determined by using a uniaxial compression test. The parameter $Y_{\omega 0}$ is the damage threshold. To sketch the damage evolution during the loading process, the damage-evolution curve for the T_{2b} marble under a confining pressure of 40MPa is shown in Fig.6.

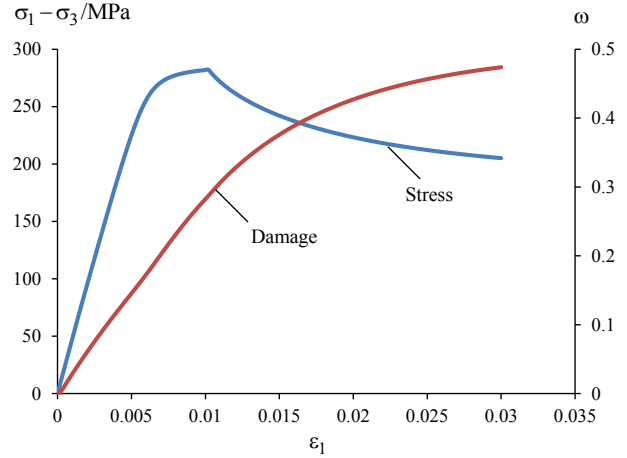


Figure 6. Damage-evolution curve for T_{2b} marble under confining pressure of 40MPa.

3.2 Plasticity description

According to the test research, rock has the characteristic of pressure sensitivity[13]. In other words, the strength increases with the increasing confining pressure or hydrostatic pressure. In this paper, the value of the variable is positive when the stress is tensile. Inspired by Chen et al., the strength criterion is adopted as

$$c_1 \frac{q}{g(\theta)f_{c0}} + c_2 \left(\frac{q}{g(\theta)f_{c0}} \right)^2 - \left(c_3 - \frac{p}{f_{c0}} \right) = 0 \quad (9)$$

where p is the hydrostatic pressure expressed as $p = \frac{1}{3} tr(\sigma)$. q is the equivalent shear stress expressed as

$q = \sqrt{\frac{3}{2} S : S}$. S is the deviatoric shear tensor expressed as $S = \sigma - \frac{1}{3}(tr\sigma)\delta$. f_{c0} is the uniaxial strength determined by the uniaxial test. The parameters c_1 , c_2 and c_3 define the curvature of the failure surface and can be determined by plotting the failure surface. $g(\theta)$ determines the effect of the Lode angle on the strength. In the loading path in this paper, $g(\theta)$ is simplified as $g(\theta)=1$. It is noted that equation (9) is the Drucker-Prager criterion in the case of $c_2=0$ for the simplified calculation.

The loading equation similar to equation (9) is

$$f_s = q - \alpha_s g(\theta) \bar{\sigma}_c = 0 \quad (10)$$

where $\bar{\sigma}_c = \frac{(-c_1 + \sqrt{c_1^2 + 4c_2(c_3 - p/f_{c0})})}{2c_2} f_{c0}$.

$\alpha_s = \alpha_0 + (1 - \alpha_0) \frac{\gamma_p}{B + \gamma_p}$. α_0 controls the threshold of plasticity. B controls the kinetics of the compressive plasticity, which is determined by the evolution law of α_s and γ_p . γ_p is the equivalent plastic shear strain expressed as

$$\gamma_p = \int \sqrt{\frac{2}{3} de^p : de^p} \quad (11)$$

$$de^p = d\varepsilon^p - \frac{1}{3} (tr d\varepsilon^p) \delta \quad (12)$$

when $\gamma_p \rightarrow 0$, $\alpha_s \rightarrow \alpha_0$. For $\gamma_p \rightarrow \infty$, $\alpha_s \rightarrow 1$.

The generation of microcracks is accompanied by the plastic deformation. To express the weakness the loading function is expressed as

$$f_s = q - \alpha_s g(\theta) \frac{\left(-c_1 + \sqrt{c_1^2 + 4c_2(c_3 - p / \bar{f}_{c0})}\right)}{2c_2} \bar{f}_{c0} = 0 \quad (13)$$

where $\bar{f}_{c0} = f_{c0} (1 - \langle \omega - \omega_f \rangle)$, ω_f is the threshold of the damage to the plasticity. When the damage variable is larger than ω_f , the loading curve shrinks and the strength decreases. The symbol $\langle x \rangle$ is expressed as: $\langle x \rangle = 0$ when $x \leq 0$ and $\langle x \rangle = x$ when $x > 0$.

The test shows that the volumetric deformation changes from compression to dilation and this effect decreases with the increasing confining pressure. To express the deformation character, inspired by the work [14, 15], the plastic potential function is

$$g_s = q + \mu_s g(\theta) I \ln \left(\frac{I}{I_0} \right) = 0 \quad (14)$$

where $I = -p + c_3 \bar{f}_{c0}$. The parameter I_0 determines the intersection point of the plastic potential surface and the coordinate p . The threshold of the volumetric compression to dilation can be determined by $\frac{\partial g_s}{\partial I} = 0$, expressed as

$$f_{sw} = q - \mu_s g(\theta) (-p + c_3 \bar{f}_{c0}) = 0 \quad (15)$$

where the parameter μ_s defines the slope of the boundary between the compressibility and dilatancy domains. Its value can be obtained by plotting the transition boundary line in the p - q plane.

3.3 The damage and plasticity coupling numerical process

In a general loading path, the plastic flow and damage evolution can be activated regarding the loading law, respectively. There are two kinds: a) $d\omega > 0, f_s = 0$. b) $d\omega > 0, f_s < 0$.

3.3.1 (a) $d\omega > 0, f_s = 0$

In this case, the plastic flow and the damage evolution are activated. The damage variable increment is determined by

$$\begin{aligned} d\omega &= d\lambda_\omega \frac{\partial f_\omega}{\partial Y_\omega} \\ &= d\lambda_\omega \frac{-\omega_{\max} B_c}{\exp[B_c(Y_\omega - Y_{\omega 0})]} \end{aligned} \quad (16)$$

where $d\lambda_\omega$ is the damage multiplier, which can be determined by the damage-consistency condition

$$\begin{aligned} df_\omega &= \frac{\partial f_\omega}{\partial Y_\omega} dY_\omega + \frac{\partial f_\omega}{\partial \omega} d\omega \\ &= \frac{-\omega_{\max} B_c}{\exp[B_c(Y_\omega - Y_{\omega 0})]} \left(\frac{\partial Y_\omega}{\partial \varepsilon^e} : d\varepsilon^e + \frac{\partial Y_\omega}{\partial \varepsilon^p} : d\varepsilon^p \right) + d\omega = 0 \end{aligned} \quad (17)$$

From equations (16) and (17) we have

$$d\lambda_\omega = - \left(\frac{\partial Y_\omega}{\partial \varepsilon^e} : d\varepsilon^e + \frac{\partial Y_\omega}{\partial \varepsilon^p} : d\varepsilon^p \right) \quad (18)$$

For plasticity, the plastic strain increment is

$$d\varepsilon^p = d\lambda_s \frac{\partial g_s}{\partial \sigma} \quad (19)$$

where $d\lambda_s$ is the plastic multiplier, which can be determined by the plastic consistency condition as

$$df_s = \frac{\partial f_s}{\partial \sigma} : d\sigma + \frac{\partial f_s}{\partial \gamma_p} \frac{\partial \gamma_p}{\partial \varepsilon^p} : d\varepsilon^p + \frac{\partial f_s}{\partial \omega} d\omega = 0 \quad (20)$$

From equations (19) and (20), the plastic multiplier is determined as

$$d\lambda_s = - \frac{\frac{\partial f_s}{\partial \sigma} : d\sigma + \frac{\partial f_s}{\partial \omega} d\omega}{\frac{\partial f_s}{\partial \gamma_p} \frac{\partial \gamma_p}{\partial \varepsilon^p} : \frac{\partial g_s}{\partial \sigma}} \quad (21)$$

Substitute (16) into (21) and (19) into (18), the simultaneous equations are obtained and thus we get the plastic multiplier and the damage multiplier. The constitutive function in incremental form can be expressed as

$$\begin{aligned} d\sigma &= \mathbf{C}(\omega) : \left(d\varepsilon - d\lambda_s \frac{\partial g_s}{\partial \sigma} \right) \\ &- d\lambda_\omega \frac{\omega_{\max} B_c}{\exp[B_c(Y_\omega - Y_{\omega 0})]} \frac{\partial \mathbf{C}(\omega)}{\partial \omega} : \varepsilon^e \end{aligned} \quad (22)$$

3.3.1 (b) $d\omega > 0, f_s < 0$

For $f_s < 0$, the stress point is in the elastic range and no plastic flow happens. $d\omega > 0$ and there is only damage evolution. Accordingly, the plastic strain increment is

0. Therefore, $d\varepsilon^p=0$. The damage-variable increment is expressed as equation (16). Similar to equation (17), the damage-consistency condition is expressed as

$$df_{\omega} = \frac{\partial f_{\omega}}{\partial Y_{\omega}} dY_{\omega} + \frac{\partial f_{\omega}}{\partial \omega} d\omega$$

$$= \frac{-\omega_{\max} B_c}{\exp[B_c(Y_{\omega} - Y_{\omega 0})]} \left(\frac{\partial Y_{\omega}}{\partial \varepsilon^e} : d\varepsilon^e \right) + d\omega = 0 \quad (23)$$

From equation (16) and (23), the damage multiplier is derived

$$d\lambda_{\omega} = -\frac{\partial Y_{\omega}}{\partial \varepsilon^e} : d\varepsilon^e \quad (24)$$

For the elastic strain to equal the total strain in the elastic loading, that is

$$d\varepsilon^e = d\varepsilon \quad (25)$$

From equations (24) and (25) we get

$$d\lambda_{\omega} = -\frac{\partial Y_{\omega}}{\partial \varepsilon} : d\varepsilon \quad (26)$$

Thus, the constitutive equation is

$$d\sigma = \mathbb{C}(\omega) : d\varepsilon - d\lambda_{\omega} \frac{\omega_{\max} B_c}{\exp[B_c(Y_{\omega} - Y_{\omega 0})]} \frac{\partial \mathbb{C}(\omega)}{\partial \omega} : \varepsilon \quad (27)$$

4 NUMERICAL SIMULATION AND VALIDATION

The parameters in the model are determined in three steps. a) The plastic parameters are determined by only considering the plastic mechanism. b) The damage parameters are determined with the plastic parameters. c) The plastic parameters are adjusted according to the failure. In the model, the last step accomplishes coupling the damage and plastic by introducing \bar{f}_{c0} in equation (13). In details, the parameters of the model can be determined by the test following the steps: a) The uniaxial compressive strength f_{c0} is determined by the uniaxial compression test. b) Neglecting damage process, at the initial yield, no plasticity formulates. For simplicity, the peak strength in the triaxial compression test with different confining pressures is viewed as an initial yield stress. The yield criterion parameters c_1 , c_2 and c_3 could be determined by using equation (9) according to the peak strength. c) After the initial yield, plasticity formulates with the plastic deformation represented by γ_p . According to the strain-hardening phase, the parameter B can be obtained by the evolution law of $\alpha_s(\gamma_p)$. d) Find out the stress with the corresponding volumetric strain rate equal to zero. The stress state means a transition from the volumetric compressibility

to the dilatancy. The transition boundary line between the compressibility and dilatancy domains is sketched in the p - q plane and the parameter μ_s is obtained. e) The damage parameters are considered after the determination of the plastic parameters. The softening phase is dominated by the damage in equation (13). With the softening stress-strain test data, the damage-evolution law and the parameter B_c are determined.

The triaxial test of the T_{2b} marble is simulated using the proposed model. The parameters in the model are listed in Table 1. Fig.7 shows the consistency between the simulation result and test curve. According to the simulation results it can be inferred: a) Brittleness is more obvious under a low-confining pressure. The stress falls down after the peak in the strength. In this condition the damage mechanism generally works (see Fig.7(a)). b) The ductile character is revealed under a high confining pressure. There is no obvious stress fall after the peak strength. In this case the plastic mechanism generally works (see Fig.7(c)). c) The strength and strain increase with the increasing confining pressure. d) There is a transition between the volumetric compression and the dilation. The dilation under the confining pressure 40MPa is not as obvious as 5MPa. The confining pressure restrains the dilation. Fig.8 shows the loading and unloading test and simulation results. The hysteresis loop occurred in the compression phase of the cyclic loading and unloading test. This loop results from the frictional movement of the particles during the cyclic loading and unloading. Because in the proposed model there is no plasticity and damage accumulation, the re-loading curve coincides with the unloading diagram. Both the simulation and test represent the elastic stiffness decrease in the loading process. There is a deviation between the simulation result and test curve, but the proposed model can express the mechanical characters of the brittle hard rock in a qualitative manner. This would have significance for a stability analysis of deep buried tunnels.

Table 1. Parameters in the proposed model.

Parameter type	Parameter value
Elastoplastic parameter	$f_{c0} = 99\text{MPa}$
	$c_1 = 0.2$
	$c_2 = 0.1$
	$c_3 = 0.05$
	$B = 9 \times 10^{-5}$
Damage parameter	$\mu_s = 1.4$
	$B_c = 85$

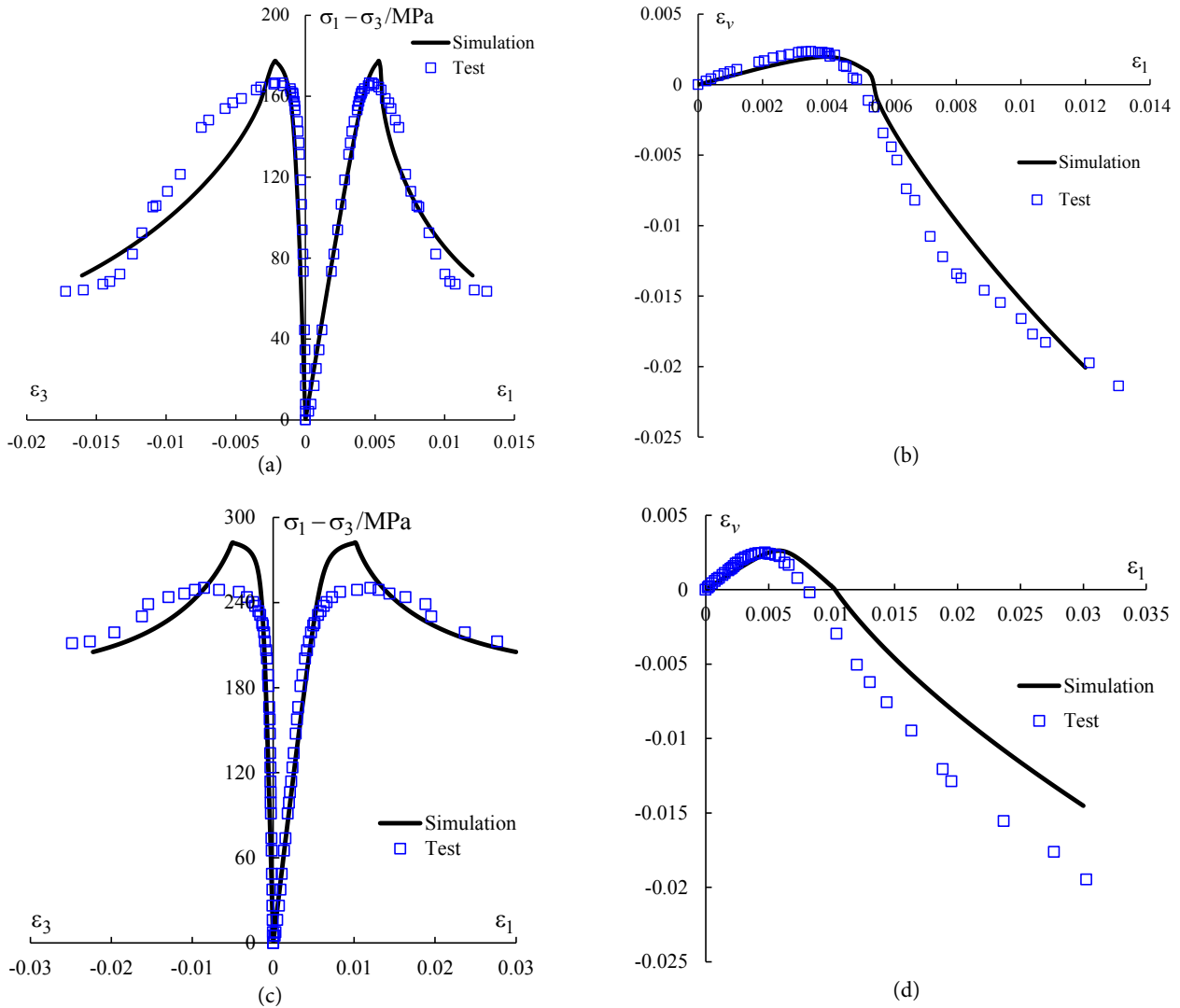


Figure 7. Simulation results and test curves: (a) axial stress-axial strain curve under confining pressure of 5MPa. (b) volumetric strain-axial strain curve under confining pressure of 5MPa. (c) axial stress-axial strain curve under confining pressure of 40MPa. (d) volumetric strain-axial strain curve under confining pressure of 40MPa.

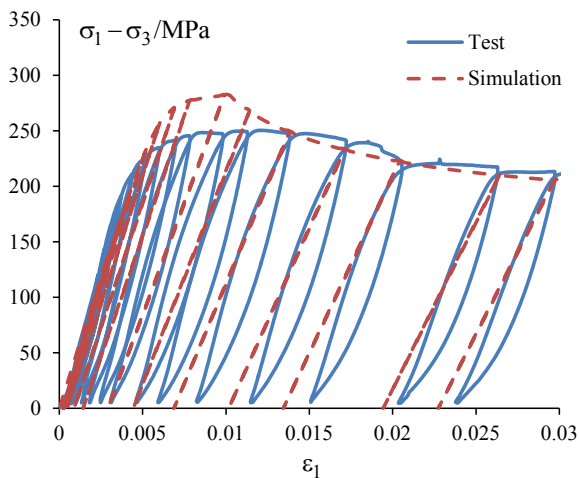


Figure 8. Simulation and test results of the loading and unloading process.

5 CONCLUSIONS

A tri-axial test is conducted in an analysis of deep buried T_{2b} marble. The hard rock in this study shows obvious pressure sensitivity and dilation. The strength and failure strain increase with the increasing confining pressure. At the same time, the dilation is suppressed and the non-linear character becomes more obvious. Based on the influence of the damage and plastic mechanism in the test, the damage-evolution function is proposed to reflect the mechanical weakness with the damage. Considering the influence of damage on the plasticity, the plastic-loading function and the plastic potential function are established. According to the activation law of the damage and plasticity, the elastoplastic damage constitutive function is proposed. The parameters of the

model are determined using a conventional tri-axial test. Then the model is verified by a simulation of the test curve. The proposed model can express the mechanical characters of deep buried hard rock in an accurate way.

Acknowledgments

We gratefully acknowledge financial support from National Natural Science Foundation of China (NSFC) (51704097), the Project of Key Opening Laboratory for Deep Mining Construction at Henan province (2015 KF-06), the Key Scientific Research Project of Henan Higher Education Institutions (16A560004), Dr. Fund Projects of Henan Polytechnic University (B2016-65) and the cooperative program between HPU and UL.

REFERENCES

- [1] Zhou, H., Zhang, C.Q., Li, Z., et al. 2014. Analysis of mechanical behavior of soft rocks and stability control in deep tunnels. *Journal of Rock Mechanics and Geotechnical Engineering* 6(3), 219-226. DOI: 10.1016/j.jrmge.2014.03.003
- [2] Zhang, C.S., Liu, N., Chu, W.J. 2016. Key technologies and risk management of deep tunnel construction at Jinping II hydropower station. *Journal of Rock Mechanics and Geotechnical Engineering* 8(4), 499-512. DOI: 10.1016/j.jrmge.2015.10.010
- [3] Li, Z., Zhou, H., Song, Y.Z., et al. 2013. Mechanical model of chlorite schist considering hardening-softening and dilatancy characteristics. *Rock and Soil Mechanics* 34(2), 404-410. DOI: 10.16285/j.rsm.2013.02.017
- [4] Singh, M., Raj, A., Singh, B. 2011. Modified Mohr-Coulomb criterion for non-linear triaxial and polyaxial strength of intact rocks. *International Journal of Rock Mechanics and Mining Sciences* 48(4), 546-555. DOI: 10.1016/j.ijrmms.2011.02.004
- [5] Cicekli, U., Voyiadjis, G.Z., Al-Rub, R.K.A. 2007. A plasticity and anisotropic damage model for plain concrete. *International Journal of Plasticity* 23(10), 1874-1900. DOI: 10.1016/j.ijplas.2007.03.006
- [6] Salari, M.R., Saeb, S., Willam, K.J., et al. 2004. A coupled elastoplastic damage model for geomaterials. *Computer Methods in Applied Mechanics and Engineering* 193(27), 2625-2643. DOI: 10.1016/j.cma.2003.11.013
- [7] Chiarelli, A.S., Shao, J.F., Hoteit, N. 2003. Modeling of elastoplastic damage behavior of a claystone. *International Journal of Plasticity* 19(1), 23-45. DOI: 10.1016/S0749-6419(01)00017-1
- [8] Zhu, Q.Z., Shao, J.F., Mainguy, M. 2010. A micromechanics-based elastoplastic damage model for granular materials at low confining pressure. *International Journal of Plasticity* 26(4), 586-602. DOI: 10.1016/j.ijplas.2009.09.006
- [9] Zhou, C.Y., Zhu, F.X. 2010. An elasto-plastic damage constitutive model with double yield surfaces for saturated soft rock. *International Journal of Rock Mechanics and Mining Sciences* 47(3), 385-395. DOI: 10.1016/j.ijrmms.2010.01.002
- [10] Zhou, H., Zhang, K., Feng, X.T. 2011. A coupled elasto-plastic-damage mechanical model for marble. *Science China Technological Sciences* 54(1), 228-234. DOI: 10.1007/s11431-011-4642-3
- [11] Chen, W.F., Saleeb, A.F. 1994. *Constitutive equations for engineering materials: elasticity and modeling*. Elsevier, Amsterdam.
- [12] Mazars, J. 1984. *Application de la mécanique de l'endommagement au comportement non linéaire et à la rupture du béton de structure*. Université Paris VI, France.
- [13] Aubertin, M., Li, L., Simon, R., et al. 1999. Formulation and application of a short-term strength criterion for isotropic rocks. *Canadian Geotechnical Journal* 36(5), 947-960. DOI: 10.1139/t99-056
- [14] Shao, J.F., Jia, Y., Kondo, D., et al. 2006. A coupled elastoplastic damage model for semi-brittle materials and extension to unsaturated conditions. *Mechanics of Materials* 38(3), 218-232. DOI: 10.1016/j.mechmat.2005.07.002
- [15] Jia, Y., Bian, H.B., Su, K., et al. 2010. Elastoplastic damage modeling of desaturation and resaturation in argillites. *International Journal for Numerical and Analytical Methods in Geomechanics* 34(2), 187-220. DOI: 10.1002/nag.819

PREDICTING THE UPLIFT CAPACITY OF VERTICALLY LOCATED TWO-PLATE ANCHORS

NAPOVEDOVANJE IZVLEČNE NOSILNOSTI NAVPIČNIH SIDER Z DVEMA PLOŠČAMA

Gizem Misir

Karamanoglu Mehmetbey University,
Department of Civil Engineering
Karaman, 70100, Turkey
E-mail: gmisir@kmu.edu.tr

DOI <https://doi.org/10.18690/actageotechslov.15.2.47-57.2018>

Keywords

pullout capacity; Plaxis 2D; two-plate anchors; design approach; regression analysis

Ključne besede

izvlečna nosilnost; Plaxis 2D; sidra z dvema ploščama; pristop oblikovanja; regresijska analiza

Abstract

Soil anchors are generally used for structures that are subjected to pullout forces, such as offshore floating bodies, transmission towers, structures requiring lateral resistance or submerged platforms etc. Multi-plate anchors are used as a foundation that apply either large compression or tension forces using a number of plates welded along a central shaft. These anchors that have more than one plate have a complex interaction between the adjacent plates due to over applying stress zones. Therefore, this interaction affects the failure mechanism and the uplift capacity of the system. However, no thorough numerical analyses have been performed to determine the ultimate pullout loads of multi-plate anchors. By far the majority of the research has been directed towards the tensile uplift behavior of one-plate single anchor. Estimating the uplift capacity by using a practical design method that is obtained from a numerical analysis of two-plate anchors in sand is described in this paper. This method can be used more confidently by design engineers to estimate the pullout capacity of two-plate anchors under tension loading. The theoretical results are compared with the numerical data and acceptable values are obtained.

Izvleček

Sidra v zemljinah se običajno uporabljajo za konstrukcije, ki so obremenjene z izvlečnimi silami, kot so plavajoča telesa na odprtem morju, stolpi električnih vodov, konstrukcije z bočnim odporom ali potopljene ploščadi itd. Sidra z več ploščami se uporabljajo kot temelj, ki lahko prenese velike tlačne ali natezne sile z uporabo več plošč varjenih vzdolž osrednje gredi. Sidra, ki imajo več kot eno ploščo, imajo kompleksno interakcijo med sosednjimi ploščami zaradi medsebojnega prekrivanja napetostnih vplivnih območij. Zato ta interakcija vpliva na porušitveni mehanizem in izvlečna nosilnost sistema. Natančna numerična analiza, s katero bi ugotovili mejno nosilnost sider z več ploščami, ni bila opravljena. Večji del raziskav je bil usmerjen v ugotovitev obnašanja natezne obremenjenega samostojnega sidra z eno ploščo glede na izvelek. V tem prispevku je opisan način ocenitve izvlečna nosilnosti z uporabo praktične metode načrtovanja, ki jo dobimo iz numerične analize sider z dvema ploščama v pesku. To metodo lahko inženirji bolj zanesljivo uporabljajo za načrtovanje ocenitve izvlečne nosilnosti sider z dvema ploščama pri natezni obremenitvi. Rezultati teoretičnih izračunov se sprejemljivo ujemajo z rezultati numeričnih analiz.

1 INTRODUCTION

Many structures experience overturning moments due to lateral loads, which result in a combination of tension and compression responses at the foundation level. The design of such structures needs various systems to resist the uplift forces. Under such conditions, effective and safe design methods can be achieved through the use of tension elements. These elements are referred to as ground anchors. The elements are typically fixed to the structure and embedded into the soil to effective depths, so that they can resist the uplift loads. Soil anchors are typically used for retaining walls, transmission towers, foundations, sea walls, pipelines, etc. The soil anchors involved are of different types, such as screw anchors, grout-injected anchors, anchor plates and anchor piles. The use of different types of anchors is dependent on the magnitude and type of loading, the type of structure and the sub-soil conditions. Multi-plate anchors are also geotechnical foundations that can be used as either tension or compression members to resist the forces listed above, composed of a number of plates welded along a central steel shaft. The anchors can have more than one plate located at an appropriate spacing on the shaft. The uplift capacity of the multi-plate anchor system is dependent on the number of plates. The central shaft is used to transfer axial loads to the anchor plates. Unfortunately, the current understanding regarding the behavior of buried foundations, and multi-plate anchors in particular, is unsatisfactory and has remained essentially unchanged for about 20 years. There have been numerous theoretical/experimental studies that address the uplift of single horizontal anchors. In contrast, there are very few publications that deal with the theoretical problem of multi-plate anchor foundations.

In the literature, the uplift capacities of horizontal (plate/helical) anchors have been investigated by many researchers (Mitsch and Clemence [1], Ghaly et al. [2], Meyerhof and Adams [3], Das [4,5], Ilamparuthi et al. [6], Dickin and Laman [7], Rowe and Davis [8], Bildik and Laman [9], Zhang et al. [10], Tang and Phoon [11], Demir and Ok [12], Nazir et al. [13], Mittal and Mukherjee [14], Mokhbi et al. [15], Papadopoulou et al. [16], Schiavon et al. [17], Tsuha et al. [18]). The failure mechanisms and pullout resistances have also been examined theoretically or experimentally. Hanna et al. [19] investigated the pullout resistance of single vertical shallow helical and plate anchors. The analytical results were compared with the experimental results of Ilamparuthi et al. [6] and Ghaly et al. [20], and they observed higher breakout factor values in the helical type of anchor compared with the circular plate anchor. But in contrast, there are very few publications that deal with the uplift behavior of multi-plate anchor systems.

Merifield [21] developed a numerical modeling technique to understand the uplift behavior of the multi-plate circular anchor in clay soil. The established design framework for multi-plate anchor foundations was compared with Narashime and Rao's [22, 23] experimental results, and it was shown that the existing semi-empirical design methods have been excessively under- or over-conservative. Merifield and Smith [24] presented a study about the behavior of the multi-plate plain-strain anchor based on numerical modelling techniques. They used the finite-element software Abaqus. A practical and straightforward design framework was presented to predict the ultimate uplift capacity of the plane-strain multi-plate anchor foundations buried in undrained soils.

This paper presents an empirical method that was developed from a numerical analysis to predict the uplift capacity of a two-plate anchor system with different embedment depths and spacing ratios in the sand. The numerical analyses were performed by using the finite-element package PLAXIS 2D, which was developed for an analysis of deformation and stability problems in geotechnical engineering. The results of the numerical analyses were modified with regression analyses and a practical design method was developed to determine the uplift capacity of the two-plate anchor system, because the desired vertical movement provides realistic results for the parameters considered in this study. It is expected that the developed approach presented in this study will provide an alternative solution for the design and applications of geotechnical engineers, together with an increase in the simplicity and a gain in time.

2 FINITE-ELEMENT MODELLING

The numerical analyses were performed by using the finite-element software PLAXIS 2D-V8.2 as an axisymmetric problem. This software is especially useful for the analysis of deformation and the stability of complex geotechnical engineering problems (Brinkgreve and Vermeer [25]). Additionally, this numerical analysis technique is well established and widely used in many researches and case studies of geotechnical applications by modelling the realistic constitutive behavior of the soils. The finite-element method can also be generally used for identifying the patterns of deformations and stress distributions at the ultimate state or allowable service load. Because of these capabilities of the finite-element method, it is possible to model the construction method and investigate the behavior of the uplift of anchor plates and the surrounding soil throughout the construction process, not just for the limit equilibrium conditions (Laman and Yildiz [26]).

Single and multi-plate anchors are generally designed with a central shaft to transfer the axial loads from the anchor plates to the structure. In this study, single and double circular rigid plates were used to obtain the uplift forces in relation to different embedment and spacing ratios. The layout of the model geometry is shown in Figure 1. The anchor system has a total of 1 or 2 individual plates of the same diameter D and the same plate thickness (t_p). The depth of the upper-plate embedment is shown as “ H ”, while the distance between the plates is shown as “ s ” in the two-plate anchor system. Therefore, the anchor spacing ratio is defined as s/D and the anchor embedment ratio is defined as H/D .

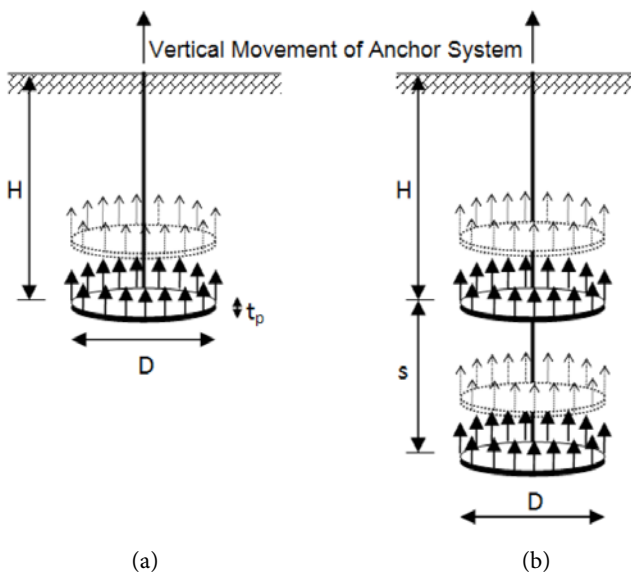


Figure 1. Mesh grid of topographic model.
(a) Single-plate anchor; (b) Two-plate anchors

The one-plate anchor system was modelled to obtain the reference bearing capacities. In the analyses, the upper-plate depth (H/D) was changed from 1 to 7 and the spacing between the two plates (s/D) for each different H/D value was changed from 0.5 to 7. Consequently, 84 analyses were performed for this study. In the finite-element analysis the axi-symmetric model was used since the geometry and the loading conditions of the problem provide axi-symmetry. Only half of the geometry is considered in the PLAXIS 2D analysis of axi-symmetric problems. The thickness (t) and the diameter (D) of the plate were 1 cm and 20 cm, respectively. The soil was modelled as an isotropic elasto-plastic continuum with failure described by the Mohr-Coulomb yield criterion. The parameters of the sandy soil were listed in Table 1. The anchor was modelled as being much stiffer than the soil as a discrete plate element.

Table 1. Sand parameters used in the numerical analysis.

Parameters	Value
Unit weight, γ_n (kN/m ³)	17.00
Saturated Unit weight, γ_d (kN/m ³)	18.00
Cohesion, c' (kN/m ²)	0.01
Friction angle, ϕ' (degrees)	30.0
Dilatancy angle, ψ (degrees) ($\phi' - 30^\circ$)	0.00
Poisson's Ratio	0.25
Elasticity Modulus, E (kN/m ²)	30.000
R_{inter}	0.10

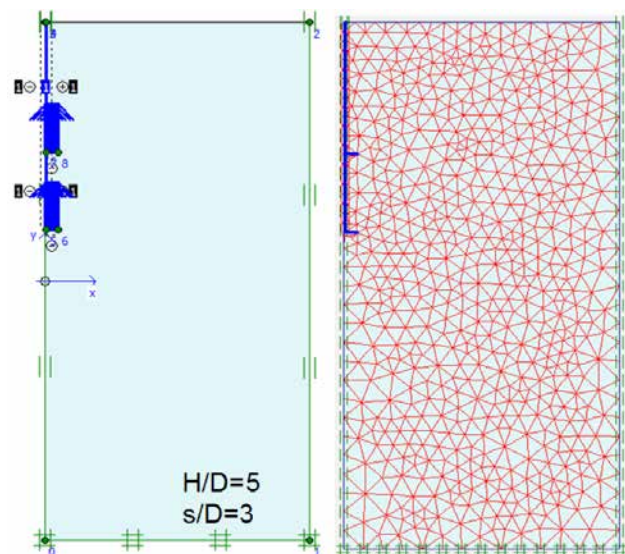


Figure 2. Typical finite-element mesh.

Although it is likely that, shaft friction contributes to the capacity, the term is generally ignored in the anchor design because of the uncertainties involved (Merifield [21]). So, the interface element was defined around the shaft and the interaction between the shaft and the surrounding soil was neglected. Also, the interaction was neglected between the plate bases and the soil under the plates (Fig 2).

The rationale of the finite-element method is one in which continuous media is divided into finite elements with different geometries. The mesh configuration can be generated automatically for the desired refinement and each element is compatible with the structural and interface elements. During the generation of the mesh, 15-node triangular elements were selected in preference, to provide greater accuracy in the determination of the

stresses. In this study, in order to select the suitable mesh refinement, preliminary analyses were conducted at five different mesh coarseness. The fine-mesh coarseness was used in all analyses, since there is a remarkable difference observed for the coarser mesh sizes. A typical finite-element mesh that is composed of the soil, multi-plate circular anchors, boundary conditions and the geometry of the model used, is shown in Fig. 2.

The uplift behavior of the plate anchor was analyzed by using the displacement-definition approach. The common opinion about the failure criteria is in the range of 10% of the plate’s diameter. However, the determination of the failure criteria was based on the comparisons of the experimental and theoretical results, as indicated in the literature (Sakr [27], Elsherbiny and Hesam El Naggar [28], Sakr [29]). The 5% displacement criterion has been recommended as a failure criterion to satisfy the serviceability requirements. For this purpose, the failure criterion was selected as 5% of the plate diameter (20 cm). Therefore, the vertical stresses above the horizontal plates were used to calculate the total ultimate load F_u , which was obtained against the 1-cm movement of the two-plate anchor system in the analyses.

3 NUMERICAL ANALYSIS

3.1 Single-Plate Anchor

The uplift capacity of the single-plate anchor at seven different embedment ratios (H/D) from 1 to 7 was analyzed using PLAXIS 2D. The results of the single-plate anchor analysis were only used to compare the results with the literature and to assess the performance change that would occur in a two-plate case. The analyses were performed until the collapse of the soil was observed. The criterion of the displacement-defined analysis was increased up to the collapse of the soil to obtain the same ultimate situation as in the literature. Uplift capacities are often expressed in dimensionless form as breakout factor (BF), as given below:

$$BF = \frac{F_u}{\gamma A_{pl} H} \tag{1}$$

where BF is the breakout factor, F_u is the maximum uplift resistance, γ is the soil unit weight, H and A_{pl} are the anchor embedment depth and plate area, respectively.

The graph in Figure 3 presents the variation of the relationship between the breakout factor and the embedment ratio (H/D) at a 30° constant angle of the shearing resistance of the soil, for a single-plate anchor in sand.

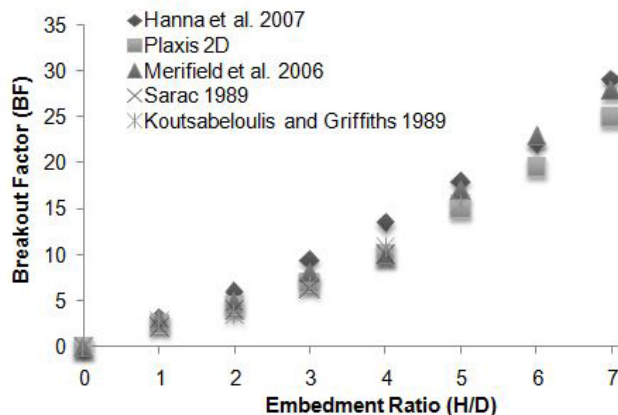


Figure 3. Comparison of the breakout factor for a single plate.

According to the graph, the breakout factor that was obtained from PLAXIS 2D are in accordance with the literature (Hanna et al. [19], Merifield et al. [30], Sarac [31], Koutsabeloulis and Griffiths [32]). The breakout factors obtained from the PLAXIS 2D are slightly below the results of the literature, especially at the large embedment depths. Consequently, the validation of the model and the parameters that are used in the analysis have been approved in the literature by dimensionless values.

3.2 Two-Plate Anchors

A total of 77 different analyses were performed. The analysis program is listed in Table 2. Evaluations were made at the maximum vertical stresses caused by a 1-cm plate’s movement. The stress distributions were presented together with the upper and lower plates, and they were compared with the single-plate condition for each embedment ratio, as seen in Figure 4.

Table 2. Analysis program.

Plate Diameter (D) cm	Constant Value	Variable Value									
		Embedment Ratio, H/D	Spacing Ratio, s/D								
20	1	0.5, 1.0, 1.5, 2.0, 2.5, 3.0, 3.5, 4.0, 5.0, 6.0, 7.0									
20	2	0.5, 1.0, 1.5, 2.0, 2.5, 3.0, 3.5, 4.0, 5.0, 6.0, 7.0									
20	3	0.5, 1.0, 1.5, 2.0, 2.5, 3.0, 3.5, 4.0, 5.0, 6.0, 7.0									
20	4	0.5, 1.0, 1.5, 2.0, 2.5, 3.0, 3.5, 4.0, 5.0, 6.0, 7.0									
20	5	0.5, 1.0, 1.5, 2.0, 2.5, 3.0, 3.5, 4.0, 5.0, 6.0, 7.0									
20	6	0.5, 1.0, 1.5, 2.0, 2.5, 3.0, 3.5, 4.0, 5.0, 6.0, 7.0									
20	7	0.5, 1.0, 1.5, 2.0, 2.5, 3.0, 3.5, 4.0, 5.0, 6.0, 7.0									

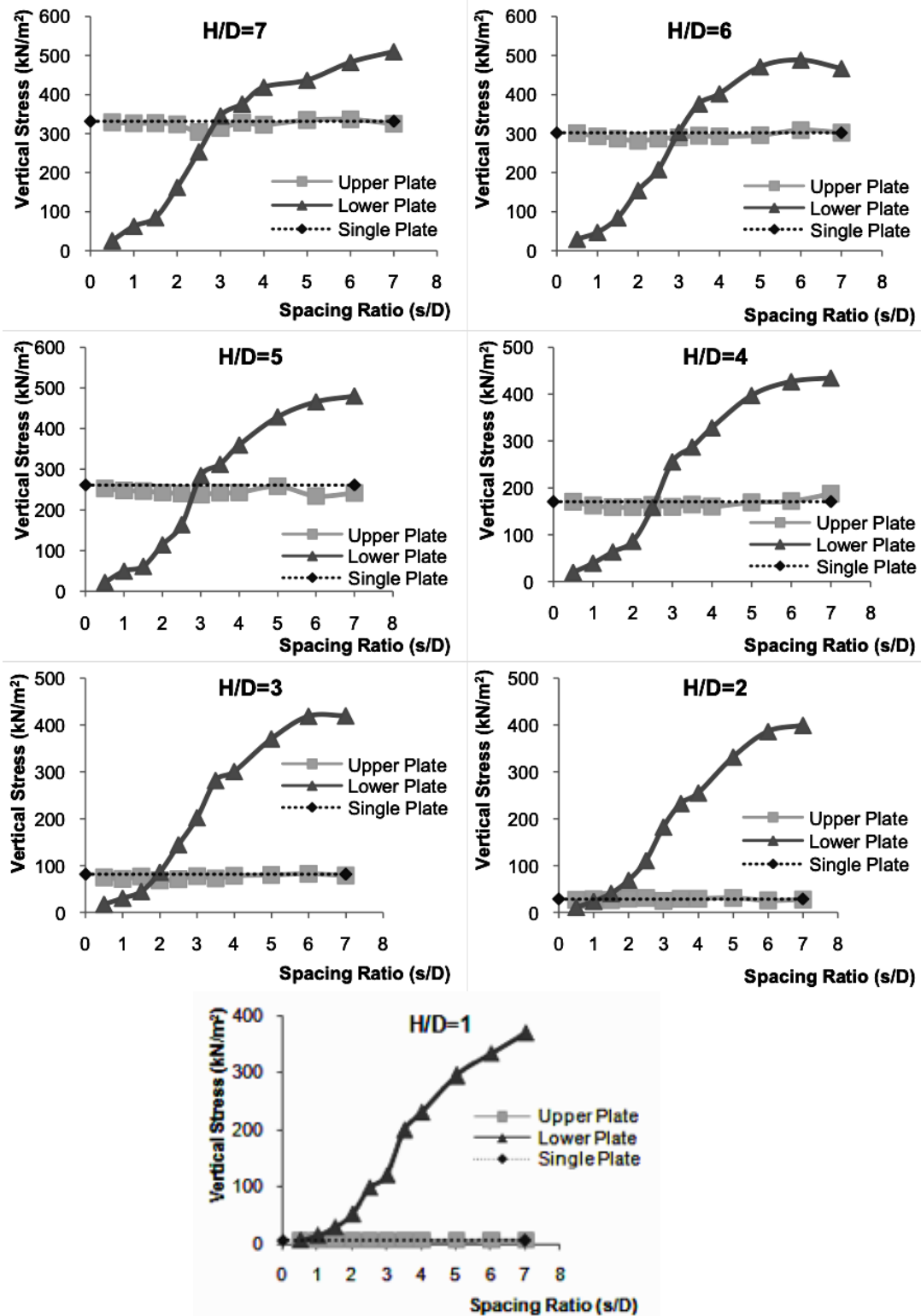


Figure 4. Vertical stress versus spacing ratio for the constant embedment ratios.

According to Figure 4, the maximum vertical stress (with a 5% vertical movement) on the single plate was obtained as being similar to the upper plate of the two-

plate anchor system at the same embedment depth ratio. An average absolute error of 3% was obtained for all the 7 embedment depth ratios.

While the upper-plate stresses were obtained about a constant value, independent of the spacing ratio, the lower-plate stresses were in a trend of increasing with an increase of the spacing ratio.

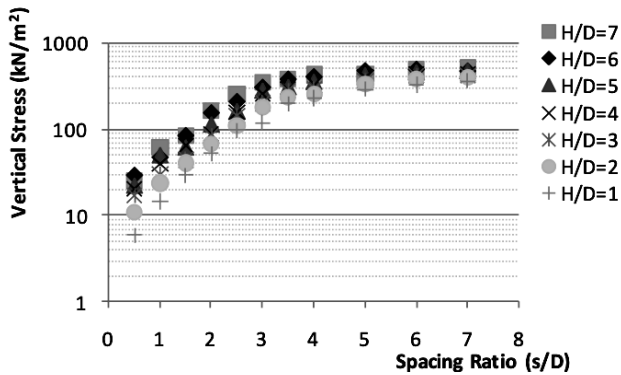
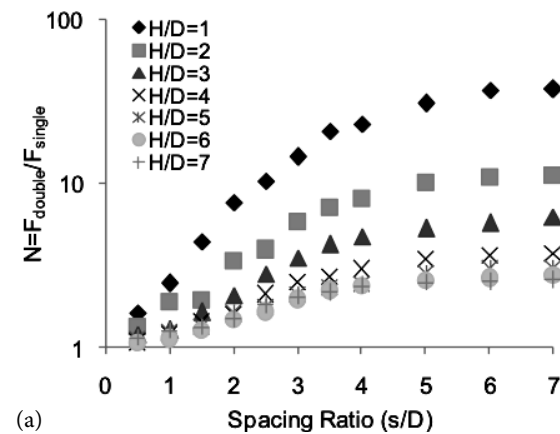
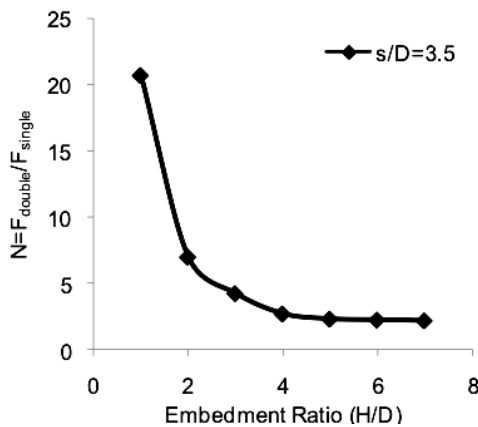


Figure 5. Vertical stress distribution at the bottom plate.



(a)



(b)

Figure 6. Performance variation.

(a) Two-plate case; (b) Optimum value ($s/D=3.5\%$)

The stress distribution in a logarithmic form on the lower plate was in a trend of increasing until a 3.5 spacing ratio and the trend of the stress was transformed into an asymptote for the larger values of the spacing ratios (Figure 5). It can be concluded that using a spacing value between the plates wider than $3.5D$ has no significant effect on the vertical stress on the lower plate. Therefore, the uplift capacity of the two-plate anchor system has become constant for a constant value of H/D and for any values of the spacing ratios $s/D > 3.5$.

The performance variation of the two-plate anchors according to the single-plate anchor system (N) was described as $N = F_{double} / F_{single}$.

In Figure 6, the N values increase when the spacing ratio (s/D) increases in a non-linear form. According to the graph, the maximum performance in a two-plate anchor system was obtained as 20 times, compared with the single-plate case, for the lowest embedment depth ratio, $H/D=1$ (Figure 6.a). As described earlier, the optimum spacing ratio was obtained as $3.5D$ for the performance increments. The graph of the performance variation against the embedment depth ratio was given in Figure 6.b for the specific spacing ratio of $3.5D$.

From the graph it can be concluded that, the N values decrease when the embedment ratio increases significantly until $H/D=4$, but it is more or less constant for the values of $H/D > 4$.

4 STATISTICAL ANALYSIS

For predicting the performance of the systems, empirical estimation methods are generally used in civil-engineering applications, including geotechnical engineering (Rao and Prasad [33], Niroumand and Kassim [34]). Regression analysis is one of the most commonly used empirical methods to examine the relationship between a dependent variable and a set of independent variables. Correlation and regression analysis are related in the sense that both deal with the relationships among variables. Neither regression nor correlation analyses can be interpreted as establishing cause and effect relationships. The correlation coefficient (R) measures only the degree of linear association between two variables and also the coefficient of determination (R^2) is used as a measure of the quality of the regression. The method that is used in this study is preferred as a similarity model and can be adopted for pullout capacities of double-plate anchor systems because the independent variables used are explicit and the dimensionless variables are physically bounded (Misir and Laman [35]).

The formulation was derived from 84 numerical analysis results with different embedment and spacing ratios. The developed formulation contains the dimensionless parameters of the embedment ratio (H/D) with a range of 1 to 7 and a spacing ratio (s/D) with a range of 0.5 to 7 for a double-plate anchor. After the studies in the literature were examined, it was decided that the curve type controlling of the plate stress ratio is a function of the exponential behavior, as seen in Eq. 2.

$$y = a * e^{b/x} \quad (2)$$

$$\frac{\sigma_{yy \text{ bottom}}}{\sigma_{yy \text{ single}}} = \left(-7.11 + \left(0.98 * \frac{H}{D} \right) + \frac{127.19}{\left(\frac{H}{D} \right)^2} \right) * e^{\left(\frac{0.424 * \frac{H}{D} - 5.4}{s/D} \right)} \quad (3)$$

Regression analysis is a technique used to estimate values that are unknown using known values. It is important to know the shape and the degree of the functional relationship between the variables. The value of the correlation coefficient indicates the degree of reliability for the estimated values (Misir and Laman [35]). The comparison of the vertical stresses on the bottom plate of the two-plate anchors and the single-plate anchor $\sigma_{yy \text{ bottom}}/\sigma_{yy \text{ single}}$ in dimensionless form obtained from PLAXIS and the formulation results is shown in Figure 7. The relationship between the PLAXIS and the formulation (Eq. 3) results are very comparable, with the line of $y=x$ having a high coefficient of determination equal to 0.995 (Figure 7).

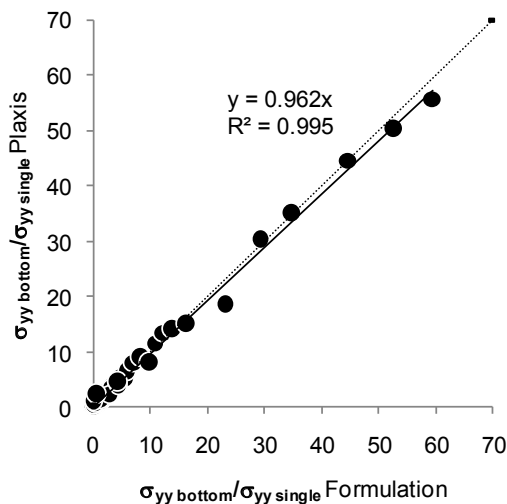


Figure 7. Correlation of the predicted results from the formulation data and PLAXIS.

5 RESULTS AND DISCUSSION

5.1 Analytical Determination of the Uplift Capacity

There have been numerous theoretical studies that address the uplift capacity of a single horizontal anchor. The majority of these studies, however, assume a condition of plane strain for the case of a continuous strip anchor or axi-symmetric for the case of circular anchors. In recent years the failure mechanisms and the pullout capacities of multi-plate anchor systems have been investigated and current approaches are now being developed. The most common approach is to categorize the multi-plate anchor system according to their failure mechanisms. For this purpose, the pullout capacities of the multiple anchor systems can be calculated based on the failure mechanisms in two groups as individual bearing or cylindrical shear. The important point in this approach is that the designer should know the critical embedded ratio and the spacing ratios to distinguish the behavior of the failure between the shallow and deep anchors.

However, in this study the double-plate anchor system and failure mechanisms have not been categorized as either a shallow or deep individual bearing versus cylindrical shear. All of the models that have been analyzed comprise a combination of both the deep and shallow anchor systems. Unlike the general approaches in the literature, in this study the pullout capacity was calculated from the vertical stress variation over the plate surface during the vertical movement caused by the pulling force. A similar semi-empirical approach was used by Meyerhof and Adams [3] to include the circular anchors by extending the strip anchor results by modifying the passive earth pressures with a shape factor.

To obtain the pullout capacity, the maximum vertical stresses corresponding to the defined vertical displacement over the plates were collected and the effective stresses at the plate depth levels were subtracted from this value (Eq. 4)

$$F = \left[\left(\sigma_{yy \text{ bottom}} + \sigma_{yy \text{ upper}} \right) * A_{pl} \right] - \left[\gamma * D * A_{pl} * \left(2 \frac{H}{D} + \frac{s}{D} \right) \right] \quad (4)$$

5.2 Comparison of the PLAXIS results with those obtained from Eq. (4)

The pullout capacities can be obtained from the conventional formulation given in Eq. (4) with the known vertical stresses, from the upper (single-plate analysis results from PLAXIS 2D) and the lower plate (statistical approach). The graph in Figure 8 shows the comparison

of the uplift capacities obtained from the PLAXIS 2D analysis and the developed approach that are given in Equation 4 for the double-plate anchor system. The linear 1:1 line was also plotted in this figure in order to discuss the performance of the statistical models. It can be seen from the figure that by using Eq. (4) the location points of the numerical and the predicted pullout capacity values are scattered around the 1:1 line with a high coefficient of determination equal to 0.982.

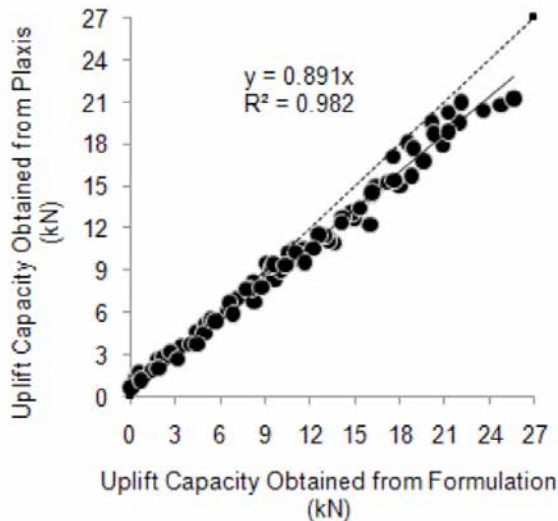


Figure 8. Comparison of the uplift capacities obtained from PLAXIS and formulation (Eq. 4).

As seen from Table 3, the pullout capacities between the results of the numerical analysis and the proposed approach were obtained in a close fit. The variables in Table 3 include the embedment ratio H/D and the anchor spacing ratio s/D . The comparisons between the numerical and proposed methods were given as the rate of the pullout capacities ($F_{Developed}/F_{Plaxis}$). For the majority of cases, the calculated capacities are approximately within +3% of the measured values, which is adequate for design purposes as an average. As seen in Table 3, the developed $F_{Developed}/F_{Plaxis}$ parameters, especially for $H/D=1, 2$ and $s/D=0.5, 1.0, 1.5$, are well below the prescribed limit value of 1. Especially for these six values, the difference is caused from the exponential part of the formulation for the shallow embedded depths and the close spacing ratios.

In summary, the implementation steps of the proposed approach are as follows:

1. The single-plate anchor model is generated at the desired embedment ratio (H/D) in the numerical analysis. But the most important thing is that the

H/D value must be the same with the upper plate depth in the two-plate anchor model.

2. The single-plate model should be analyzed at a 5% vertical displacement ratio with PLAXIS 2D.
3. The maximum vertical stress value on the circular plate can be obtained from this analysis.
4. This vertical stress value corresponds to the upper plate in the case of two plates because of the same effective stress and the same vertical movement.
5. The stress value on the bottom plate can be calculated from the statistical formulation as given in Eq. (3) by using the embedded and spacing ratios.
6. After the two last steps, the vertical stresses are the known parameters to obtain the pullout resistance for the desired vertical displacement.
7. Finally, the uplift capacity of the two-plate anchor system can be calculated using Eq. (4).

Limitations

The results reported in the present study are only valid for the embedment and spacing ratios referred to herein. The breakout factors and the failure mechanisms and also the size and scale effects of the plate anchors have not been investigated. Therefore, the results obtained from this study should not be used in practice without a verification based on experimental studies.

6 CONCLUSIONS

On the basis of the analysis of the results obtained from the present investigation, the following main conclusions can be drawn:

- The aim of the single-plate anchor modelling was to understand the effect of the embedment depth of the anchor. The results of this group of analyses were used as a reference analysis to make a transition to the two-plate anchor model. The breakout factors' variation of the single-plate anchor according to the versus embedment ratios from 1 to 7 (H/D) at a constant 30° angle of the shearing resistance of sandy soil were in good agreement with the literature.
- The vertical stress distribution at a predetermined vertical displacement (1 cm) on the upper plate was obtained as similar to the single-plate anchor model at a constant embedment ratio. Also, the maximum vertical stress on the upper plate increased with the increment of the embedment ratios, but it was independent of the spacing ratios (s/D) for a 1cm movement of the anchor system.
- In the two-plate anchoring case, the maximum

Table 3. Comparison of the results of the Plaxis analysis and the developed formulation.

H/D	s/D	F (kN) Developed	F (kN) Plaxis	$F_{Developed}/$ F_{Plaxis}	H/D	s/D	F (kN) Developed	F (kN) Plaxis	$F_{Developed}/$ F_{Plaxis}
7	0.5	9.063	9.494	0.95	3	0.5	1.880	2.626	0.72
7	1	10.990	10.462	1.05	3	1	2.233	2.771	0.81
7	1.5	13.651	10.914	1.25	3	1.5	3.401	3.575	0.95
7	2	16.041	12.277	1.31	3	2	4.965	4.518	1.10
7	2.5	18.006	15.023	1.20	3	2.5	6.573	6.076	1.08
7	3	19.598	16.776	1.17	3	3	8.076	7.615	1.06
7	3.5	20.895	17.838	1.17	3	3.5	9.428	9.243	1.02
7	4	21.962	19.528	1.12	3	4	10.626	10.304	1.03
7	5	23.597	20.370	1.16	3	5	12.611	11.517	1.09
7	6	24.775	20.735	1.19	3	6	14.159	12.390	1.14
7	7	25.651	21.237	1.21	3	7	15.381	13.459	1.14
6	0.5	8.229	8.149	1.01	2	0.5	0.421	1.257	0.33
6	1	9.371	8.677	1.08	2	1	0.617	1.766	0.35
6	1.5	11.338	9.764	1.16	2	1.5	1.464	1.828	0.80
6	2	13.290	11.247	1.18	2	2	2.719	3.154	0.86
6	2.5	14.987	12.686	1.18	2	2.5	4.084	3.707	1.10
6	3	16.411	15.011	1.09	2	3	5.406	5.473	0.99
6	3.5	17.600	17.103	1.03	2	3.5	6.624	6.648	1.00
6	4	18.595	18.083	1.03	2	4	7.722	7.622	1.01
6	5	20.149	19.528	1.03	2	5	9.578	9.431	1.02
6	6	21.288	20.251	1.05	2	6	11.050	10.267	1.08
6	7	22.147	20.954	1.06	2	7	12.227	10.568	1.16
5	0.5	7.125	7.025	1.01	1	0.5	0.057	0.415	0.14
5	1	7.933	7.678	1.03	1	1	0.063	0.622	0.10
5	1.5	9.657	8.363	1.15	1	1.5	0.750	1.131	0.66
5	2	11.547	10.122	1.14	1	2	1.880	1.960	0.96
5	2.5	13.286	11.014	1.21	1	2.5	3.179	2.645	1.20
5	3	14.799	13.107	1.13	1	3	4.483	3.682	1.22
5	3.5	16.093	14.382	1.12	1	3.5	5.715	5.334	1.07
5	4	17.199	15.293	1.12	1	4	6.846	5.862	1.17
5	5	18.960	17.668	1.07	1	5	8.795	7.779	1.13
5	6	20.280	18.730	1.08	1	6	10.372	9.337	1.11
5	7	21.292	18.856	1.13	1	7	11.651	9.550	1.22
4	0.5	4.463	4.574	0.98					
4	1	5.024	5.133	0.98					
4	1.5	6.505	6.063	1.07					
4	2	8.300	6.729	1.23					
4	2.5	10.046	8.972	1.12					
4	3	11.620	10.487	1.11					
4	3.5	13.002	11.448	1.14					
4	4	14.204	12.717	1.12					
4	5	16.158	14.527	1.11					
4	6	17.654	15.400	1.15					
4	7	18.818	15.714	1.20					

- vertical stress distribution on the bottom plate was in a trend of increasing, depending on the increasing spacing ratio.
- The vertical stress on the bottom plate remained unchanged at the larger spacing ratios from $3.5D$. At the smaller values from $3.5D$, the vertical stresses increased with the spacing ratios. Therefore, the maximum performance of the bottom plate was obtained at a spacing ratio of 3.5.
 - When the performance increment on the two-plate anchor system was plotted on the graph for the optimum $3.5D$ plate spacing, the effect of the second plate increased the system performance to 20 times for the embedment depth of $H/D=1$. This increase was continued in a trend of decreasing up to $H/D=4$ and resulted in an average 2.3 times increase in the system performance with values of greater than $H/D=4$.
 - Based on the analysis, the vertical stresses on the lower plate were formulated using a statistical analysis based on dimensionless parameters such as the H/D and s/D ratios. When compared with the values obtained from this formula and the values obtained from PLAXIS, the vertical stress value on the lower plate was estimated with a high correlation coefficient of 0.995.
 - When a proportional relationship between PLAXIS and the developed approach is established, the $F_{y\text{ developed}} / F_{y\text{ plaxis}}$ ratio, which should be 1 in the ideal solution, was obtained in average as 1.03 for all the analyses.
 - It can be concluded that, the perspective of the developed approach is quite promising for the prediction of the ultimate pullout capacity of two-plate anchor system as a preliminary design work.

REFERENCES

- [1] Mitsch, M.P., Clemence, S.P. 1985. The uplift capacity of helix anchors in sand. In Uplift Behaviour of Anchor Foundations in Soil. Proceedings of a Session Sponsored by the Geotechnical Engineering Division of the American Society of Civil Engineers, Michigan. American Society of Civil Engineers, New York, pp. 26–47.
- [2] Ghaly, A., Hanna, A., Hanna, M. 1991. Uplift behavior of screw anchors in sand, II: Hydrostatic and Flow Conditions. J. Geotech. Eng. Div. ASCE 117, 5, 794–808. [https://doi.org/10.1061/\(ASCE\)0733-9410\(1991\)117:5\(794\)](https://doi.org/10.1061/(ASCE)0733-9410(1991)117:5(794))
- [3] Meyerhof, G.G., Adams, J.I. 1968. The ultimate uplift capacity of foundations. Canadian Geotechnical Journal 5, 4, 224–244. <https://doi.org/10.1139/t68-024>
- [4] Das, B.M. 1978. Model tests for uplift capacity of foundations in clay. Soils and Foundations 18, 2, 17–24. https://doi.org/10.3208/sandf1972.18.2_17
- [5] Das, B.M. 1980. A procedure for estimation of ultimate uplift capacity of foundations in clay. Soils and Foundations 20, 1, 77–82. <https://doi.org/10.3208/sandf1972.20.77>
- [6] Ilamparuthi, K., Dickin, E.A., Muthukrisnaiah, K. 2002. Experimental investigation of the uplift behavior of circular plate anchors embedded in sand. Canadian Geotechnical Journal 39, 3, 648–664. <https://doi.org/10.1139/t02-005>
- [7] Dickin, E.A., Laman, M. 2007. Uplift response of strip anchors in cohesionless soil. Advances in Eng. Software 38, 8-9, 618–625. <https://doi.org/10.1016/j.advengsoft.2006.08.041>
- [8] Rowe, R. K., Davis, E.H. 1982. The behavior of anchor plates in sand. Geotechnique 32, 1, 25–41. <https://doi.org/10.1680/geot.1982.32.1.25>
- [9] Bildik, S., Laman, M. 2011. Experimental investigations on uplift behavior of plate anchors in cohesionless soil. Journal of Fac. Eng. Archit. Gazi 26, 2, 486–497.
- [10] Zhang, N., Wu, H.N., Shen, J.S., Hino, T., Yin, Z.Y. 2017. Evaluation of the uplift behavior of plate anchor in structured marine clay. Marine Georesources & Geotechnology 35, 6, 758–768. <https://doi.org/10.1080/1064119X.2016.1240273>
- [11] Tang, C., Phoon, K.K. 2016. Model uncertainty of cylindrical shear method for calculating the uplift capacity of helical anchors in clay. Engineering Geology 207, 14–23. <https://doi.org/10.1016/j.enggeo.2016.04.009>
- [12] Demir, A., Ok, B. 2015. Uplift response of multi-plate helical anchors in cohesive soil. Geomechanics and Engineering 8(4), 615–630. <http://dx.doi.org/10.12989/gae.2015.8.4.615>
- [13] Nazir, R., Chuan, H.S., Niroumand, H., Kassim, K.A. 2014. Performance of single vertical helical anchor embedded in dry sand. Measurement 49, 42–51. <https://doi.org/10.1016/j.measurement.2013.11.031>
- [14] Mittal, S., Mukherjee, S. 2013. Vertical uplift capacity of a group of helical screw anchors in sand. Indian Geotechnical Journal 43(3), 238–250. <https://doi.org/10.1007/s40098-013-0055-5>
- [15] Mokhbi, H., Mellas, M., Mabrouki, A., Pereira, J.M. 2018. Three-dimensional numerical and analytical study of horizontal group of square anchor plates in sand. Acta Geotechnica 13(1), 159–174. <https://doi.org/10.1007/s11440-017-0557-x>
- [16] Papadopoulou, K., Saroglou, H., Papadopoulos,

- U. 2014. Finite element analyses and experimental investigation of helical micropiles. *Geotechnical Geological Engineering* 32(4), 949-963. <https://doi.org/10.1007/s10706-014-9771-6>
- [17] Schiavon, J.A., Tsuha, C.H.C., Thorel, L. 2016. Scale effect in centrifuge tests of helical anchors in sand. *International Journal of Physical Modelling in Geotechnics* 16(4), 185-196. <https://doi.org/10.1680/jphmg.15.00047>
- [18] Tsuha, C.H., Aoki, N., Rault, G., Thorel, L., Garnier, J. 2012. Evaluation of the efficiencies of helical anchor plates in sand by centrifuge model tests. *Canadian Geotechnical Journal*, 49(9), 1102-1114. <https://doi.org/10.1139/t2012-064>
- [19] Hanna, A., Ayadat, T., Sabry, M. 2007. Pullout resistance of single vertical shallow helical and plate anchors in sand. *Geotech. Geolog. Engineering* 25, 559-573. <https://doi.org/10.1007/s10706-007-9129-4>
- [20] Ghaly, A.M., Hanna, A.M., Hanna, M. 1991. Uplift behavior of screw anchors in sand I: Dry sand. *Journal of Geotech. Eng. ASCE* 117(5), 773-793. [https://doi.org/10.1061/\(ASCE\)0733-9410\(1991\)117:5\(773\)](https://doi.org/10.1061/(ASCE)0733-9410(1991)117:5(773))
- [21] Merifield, R.S. 2011. Ultimate uplift capacity of multiplate helical type anchors in clay. *Journal of Geotechnical and Geoenvironmental Engineering ASCE*, 137(7), 704-716. [https://doi.org/10.1061/\(ASCE\)GT.1943-5606.0000478](https://doi.org/10.1061/(ASCE)GT.1943-5606.0000478)
- [22] Narasimha Rao, S., Prasad, Y.V.S.N., Shetty, M.D. 1991. The behavior of model screw piles in cohesive soils. *Soils and Foundations* 31(2), 35-50. https://doi.org/10.3208/sandf1972.31.2_35
- [23] Narasimha Rao, S., Prasad, Y.V.S.N., Veeresh, C. 1993. Behavior of embedded model screw anchors in soft clays. *Géotechnique*, 43(4), 605-614. <https://doi.org/10.1680/geot.1993.43.4.605>
- [24] Merifield, R.S., Smith, C.C. 2010. The ultimate uplift capacity of multi-plate strip anchors in undrained clay. *Computers and Geotechnics* 37(4), 504-514. <https://doi.org/10.1016/j.compgeo.2010.02.004>
- [25] Brinkgreve, R.B.J., Vermeer, P.A. 1998. Finite element code for soil and rock analyses. A.A. Balkema, Rotterdam, Netherlands.
- [26] Laman, M., Yildiz, A. 2007. Numerical studies of ring foundations on geogrid-reinforced sand. *Geosynthetics International*, 14(2), 52-64. <https://doi.org/10.1680/gein.2007.14.2.52>
- [27] Sakr, M. 2009. Performance of helical piles in oil sand. *Canadian Geotechnical Journal*, 46(9), 1046-1061. <https://doi.org/10.1139/T09-044>
- [28] Elsherbiny, Z.H., El Naggar, H.M. 2013. Axial compressive capacity of helical piles from field tests and numerical study. *Canadian Geotechnical Journal*, 50(12), 1191-1203. <https://doi.org/10.1139/cgj-2012-0487>
- [29] Sakr, M. 2011. Installation and performance characteristics of high capacity helical piles in cohesionless soils. *DFI Journal - The J. of the Deep Foundations Institute* 5(1), 39-57. <https://doi.org/10.1179/dfi.2011.004>
- [30] Merifield, R.S., Lyamin, A.V., Sloan, S.W. 2006. Three-dimensional lower-bound solutions for the stability of plate anchors in sand. *Geotechnique*, 56(2), 123-132. <https://doi.org/10.1680/geot.2006.56.2.123>
- [31] Sarac, D.Z. 1989. Uplift capacity of shallow buried anchor slabs. *Proceedings, 12th International Conference on Soil Mechanics and Foundation Engineering, Rio de Janeiro*, 12, 2, 1213-1218.
- [32] Koutsabeloulis, N.C., Griffiths, D.V. 1989. Numerical modelling of the trap door problem. *Geotechnique*, 39(1), 77-89. <https://doi.org/10.1680/geot.1989.39.1.77>
- [33] Rao, S.N., Parasad, Y.V.S.N. 1993. Estimation of uplift capacity of helical anchors in clays. *Journal of Geotechnical Engineering ASCE, Technical Note* 119(2), 352-357. [https://doi.org/10.1061/\(ASCE\)0733-9410\(1993\)119:2\(352\)](https://doi.org/10.1061/(ASCE)0733-9410(1993)119:2(352))
- [34] Niroumand, H., Kassim, K.A. 2014. Uplift response of symmetrical anchor plates in reinforced cohesionless soil. *Arabian Journal of Geosciences* 7(9), 3755-3766. <https://doi.org/10.1007/s12517-013-1071-6>
- [35] Misir, G., Laman, M. 2017. A modern approach to estimate the bearing capacity of layered soil. *Periodica Polytechnica Civil Engineering* 61(3), 434-446. <https://doi.org/10.3311/PPci.9578>

CONSOLIDATION ANALYSIS OF CLAYEY SOILS USING ANALYTICAL TOOLS

ANALIZA KONSOLIDACIJE GLINASTIH TAL S POMOČJO ANALITIČNIH ORODIJ

Bartłomiej Szczepan Olek

Tadeusz Kościuszko University of Technology,
Warszawska 24, 31-155 Kraków, Poland
E-mail: bartlomolek@gmail.com

DOI <https://doi.org/10.18690/actageotechslov.15.2.58-73.2018>

Keywords

consolidation; clay; filtration; coefficient of consolidation; optimization

Ključne besede

konsolidacija; glina; filtracija; koeficient konsolidacije; optimizacija

Abstract

The uncoupled Terzaghi consolidation equation (excess pore pressure only) is widely used to predict the rate and magnitude of settlements in clayey soils. The theoretical solution is based on the approach of considering the soil permeability and compressibility as one parameter obtained by experimental methods – the coefficient of consolidation c_v . This article presents two analytical tools that allow us to determine the consolidation coefficient, which is independent of a single measurement point and represents the consolidation behavior for the significant progress of settlements. The presented methods were based on the process of optimizing the coefficient of consolidation value and the quasi-constant approach, which assumes the identification of a quasi-filtration consolidation phase using the $\log c_v - U$ relationship. To assess the validity of each method, the experimental results were compared to the theoretical solution and quantified using a new statistical parameter d_n .

Izvleček

Nevezana Terzaghija enačba vertikalne konsolidacije (upoštevane samo porne nadtlake) se pogosto uporablja za napovedovanje hitrosti in velikosti pomikov v glinastih tleh. Teoretična rešitev temelji na pristopu upoštevanja prepustnosti tal in stisljivosti v enem parametru, pridobljenem z eksperimentalnimi metodami – koeficient vertikalne konsolidacijske c_v . V članku sta prikazani analitični orodji, ki omogočata določitev koeficienta vertikalne konsolidacije, ki je neodvisen od posamezne merilne točke in opisuje konsolidacijsko vedenje za značilen časovni razvoj posedkov. Predstavljene metode temeljijo na procesu optimizacije vrednosti koeficienta vertikalne konsolidacijske in kvazi - konstantnega pristopa, ki predpostavlja identifikacijo faze kvazifiltracijske konsolidacije z uporabo relacije $\log c_v - U$. Veljavnost obeh metod smo ocenili s primerjavo eksperimentalnih rezultatov in teoretičnih rešitev ter kvantitativno ovrednoteli z uporabo novega statističnega parametra d_n .

1 INTRODUCTION

Studying the properties of geomaterials is one of the basic aspects involved in predicting the soil-structure interaction and planning any soil-strengthening modifications. Geomaterials include all the natural, processed or produced and improved materials used in geotechnical applications. Natural geomaterials are mainly soils and rocks, as well as mixed material behaving as a transient between soil and rock. Natural soils, especially soft clays, muds and expansive soils, can be problematic and may cause a potential threat to a construction. During the design of foundations and embankments on clayey soil, it is crucial to predict the magnitude and rate of settlements. The accuracy of predictions in the design stage depends on the input value of the coefficient of consolidation c_v . A correct assessment of the real values of this parameter and the impact of the factors influencing it is a difficult problem. It has been a serious challenge for researchers and has not yet been fully resolved.

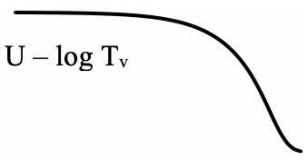
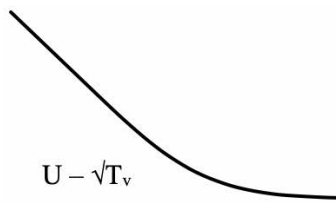
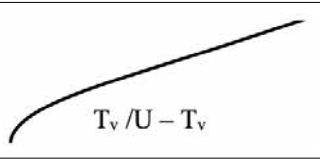
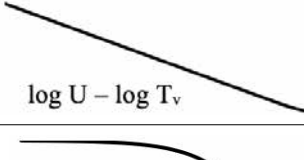
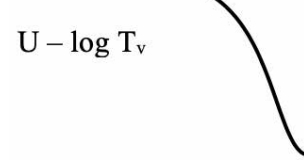
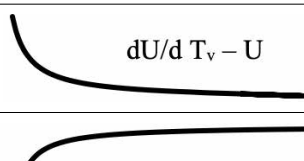
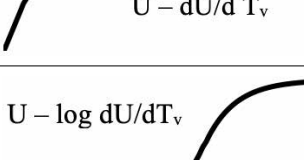
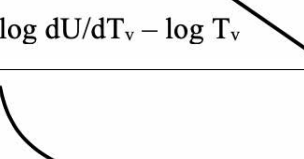
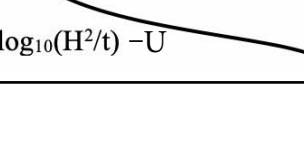
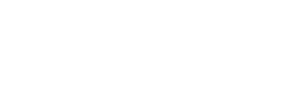
The consolidation process is a combination of two phenomena: permeability, which controls the rate at which water is removed from the pore space (and thus the rate of the settlement at any time) and compressibility, which controls the evolution of the distribution of excess pore-water pressure (and thus the duration of the consolidation process). The widely used Terzaghi theory is based on a linear stress-strain relationship and constant permeability. Theoretical solutions were based on a consideration of all the soil properties as one parameter – the coefficient of consolidation c_v , obtained with experimental methods ([1]). Over the past 50 years, difficult and time-consuming attempts have been made to develop appropriate methodologies and interpretations of consolidation tests. The valuable material refers to the studies on the standardization of time-compression data analysis and can be found in ([2], [3], [4], [5], [6], [7], [8], [9], [10], [11], [12]). The achievements of the above-mentioned researchers relate to the commonly accepted Terzaghi theory and could be used for a uniform, initial, pore-pressure distribution. Solutions for a non-uniform and sinusoidal initial pore-pressure distribution can be found in Lovisa et al. [13] and Lovisa and Sivakugan [14], respectively. The existing methods for calculating the consolidation coefficient were collected in Table 1, where the experimental and theoretical relations considered during the analysis were included as well as the individual expressions for the coefficient of consolidation.

The realistic application of Terzaghi's theory for determining the consolidation coefficient assumes the identification of a primary consolidation range. This recognition can be conducted by the fitting procedure of the theoretical relationship between different variations of the degree of consolidation and the dimensionless time factor $U - T_v$ to the measured deformation with time or the pore-water pressure dissipation. This kind of procedure is carried out on the basis of the similarity between the observed and theoretical curves, which can be presented and interpreted in various ways. Consolidation coefficients determined on the basis of fitting procedures are characterized by a large dispersion, which results from choosing different reference points on the experimental curve and a different way of determining the start and the end of the primary consolidation. Cohesive soils are variable due to the nature of their formation (genesis) and the impact of environmental processes. Recognizing the coefficient of consolidation as a constant parameter is the main disadvantage of Terzaghi's conventional theory. It is known that the consolidation properties of the soil should be treated in an independent manner, and considering them as one coefficient makes it difficult to relate the experimental course of the process with the theoretical solution.

The main goal of the work was to develop a reliable interpretation tool for consolidation studies based on the optimization procedure. Special attention was paid to the secondary consolidation effect on the filtration nature of the process and on the relative duration of the quasi-filtration consolidation phase.

During the analysis, three basic assumptions resulting from Terzaghi's theory were examined: (i) the quasi-constant consolidation coefficient; (ii) the convergence between the theoretical and the experimental course of the consolidation curves; and (iii) parallelism in the course of the curves of the pore-pressure dissipation and deformation. This paper examines those aspects based on an analysis of the consolidation data with settlement and pore-water pressure measurements during the consolidation using a Barden-Rowe hydraulic consolidometer. Tests conducted on various soils with different liquid and plastic limits have been evaluated and the coefficient of consolidation has been determined. Two methods for computing the coefficient of consolidation were presented in the study.

Table 1. Comparison of existing methods for determining the coefficient of consolidation.

Method	Experimental relation	Expression	Form of the theoretical curve	Reference
Metoda $\log t$	$\delta - \log t$	$c_v = \frac{0,196H^2}{t_{50}}$	$U - \log T_v$ 	Casagrande & Fadum [15]
Metoda \sqrt{t}	$\delta - \sqrt{t}$	$c_v = \frac{0,848H^2}{t_{90}}$		Taylor [16]
Slope method	$\delta - \sqrt{t}$	$c_v = \frac{\pi}{4} \left(\frac{m_1}{\delta_{EOP}} \right)^2 H^2$	$U - \sqrt{T_v}$ 	Al-Zoubi ([17], [18])
Rectangular hyperbola method	$t/\delta - t$	$c_v = 0.24 \frac{M}{c} H^2$	$T_v / U - T_v$ 	Sridharan et al. [4]
Logarithmic method	$\log \delta - \log t$	$c_v = \frac{(\pi / 4)H^2}{t_{88.3}}$	$\log U - \log T_v$ 	Sridharan & Prakash [6]
Inflection point method	$\delta - \log t$	$c_v = \frac{0.405H^2}{t_{70}}$	$U - \log T_v$ 	Mesri & Feng [19]
Early stage method	$\delta - \log t$	$c_v = \frac{0.0385H^2}{t_{22.14}}$	$U - \log T_v$ 	Robinson & Allam [20]
SRS method	$d\delta/dt - \delta$	$c_v = \frac{m_1 H^2}{2,468}$	$dU/d T_v - U$ 	Al-Zoubi [21]
$\delta - d\delta/dt$ method	$\delta - d\delta/dt$	$c_v = -\frac{4H^2}{\pi^2 m_2}$	$U - dU/d T_v$ 	Tewatia et al. [10]
$\delta - \log d\delta/dt$ method	$\delta - \log d\delta/dt$	$c_v = -\frac{0.2566v_{16.19}H^2}{s_{50}}$	$U - \log dU/dT_v$ 	Tewatia et al. [10]
Velocity method / Improved velocity	$\log d\delta/dt - \log t$	$c_v = \frac{0.793H^2}{t_{88.5}}$	$\log dU/dT_v - \log T_v$ 	Parkin [22] Pandian et al. [23]
One point method	$\log_{10}(H^2/t) - U$	$c_v = \frac{T_i H^2}{t_i}$	$\log_{10}(H^2/t) - U$ 	Sridharan et al. [24]

2 PRINCIPLES OF TERZAGHI'S CONSOLIDATION THEORY

The one-dimensional differential equation that governs the consolidation and pore-water-pressure dissipation process is expressed as follows:

$$\frac{\partial u}{\partial t} = c_v \frac{\partial^2 u}{\partial z^2} \quad (1)$$

where t is the time variable, u is the pore-water pressure, and z is the depth below the top of the soil layer.

By introducing the dimensionless variables:

$$Z = \frac{z}{H} \quad (2)$$

and

$$T_v = \frac{c_v t}{H^2} \quad (3)$$

equation (1) is as follows:

$$\frac{\partial u}{\partial T_v} = c_v \frac{\partial^2 u}{\partial Z^2} \quad (4)$$

The dimensionless time factor T_v defined by equation (3) is related to the average degree of consolidation U , which determines the progress of the process. The solution to equation (4) for the initial uniform excess pore-water pressure inside the soil layer is given by:

$$U = 1 - \sum_{m=0}^{m=\infty} \frac{2}{M^2} e^{-M^2 T_v} \quad (5)$$

The theoretical velocity of consolidation $U=dU/dt$ is a product of the differentiation of the relationship between U and T_v with respect to T_v . Depending on the degree of consolidation, the following approximations can be used:

$$\dot{U} = \frac{1}{\sqrt{\pi T_v}} \quad \text{for } T_v \approx 0.197 (U \leq 50\%) \quad (6)$$

$$\dot{U} = 2e^{-(\pi^2 T_v / 4)} \quad \text{for } T_v > 0.197 (U > 50\%) \quad (7)$$

3 COURSE OF CONSOLIDATION

Considering one-dimensional strain, volume changes are caused by the initial or immediate compression, the primary consolidation, and the secondary (rheological) consolidation. It should be noted that rheological conditions depend on the soil skeleton's susceptibility to plastic deformations. The progress of the consolidation process is assessed on the basis of pore-pressure dissipation or the relative settlement of the consolidated layer (Fig. 1).

The initial compression occurs almost immediately after the load application due to the expulsion and compression of air in the voids. Primary consolidation is a time-dependent deformation caused by the excess of pore water pressure. Tewatia et al. [21] separated three phases of this deformation using the relationship between the compression and the compression rate. The first primary phase is characterized by the smallest impact of secondary consolidation effects and the calculated values of the coefficient of consolidation are the highest. After that the transition from first primary to second primary phase occurs. The second primary phase in many soils is characterized by a constant coefficient of consolidation value for a considerable percentage of the total settlement. Olek and Woźniak [22] separated this phase using the criterion of a quasi-constant value of the coefficient of consolidation and the relationship between the degree of consolidation and the coefficient of consolidation. As the

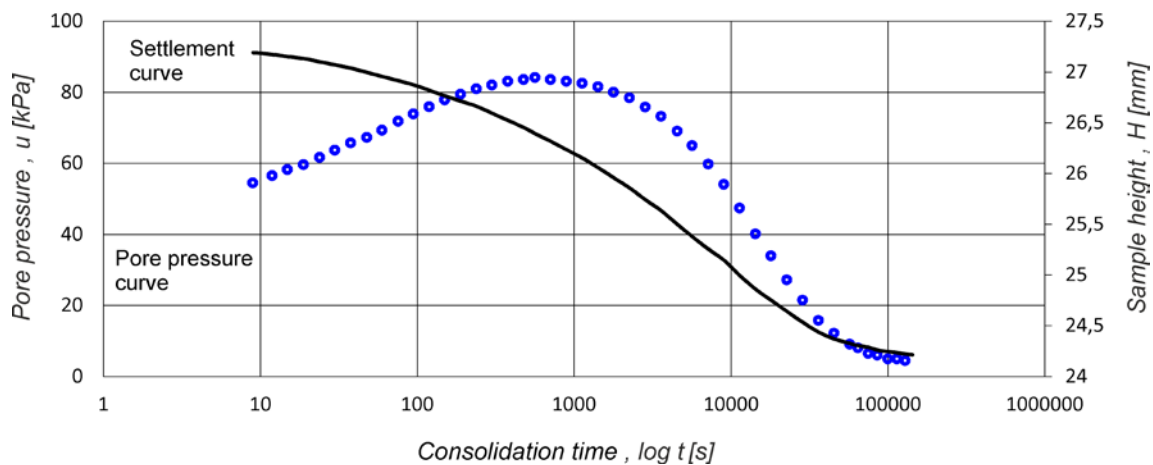


Figure 1. Typical experimental course of consolidation for clayey soil.

consolidation progresses, the impact of the soil's secondary consolidation increases. The transient behaviour is characterized by obtaining different temporary values of cv . The deformations in this phase result from both the pore pressure dissipation and the elasto-plastic nature of the soil skeleton's compression. The last phase is a pure creep, time-dependent deformation under a virtually constant effective stress. It should be noted that not all the phases are observed in all the soils.

The pore pressure dissipation curve is characteristic. In research practice, the mobilization delay characterized by an increase in the pore pressure is usually observed. Dobak and Pająk [23] indicated some soil properties (particle size distribution, nature of micro-pore connections, content of minerals prone to swelling) that determine the delay of the load transfer on the liquid phase. The character of the pore pressure increases and reaches its stabilized maximum value $u_{b,max}$. As the pore pressure is mobilized, the larger but not fully developed influence of the limited permeability of soil causes a delay in the deformation. It can also be seen that the volume of the soil is temporarily reduced after loading due to compression or releasing gases from the sample.

The courses of the uniaxial strains and the pore-pressure dissipation do not usually overlap. Regarding the theoretical assumptions, changes in the voids ratio e are not proportional to the changes in the effective stress, and the compressibility and permeability parameters for a relatively high stress applied, decrease during the consolidation process. The explanation of the above can be made on the basis of three definitions of the degree of consolidation, referring to excess pore water pressure, changes in the effective stress and changes in the strain. Comparing them with each other, some irregularities can be encountered. Terzaghi's theory assumes that the change in the effective stress is almost linearly dependent on the deformation or change in the voids ratio. However, this is not correct, because this change is proportional to the change in the logarithm of the effective stress. During the consolidation process, the thickness of the loaded soil layer decreases due to the decrease in the voids ratio. The corresponding settlement of the layer at any time is expressed as a percentage of the total settlement and is called the average degree of consolidation U_{avg} . The average degree of consolidation can be expressed as follows:

$$U_{avg} = 1 - \frac{\int_{z=0}^{z=2H} u dz}{2H \times u_0} = \frac{\int_{z=0}^{z=2H} (\Delta\sigma' - u) dz}{2H \times \Delta\sigma'} \quad (8)$$

where H refers to the layer thickness, u_0 is the initial excess pore water pressure caused by the load applica-

tion. The consolidation process can be considered as completed when the total excess pore water pressure is dispersed due to the load increase. However, because of the absence of a linear relationship between the changes in the pore pressure and the voids ratio, the average degree of consolidation over time calculated on the basis of the pore water pressure measurements U_{avg}^u is not equal to the average degree of consolidation determined on the basis of the registration of settlements U_{avg}^e . This can be expressed as follows:

$$U_{avg}^u \neq U_{avg}^e \quad (9)$$

and

$$1 - \frac{\int_0^{2H} u dz}{2H \times (\Delta\sigma')} \neq 1 - \frac{\int_0^{2H} \varepsilon_t dz}{\int_0^{2H} \varepsilon_{t=\infty} dz} \quad (10)$$

4 RELIABILITY OF THE CONSOLIDATION ANALYSIS

In this section the two methods for determining the coefficient of consolidation are briefly described together with preliminary studies of the usefulness of the considered solutions.

4.1 Optimisation method for the coefficient of consolidation and the convergence criteria

Using Terzaghi's model to describe the consolidation process has certain consequences. The course of the consolidation caused by the flow of water through the soil is determined by a set of curves. A fixed value of the consolidation coefficient is assigned to each curve. The compatibility between the experimental data and the theoretical solution can be the criterion for compliance with Terzaghi's model. In this study, the theoretical characteristics of the consolidation progress with the smallest possible discrepancy were assessed using the statistical parameter d_n :

$$d_n = \frac{\sum \frac{|U_{n,i} - U_{n,i}^*|}{U_{n,i}} \times w_{n,i}}{\sum w_{n,i}} \quad (11)$$

$$w_{n,i} = \frac{U_{n,i}^* - U_{n,i-1}^*}{2} + \frac{U_{n,i+1}^* - U_{n,i}^*}{2} \quad (12)$$

where $U_{n,i}$ is an experimental consolidation degree, $U_{n,i}^*$ is a consolidation degree calculated for a theoretical solution on the basis of the modified dimensionless time factor T_v^{mod} and $w_{n,i}$ is a range around each theoretical point $U_{n,i}^*$ characterizing the dispersion. In Figure 2 a graphical presentation of this approach is shown, where the dashed line refers to the experimental course and the

continuous line to the theoretical one. The best-fitted model curve with the corresponding consolidation coefficient is the one for which the d_n parameter is the smallest. The use of a particular type of weighted average allowed us to determine accurately the representation of individual measurements under changing axial deformation or the speed of the pore water pressure dissipation conditions, taking into consideration the real environment of each point. A similar comparison of the consolidation was conducted by Mikasa and Takada [24] based on the curve-rule method, Lovisa, Sivakugan & Read [25] using the variance method and Sebai & Belkacemi [26] using a probabilistic method and a minimization of the sum of the squared residual (SSR). In the second and third approaches, the authors applied ranges of probable values for d_0 , d_{100} and c_v .

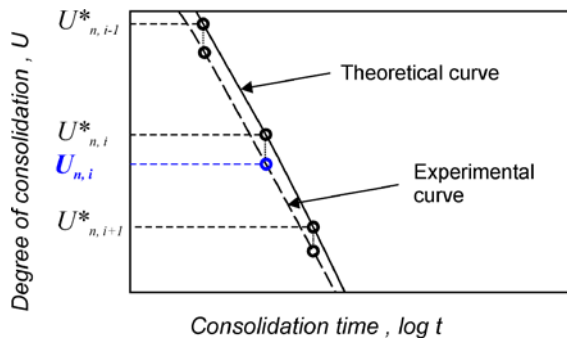


Figure 2. Graphical illustration for the estimation of the dispersion between the theoretical and experimental consolidation progress.

4.2 Quasi-constant c_v method

For the initial, uniform distribution of excess pore water pressure u_0 and double drainage, the average degree of consolidation can be recorded as:

$$U_{avg} = 1 - \frac{\int_0^H u_e dz}{u_i} = 1 - \sum_{m=0}^{\infty} \frac{2}{M^2} \exp^{-M^2 T_v} \quad (13)$$

where u_i is the initial excess pore pressure distribution as a result of an applied load, u_e is an excess pore water pressure at any time during the consolidation process, $M = (\pi/2)(2m+1)$ and m is an integer. The experimental data obtained from the test can be converted into a dimensionless time factor T_v using the following expression:

$$T_v = \frac{c_v t}{H^2} \quad (14)$$

Most graphical methods based on the curve-fitting procedure assume obtaining a consolidation factor for one selected point. In the case of the $\log(t)$ method of

Casagrande and Fadum [11] the point refers to 50% of the consolidation progress. In Taylor's $t^{1/2}$ method [12], this point corresponds to 90% of the consolidation progress. The remaining extensions of the above methods mainly concern the choice of a different reference point ([15], [16], [27], [28]). Through the functional dependence $c_v - U$ plotted on a semi-logarithmic chart, the variability of the coefficient of consolidation can be examined in relation to the entire experimental course of consolidation. Using the quasi-determination criterion, such a consolidation phase can be determined, where constant or quasi-constant values of the consolidation coefficient for a significant part of the deformation course are observed. The values of the consolidation coefficient for individual reference points are calculated on the basis of two solutions for the dependence $T_v - U$, assuming a parameter T_v for a rectangular or parabolic distribution of the pore-water pressure, using the following formula:

$$c_{v,i} = \frac{T_{v,i} H_i^2}{t_i} \quad (15)$$

where $c_{v,i}$ is the coefficient of consolidation for the considered time t_i , and H_i refers to the height of the sample at the analysed time t_i .

The parametric rectangular distribution is based on the solution of the rectangular distribution of the excess pore water pressure in the axis of the sample. In this case, the degree of consolidation was determined on the basis of the uniaxial deformation of the sample. The parabolic distribution was based on the values obtained from the solution of the series, where the consolidation coefficient was determined on the basis of the distribution of the pore water pressure. Distinguishing from the entire course of the consolidation process, the duration of the quasi-filtration consolidation phase can be performed by analyzing the variability of the relation $c_v - U$. Based on many results of consolidation studies in the course of the consolidation described by the function $c_v - U$, three ranges with a different nature of changes in the consolidation coefficient can be identified. In Figure 3a an example of a characteristic course of the semi-logarithmic relation $c_v - U$ was shown. The variability in the initial phase of consolidation is determined by the moment of applying a load to the sample of saturated soil (in terms of deformations, this is the initial compression). At this stage, the consolidation coefficient demonstrates the highest values. Then the values of the consolidation coefficient decrease together with the increase in the consolidation degree U and stabilize to a quasi-linear character (slight fluctuations in the course of the $f = c_v - U$ function are observed in this phase). Before the stabilization is recorded, there is a bound which is noted both for the course of the pore pressure

dissipation and for the uniaxial strain. Stabilized values can be defined as quasi-constant values of the consolidation factor $c_{v,i}^q$. The stabilization confirms that the assumptions (i) and (ii) are fulfilled, and the limit value $c_{v,i}^q$ determines the end of the quasi-filtration phase, e.g., U_{EOP} . At a later stage, the consolidation coefficient value is characterized by lower values, depending on the size of the impact of the rheological mechanisms. If the limit values $c_{v,i}^q$ for the interval are known, the geometric mean of these values can be calculated as follows:

$$\prod c_v^q = \sqrt[n]{a_1 \cdot a_2 \cdot \dots \cdot a_n} \quad (16)$$

where a_1, a_2, a_n are the following values of the consolidation coefficient from the set of n values for the quasi-filtration phase. The value of the consolidation coefficient calculated this way is independent of a single measurement point and represents the consolidation behaviour for a significant settlement progress.

For example, a sample of a natural clay from Krakowiec with an initial height of 24.3 mm was consolidated at a

load of 400 kPa. In the first step of the analysis, a quasi-linear part of the $\log c_v - U$ plot was identified and the average value of the quasi-filtration coefficient of the consolidation was calculated according to the formula (16). In order to check the compatibility of the theoretical solution, a curve was constructed and compared to the curve obtained from the test (Fig. 3b). Using the optimization method, the lowest value of the d_n parameter was determined, together with the corresponding coefficient of consolidation value (Fig. 3c).

These values were used to determine the compliance between the best model solution and the quasi-constant approach. The best-fitting model curve was obtained using the coefficient of consolidation $c_v = 2.60 \times 10^{-8} \text{ m}^2/\text{s}$, with the conformity assessed using the parameter $d_n = 0.000889$. The average value of the quasi-filtration consolidation ratio was $c_v^q = 2.59 \times 10^{-8} \text{ m}^2/\text{s}$ and the d_n parameter was 0.000893. Note that the values of the d_n parameter ranged from 0.0009 to 0.0001, indicating a very good “fit” between the measured and the theoretical data. As the results show, both approaches are in very good agreement.

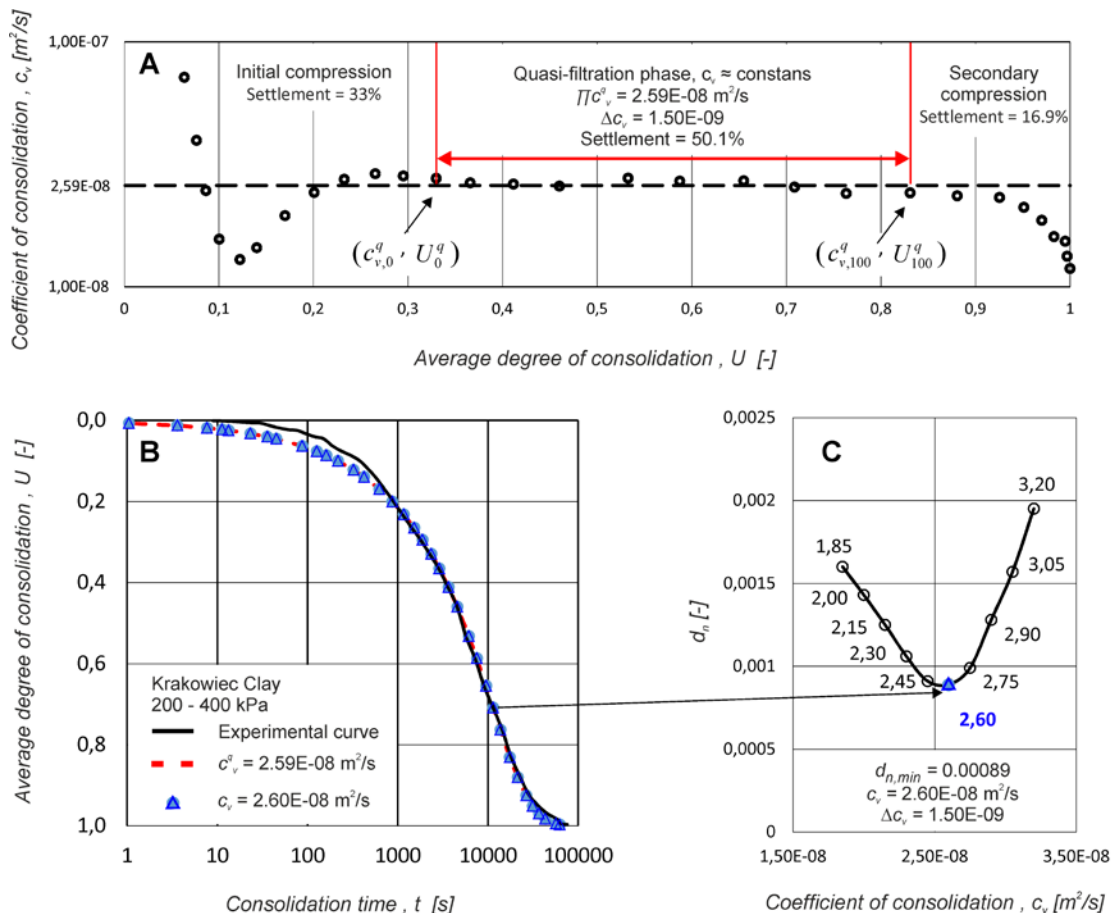


Figure 3. Experimental results showing the variation of the coefficient of consolidation with the degree of consolidation referring to the optimization procedure: A – coefficient of consolidation versus degree of consolidation, B – comparison of the experimental data and theoretical best-fit solution; C – relationship between d_n parameter and coefficient of consolidation c_v .

5 SOILS AND TESTING PROCEDURES

To illustrate the importance of assessing the validity of the optimization method and the quasi-constant approach and to determine the consolidation parameters, an extensive testing programme was established. In this study the behaviour of the reconstituted clay as well as the behaviour of clay-sand mixture and the natural organic mud soil were the focus of interest. Three soils, namely, Krakowiec clay (designated as C), 50 % clay – 50 % sand mixture (designated as S), and organic silty clay as per ISO Soil Classification (PN-EN ISO 14688-2), [29] were used for the study. Washed fine river sand was used for the mixture (passing a 0.2 mm sieve and retained on a 0.063 sieve). The physical properties of these soils are listed in Table. 1. The clay suspension was made of Krakowiec clay from a deposit near the village of Chmielów, in the Podkarpackie voivodeship, Poland. Based on a chemical analysis for aluminosilicate refractory products and raw materials in accordance with ISO 12677-2: 2007, [30], which was an alternative method to the X-ray fluorescence (XRF), the chemical composition

of the clay used in this study was determined. Table 3 shows the tested chemical compounds. Additionally, a qualitative phase analysis was carried out using the X-ray diffraction method and quartz, calcite, dolomite, albite, siderite, illite, muscovite, kaolinite and microcline were found.

After drying the Krakowiec clay at a temperature of 106 degrees, it was separated into lumps and wiped through a sieve with a sieve diameter of 0.0063 with the use of distilled water. The suspension was left for one week until the clay fraction sedimented. Then, the clarified water was removed from the surface, and the clay fraction was dried. The pastes with plasticity approaching the liquid limit ($w_n \approx LL$) were made from dried and mortar-ground soil mass combined with distilled water to form a uniform texture. The first four IL-type tests with the measurements of the pore-water pressure were made according to the following path of load increments: 50, 100, 200, 400 kPa. The fifth and sixth studies were carried out for a different path of load increment: 25, 50, 75, 100, 125 kPa. The pore pressure was measured centrally on the lower surface of the specimen along the

Table 2. Physical parameters of soils utilized in the present study.

Soil	Particle size			Atterberg limits		Plasticity index	Organic matter	Specific gravity
	Sand [%]	Silt [%]	Clay [%]	Liquid limit [%]	Plastic limit [%]	I_p [%]	OM [%]	G_s [-]
Krakowiec clay	14	48	38	65.02	24.60	40.42	-	2.72
Organic silty clay	2	56	42	109.78	54.22	55.56	11.33	2.62

Table 3. Chemical composition of Krakowiec Clay.

	Chemical compound							
	SiO ₂	Al ₂ O ₃	Fe ₂ O ₃	CaO	MgO	K ₂ O	Na ₂ O	TiO ₂
% content	10.31	59.34	14.17	5.39	5.40	2.13	2.47	0.79

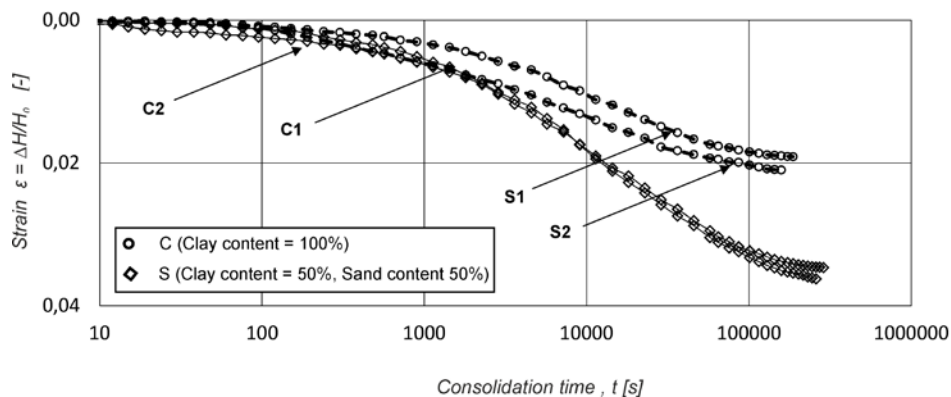


Figure 4. Strain-time relationships for samples with different clay contents.

impermeable base of the cell. The consolidation cell used a fixed-type ring setup with single drainage on the top end of the specimen. The paste samples were prepared in a consolidation ring with a diameter of 75 mm and a height of 30 mm. The strain-time curves obtained in the studies for the first four tests are shown in Figure 4.

In general, a similar compression behaviour was found for the two types of samples. Samples with sand content revealed greater stiffness compared to the clay samples, which is reflected in the smaller recorded settlement. It is interesting to note that despite the preparation of a homogeneous clay paste with the addition of sand, the same curves were not obtained. The biggest differences were visible in the advanced stage of consolidation, where for sample S1 the deformations proceeded slightly more slowly than for sample S2.

6 VALIDATION ANALYSIS

In this section the previously developed solutions were applied to the interpretation of the consolidation tests. Then the results of the analyses were discussed, and the importance of optimisation was highlighted with an example. The comparison of the two classic curve-fitting methods for the coefficient of consolidation with those developed in this study were also presented.

6.1 Interpretation of the consolidation test

Based on the $U - T_v$ relationship for the initial constant, positive pore-water pressure, Sridharan et al. [20] noted that it was possible to generate theoretical curves $\log_{10}(H^2/t_{theor}) - U$. This approach assumes applying

the experimental data on one graph, represented by measuring coordinates relative to the model curves $\log_{10}(H^2/t_{theor}) - U$, plotted on the basis of known values of the consolidation coefficient and the corresponding theoretical time. The consolidation coefficients used to construct the theoretical curves $\log_{10}(H^2/t_{theor}) - U$ were obtained on the basis of the procedure described in Section 3. The combination of the experimental curves $\log_{10}(H^2/t_{exp}) - U$ versus the background of the model curves $\log_{10}(H^2/t_{theor}) - U$, allows a direct comparison of the obtained values of the consolidation factor (Fig 5).

The quasi-filtration phase was established on the basis of the $\log c_v - U$ relationship. Two interpretation assumptions were made when interpreting the results of the research. The first one assumes the criterion of convergence of the uniaxial strains and the pore-pressure dissipation. The second assumes a coincidence between the experimental data and the corresponding theoretical solution. In the case of a paste made of clay without any admixture of sand, the consolidation behaviours do vary. Despite a similar course of uniaxial deformation curves, the filtration nature of the consolidation process was ambiguous. For sample C1, there was a clear delay in the pore pressure dissipation. The consolidation factor calculated on the basis of the pore pressure dissipation was significantly lower than that determined on the basis of the deformation. In turn, for sample C2, the opposite behaviour was observed: the excess pore water pressure dissipation proceeded faster than the deformation. It should be noted that we are dealing here with two different factors that drive the consolidation process. One can be described as filtration and the other as a rheological factor. A qualitative assessment of the dominance of one factor over another can be performed using the param-

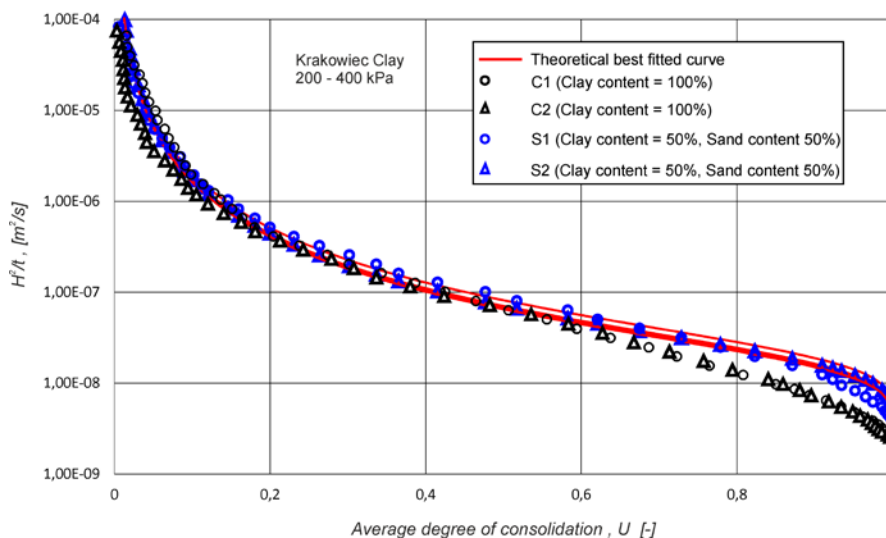


Figure 5. Family of the $\log_{10}(H^2/t_{exp}) - U$ curves collocated with the $\log_{10}(H^2/t_{theor}) - U$ curves.

eter η developed by Dobak and Gaszyński [31]. This parameter is determined using two values of the coefficient of consolidation calculated on the basis of excess pore water pressure dissipation and strain in accordance with the formula:

$$\eta = \frac{c_{v,\varepsilon} - c_{v,u}}{c_{v,u}} \quad (17)$$

where $c_{v,\varepsilon}$, $c_{v,u}$ are consolidation coefficients calculated on the basis of deformation and pore water pressure dissipation, respectively.

On the basis of the $U - t$ diagrams and the d_n parameter, the range of consolidation was determined and expressed as a percentage of the quasi-filtration phase in relation to the entire process, for which the compliance of the applied theoretical model with respect to the obtained experimental data was the largest. Figures 6a and 6b show the consolidation behaviour for the reconstituted clay paste. For samples C1 and C2, the percentage of

compliance was 37% and 34%, respectively. The 3% difference was based on the greater extent of the initial compression after applying the load for sample C2. However, the effect of the initial compression caused a very slight deviation in relation to the theoretical solution. Both samples showed very similar susceptibility to the rheological effects, with the visible part of the secondary consolidation, which starts close to $U = 55\%$. The adopted scheme for the implementation of the experiments assumed the possibility of extending the relative scope of the quasi-filtration consolidation through the application of a sand fraction. The results of the tests carried out on samples of sand and clay pastes showed that the content of the sand fraction caused a significant reduction in the differentiation between the courses of the pore pressure dissipation and the uniaxial strain curves (Fig. 6c). On the basis of the presented graphs, a very slight predominance of settlement progress was observed in comparison to the dissipation excess

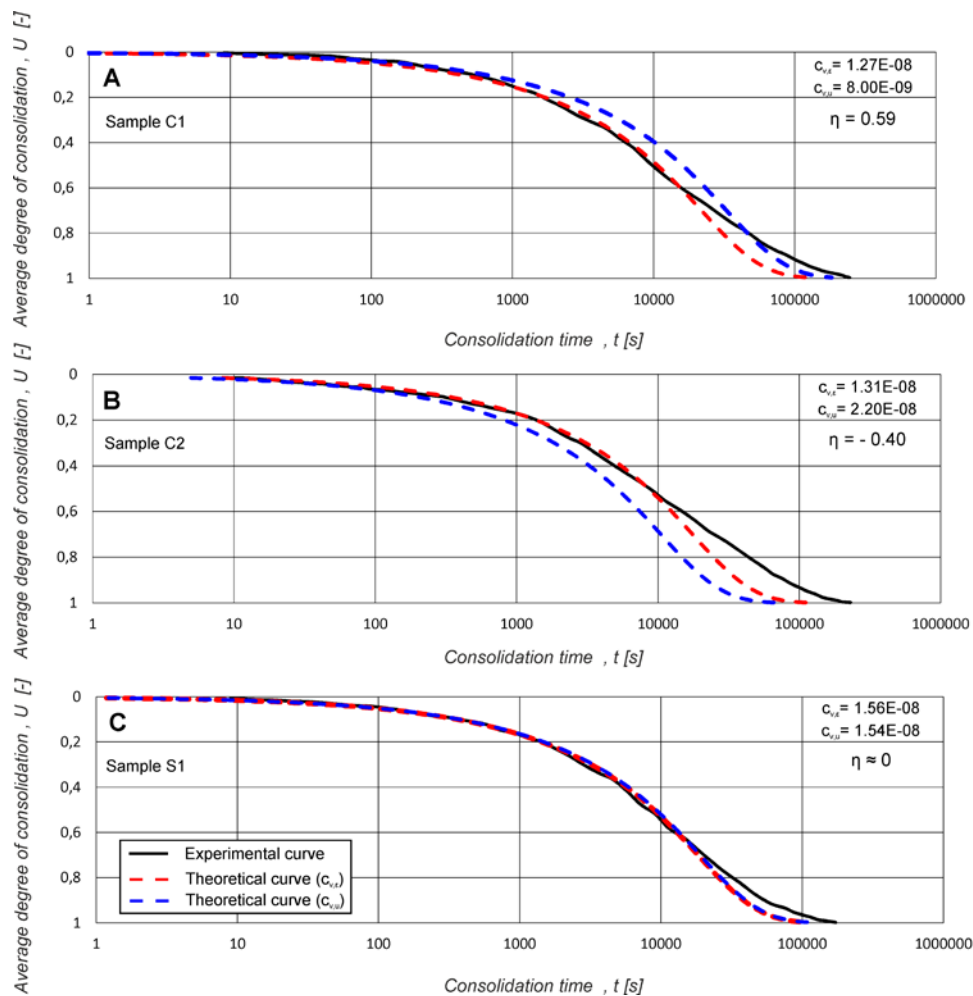


Figure 6. Consolidation behaviour of reconstituted clay paste with and without additional sand content: A) predominance of the rheological factor over the filtration factor; B) predominance of the filtration factor over the rheological factor; and C) similar course of consolidation in terms of filtration and creep factors.

pore water pressure. The assumed presence of the sand fraction influenced the extension of the quasi-filtration phase and the reduction of the secondary consolidation phase, which can be seen in the $U - t$, $\log_{10}(H^2/t) - U$ and $\log c_v - U$ diagrams. The range of the separated phase is in the highest compliance with the theoretical model in the case of the S1 and S2 samples, i.e., 70% and 69%,

Table 3. Results of consolidation parameters' interpretation obtained with the Quasi- constant, Optimisation and Casagrande methods.

Sample	Strain $q-c$	c_v [m ² /s]		Course parameters		
		Pore pressure $q-c$	Optimisation	Log t	η	$d_{n,min}$
S1	1.56 ⁻⁰⁸	1.54 ⁻⁰⁸	1.56 ⁻⁰⁸	1.82 ⁻⁰⁸	0.033	0.0032
S2	1.60 ⁻⁰⁸	1.49 ⁻⁰⁸	1.61 ⁻⁰⁸	1.85 ⁻⁰⁸	0.073	0.0030
C1	1.27 ⁻⁰⁸	8.00 ⁻⁰⁹	1.28 ⁻⁰⁸	1.46 ⁻⁰⁸	0.59	0.0038
C2	1.31 ⁻⁰⁸	2.20 ⁻⁰⁸	1.31 ⁻⁰⁸	1.36 ⁻⁰⁸	-0.40	0.0034

respectively. Table 3 presents the consolidation parameters obtained from the current analysis.

6.2 Comparison of the Optimisation, Quasi-constant, Taylor, and Casagrande methods in terms of c_v and d_n

The selected experimental consolidation courses together with the best-fitting model curve obtained for a reconstituted clay (study no 5) and for an organic soil (study no. 6) are shown in Figures 7 and 8, respectively. For each of the load increments the experimental $U - T_v$ data was plotted against the theoretical curve from which the d_n parameter was calculated. Both example sets of $U - T_v$ curves demonstrate the high quality of the fit associated with the d_n parameter, irrespective of the physical properties of the tested soils. It can be observed that the secondary consolidation essentially starts around $U = 60\%$ for the clay samples and $U = 40-60\%$ for the organic soil samples. It indicates that the inves-

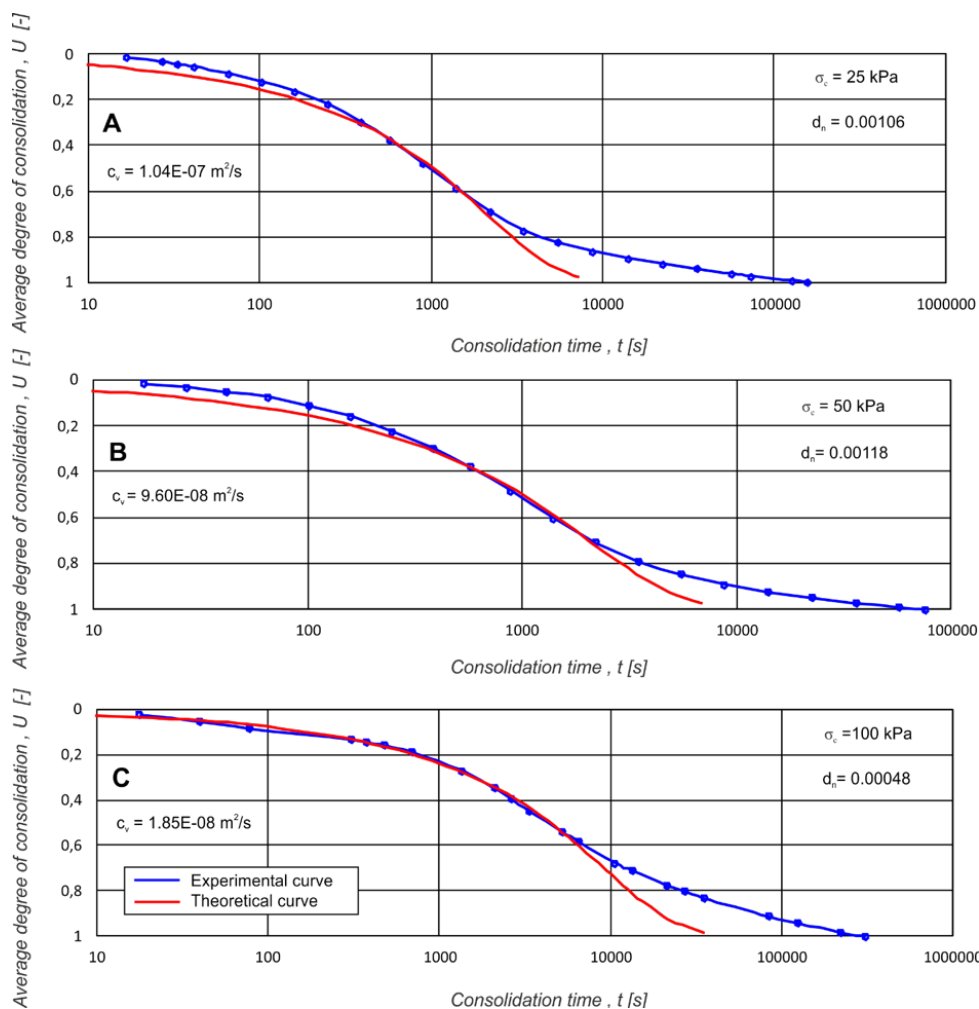


Figure 7. Experimental consolidation courses versus the best-fitting model curves for reconstituted clay.

tigated organic soil is prone to significant secondary deformations. It was found by the optimization method that Terzaghi's consolidation model is able to capture a slight range of the total deformation. This is mainly due to the postulation that the consolidation process is regarded as purely filtration [32]. Figs 7–8 show that the greater is the discrepancy between the experimental and theoretical curves, the greater is the presence of secondary consolidation.

The coefficient of consolidation for the clay sample computed using Eq. (6) and (7) and those obtained using the Taylor ($t^{1/2}$) and Casagrande ($\log t$) methods with reference to the d_n parameter are shown in Figure 9. The optimal c_v value of each curve was determined based on the lowest value of the d_n parameter. This value represented the best agreement between the experimental and theoretical curves. The results of the analysis for clay and organic soil in Tables 4–5 showed that the accuracy of the determined c_v with the quasi-constant method in

relation to the best analytical solution increases together with the rise of the consolidation load. The c_v^q values were slightly higher than those determined on the basis of the optimization. However, the largest discrepancies were observed for loads of 25 and 50 kPa.

Nevertheless, both methods are characterized by good compliance and the c_v values correspond with each other. Using the optimization method, the value of c_v changed, which refers to the distance from the theoretical curves imposed on the experimental curve, which should be chosen very carefully. In turn, in the quasi-constant method, a very precise distinction of the quasi-filtration phase for which the value of c_v will be calculated is crucial. Making mistakes at this stage of the analysis could result either in an inadequate shape of the $d_n - c_v$ curve as well as in a lack of assumed linearity of part of the $c_v - U$ curve. The lowest values of the d_n parameter were obtained for the optimization method and the quasi-constant method. The highest values were

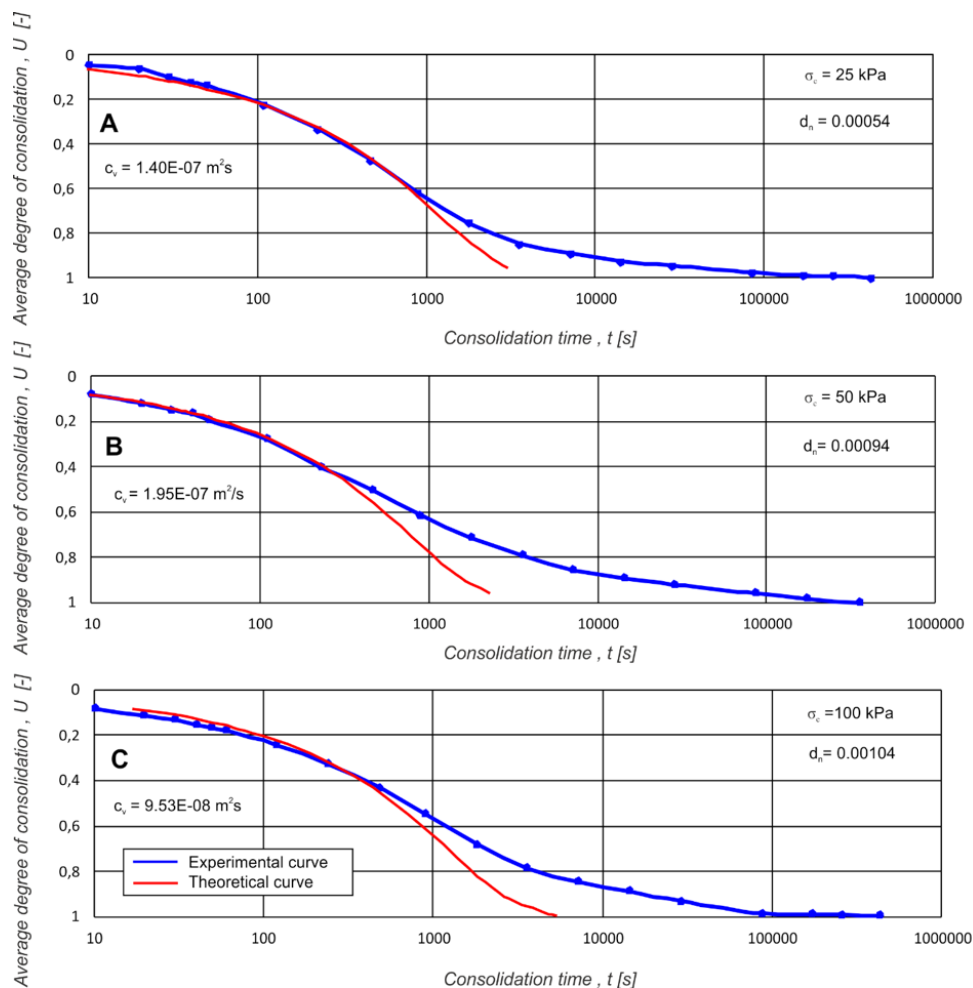


Figure 8. Experimental consolidation courses versus the best-fitting model curves for organic soil.

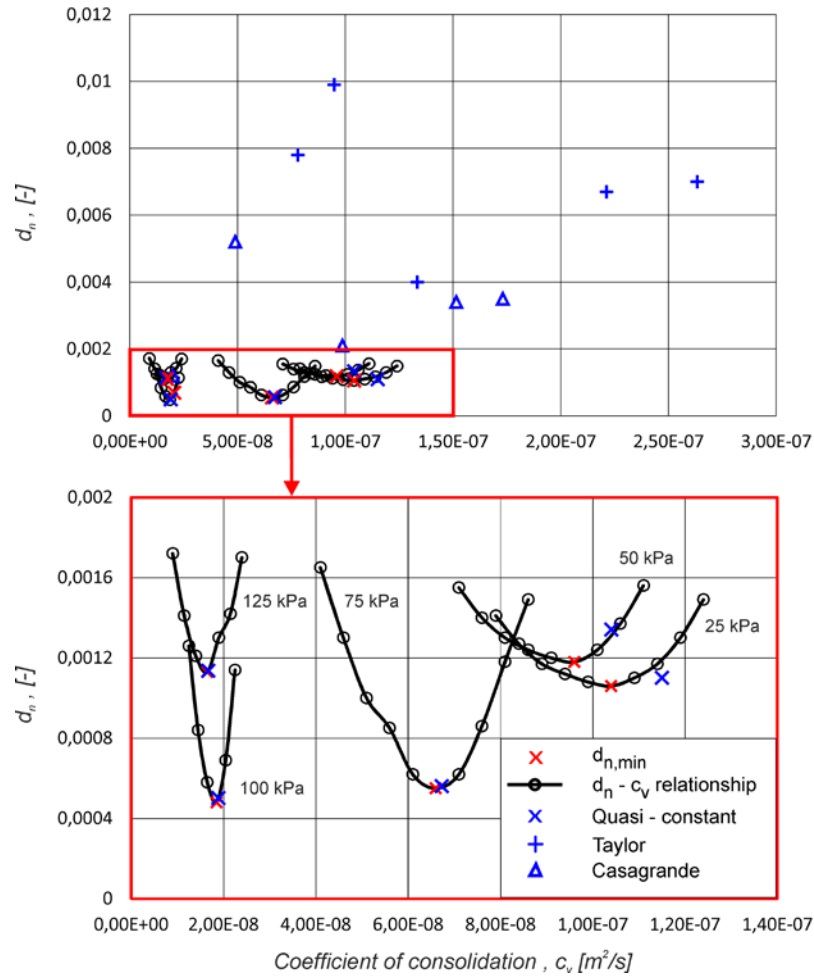


Figure 9. Coefficient of consolidation for all increments by various methods with reference to the changes of the d_n parameter. The optimal values of the coefficient of consolidation related to the lowest d_n parameter are marked with red crosses.

Table 4. Consolidation parameters for the reconstituted clay obtained from the interpretation of the consolidation tests using the quasi-constant approach, the optimization method, the $\log(t)$ method the and $t^{1/2}$ method.

Load		Quasi-constant Method	Optimization Method	$\log(t)$ Method	$t^{1/2}$ Method
25	$c_v \times 10^{-8} \text{ m}^2/\text{s}$	11.5	10.4	17.3	26.3
	$d_{n,min}$	0.0011	0.0010	0.0035	0.0070
	$U_{EOP} \%$	69.1	69.3	-	-
50	$c_v \times 10^{-8} \text{ m}^2/\text{s}$	10.4	9.60	15.1	22.1
	$d_{n,min}$	0.0013	0.0011	0.0034	0.0067
	$U_{EOP} \%$	70.7	72.1	-	-
75	$c_v \times 10^{-8} \text{ m}^2/\text{s}$	6.73	6.60	9.86	13.3
	$d_{n,min}$	0.0005	0.0005	0.0021	0.0040
	$U_{EOP} \%$	61.0	62.0	-	-
100	$c_v \times 10^{-8} \text{ m}^2/\text{s}$	1.89	1.85	4.88	9.47
	$d_{n,min}$	0.0005	0.0004	0.0052	0.0099
	$U_{EOP} \%$	58.0	59.8	-	-
125	$c_v \times 10^{-8} \text{ m}^2/\text{s}$	1.67	1.65	2.0	7.8
	$d_{n,min}$	0.0011	0.0011	0.0012	0.0078
	$U_{EOP} \%$	51.0	51.0	-	-

Table 5. Consolidation parameters for the organic soil obtained from an interpretation of the consolidation tests using the quasi-constant approach, the optimization method, the $\log(t)$ method and the $t^{1/2}$ method.

Load		Quasi-constant Method	Optimization Method	$\log(t)$ Method	$t^{1/2}$ Method
25	$c_v \times 10^{-8} \text{ m}^2/\text{s}$	11.39	11.40	11.60	8.40
	$d_{n,min}$	0.0011	0.00054	0.0035	0.0070
	$U_{EOP} \%$	61.0	61.0	-	-
50	$c_v \times 10^{-8} \text{ m}^2/\text{s}$	18.90	19.50	24.00	17.00
	$d_{n,min}$	0.0013	0.00093	0.0034	0.0067
	$U_{EOP} \%$	70.7	40.0	-	-
75	$c_v \times 10^{-8} \text{ m}^2/\text{s}$	6.73	13.00	15.50	10.50
	$d_{n,min}$	0.0005	0.0005	0.0021	0.0040
	$U_{EOP} \%$	61.0	62.0	-	-
100	$c_v \times 10^{-8} \text{ m}^2/\text{s}$	9.66	9.53	9.89	8.00
	$d_{n,min}$	0.0005	0.0010	0.0052	0.0099
	$U_{EOP} \%$	58.0	43.0	-	-
125	$c_v \times 10^{-8} \text{ m}^2/\text{s}$	8.48	9.50	9.21	7.50
	$d_{n,min}$	0.0011	0.0011	0.0012	0.0078
	$U_{EOP} \%$	51.0	51.0	-	-

obtained with the $t^{1/2}$ method, indicating a significant discrepancy between the laboratory measurements and the theoretical fitting. For individual load levels, the conformity of the calculated c_v for the three methods was obtained only in one case. For the load of 125 kPa on the basis of the optimization method, the quasi-constant and $\log(t)$ methods, the $d_{n,min}$ values were calculated as 0.0011, 0.0011 and 0.0012, respectively. Similar results were obtained in the case of the organic soil.

The c_v values of the reconstituted clay obtained using the $\log t$ method and the $t^{1/2}$ method were significantly higher than those determined on the basis of the optimization and the quasi-constant approaches. The differences between those two methods and the optimisation method are discussed using the obtained ratios of the c_v values. This method is often adopted in geotechnical practice and was used, among others, in the works of Sridharan and Prakash [6], Robinson [8], Al - Zoubi [17] and Cortellazzo [33]. The first and second ratios compare the c_v values determined using $\log t$ and $t^{1/2}$ methods with those determined using the optimisation method. The c_v values determined using the $\log t$ and $t^{1/2}$ methods were approximately 1.5 to 2.7 and 2 to 5 times higher than those obtained with the optimization method, respectively. The third relation compared the $\log t$ and $t^{1/2}$ methods and was calculated as from 1.5 to 4. This regularity is confirmed by previous analyses carried out for various clay soils by Sridharan et al. [20], Feng and Lee [27], Chan [34] and Shukla et al. [35]. In the case of the organic soil the c_v values obtained using the $\log t$ method

were significantly higher and using the $t^{1/2}$ method were significantly lower than those determined on the basis of the optimization and the quasi-constant approaches. The c_v values determined using the $\log t$ method were approximately 1.0 to 1.3 times higher than those obtained from the optimization method. The c_v values determined by the $t^{1/2}$ method were approximately 0.6 to 0.9 times lower than those obtained from the optimization method. The ratio compares the c_v values determined using the $\log t$ method with those determined using the $t^{1/2}$ method, which were always higher than 1.0 and lower than 2.0.

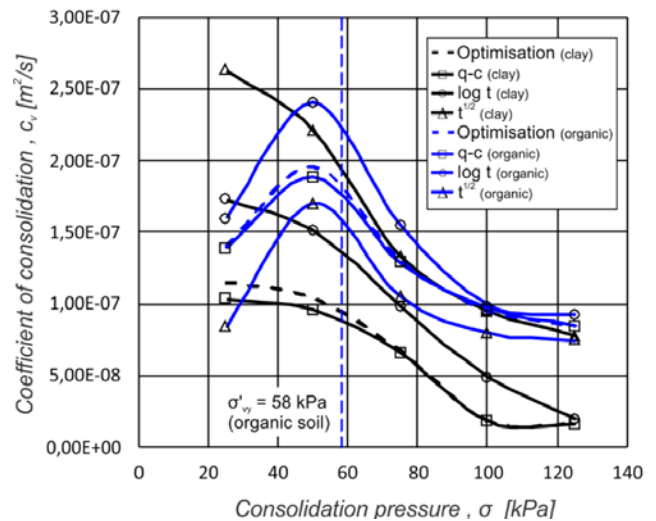
**Figure 10.** Comparison of $c_v - \sigma_c$ curves obtained for different load steps.

Figure 10 illustrates the values of the coefficient of consolidation obtained for different load steps. A downward trend of the c_v - σ'_c relationship was observed in the case of the reconstituted clay for all four methods and was the largest for the $t^{1/2}$ method. The shapes of the calculated c_v - σ curves for the organic soil were generally similar. It is also evident from Fig. 10 that a drastic decrease in the c_v - σ curve appeared near the vertical yield stress σ'_{vy} .

7 CONCLUSIONS

Mathematical modelling, including a comparison of the experimental data with the sets of theoretical solutions, is a promising interpretation approach in consolidation studies. Terzaghi's consolidation theory does not take into account both the initial and secondary effects, hence the c_v values are dependent upon the theoretical solution and refer to the primary consolidation only. Analytical tools made it possible to determine the coefficient of consolidation c_v with the smallest value of the statistical d_n parameter that led to the best fitting of the laboratory data. In this study the d_n parameter was identified as an error function between the experimental and theoretical solutions. The optimization method based on the process of minimizing this function can be implemented in computer spreadsheet programs that are commonly used in various geotechnical applications. Furthermore, the d_n error calculated between the experimental and theoretical degree of consolidation was generally quite low, and always less than the error associated with the $\log t$ and $t^{1/2}$ c_v values. The optimization method was also used to assess the reliability of the results of the quasi-constant method. Using the $\log c_v - U$ relationship, the variability of the coefficient of consolidation in relation to the entire experimental course of consolidation was examined. The analysis of the relationship between the coefficient of consolidation and the degree of consolidation showed the presence of a region with semi-established c_v values.

Based on the results of oedometer tests on various soils, the c_v values estimated by the quasi-constant approach were in good agreement with those obtained from the optimization method. The coefficient of consolidation determined by the graphic methods, e.g., $\log t$ and $t^{1/2}$, is highly variable, due to the assumption of different reference points on the experimental curve. In the case of reconstituted clay the $t^{1/2}$ method gave higher c_v values and higher d_n values than those obtained from both of the presented methods and the $\log t$ method. In the case of the organic soil the $t^{1/2}$ method gave lower c_v values than those obtained from both the presented

methods and the $\log t$ method. In general, the values of c_v calculated using the $\log t$ method were greater than those determined using other methods.

REFERENCES

- [1] Leroueil, S. 1987. Tenth Canadian geotechnical colloquium: recent developments in consolidation of natural clays. *Canadian Geotechnical Journal* 25, 1, 85–107. DOI:10.1139/t88-010
- [2] Šuklje, L. 1957. The analysis of the consolidation process by the isotaches method. *Proceedings of the Fourth ICSMFE, London*, 1, 200–206.
- [3] Parkin, A.K. 1995. Consolidation analysis by the velocity method. *Proceedings of the Compression and Consolidation of Clayey Soils*, Yoshikuni and Kusakabe Eds. A.A. Balkema, Rotterdam, 567–572.
- [4] Sridharan, A., Murthy, N.S., Prakash, K. 1981. Rectangular hyperbola fitting method for one dimensional consolidation. *Géotechnique* 37, 3, 355–368. DOI:10.1680/geot.1987.37.3.355
- [5] Sridharan, A., Prakash, K. 1993. δ - $t\delta$ Method for the determination of coefficient of consolidation. *Geotechnical Testing Journal* 16, 1, 131–134. DOI: 10.1520/GTJ10262J
- [6] Sridharan, A., Prakash, K. 1997. The $\log \delta - \log t$ method for the determination of coefficient of consolidation. *Geotechnical Engineering* 125, 27–32. DOI: 10.1680/igeng.1997.28994
- [7] Tan, T.S., Inoue, T., Lee, S.L. 1991. Hyperbolic method for consolidation analysis. *Journal of Geotechnical Engineering* 117, 11, 1723–1737. DOI:10.1061/(ASCE)0733-9410(1991)117:11(1723)
- [8] Robinson, R.G. 1999. Consolidation analysis with pore water pressure measurements. *Géotechnique* 49, 1, 127–132. DOI:10.1680/geot.1999.49.1.127
- [9] Tewatia, S.K., 1998. Evaluation of true c_v , instantaneous c_v and isolation of secondary consolidation. *Geotechnical Testing Journal* 21, 2, 102–108. DOI: 10.1520/GTJ10748J
- [10] Tewatia, S.K., Sridharan, A., Phalswal, M.K., Singh, M., Rath, S. 2012. Fastest rapid loading methods of vertical and radial consolidations. *International Journal of Geomechanics* 13, 332–339. DOI: 10.1061/(ASCE)GM.1943-5622.0000213
- [11] Barros P.A.L, Pinto P.R.O. 2007. Oedometer consolidation test analysis by nonlinear regression. *Geotechnical Testing Journal* 31, 1, 76–83. DOI: 10.1520/GTJ101007
- [12] Doran I.G., McKinley J.D., Day R.A., Morris P.H. 2006. Determination of the coefficient of consoli-

- ation using a least squares method. *Géotechnique* 56,1, 73-76. DOI:10.1680/geot.2006.56.1.73
- [13] Lovisa, J., Read, W., Sivakugan, N. 2012 - Calculating c_v based on non-uniform initial excess pore pressure. *Geotechnique* 62, 8, 741-748. DOI:10.1680/geot.11.P.055
- [14] Lovisa, J., Sivakugan, N. 2013 - A method to determine c_v under sinusoidal pore pressure distribution. *Geotechnical Testing Journal* 36, 6, 787-798. DOI:10.1520/GTJ20120233
- [15] Casagrande, A., Fadum, R.E. 1940. Notes on soil testing for engineering purposes, Harvard Soil Mechanics 8, Cambridge, Mass.
- [16] Taylor, D.W. 1942. Research on consolidation of clays. *Mass. Inst. of Tech.* 82, 147.
- [17] Al-Zoubi, M.S. 2008. Coefficient of consolidation by the slope method. *Geotechnical Testing Journal* 31, 6, 1-5. DOI: 10.1520/GTJ100810
- [18] Al-Zoubi, M.S. 2014. Consolidation analysis by the modified slope method. *Geotechnical Testing Journal* 37, 3, 1-8. DOI: 10.1520/GTJ20130097
- [19] Mesri, G., Feng, T.W., Shahien, M. 1999. Coefficient of consolidation by inflection point method. *Journal of Geotechnical and Geoenvironmental Engineering* 125, 8, 716-718. DOI: 10.1061/(ASCE)1090-0241(1999)125:8(716)
- [20] Robinson, R.G., Allam, M.M. 1996. Determination of coefficient of consolidation from early stage of log t plot. *Geotechnical Testing Journal* 19, 3, 316-320. DOI: 10.1520/GTJ10358J
- [21] Al-Zoubi, M.S. 2010. Consolidation analysis using the settlement rate-settlement (SRS) method. *Applied Clay Science* 50, 1, 31-40. DOI: 10.1016/j.clay.2010.06.020
- [22] Parkin, A.K. 1987. Coefficient of consolidation by the velocity method. *Géotechnique* 28, 4, 472-474. DOI: 10.1680/geot.1978.28.4.472
- [23] Pandian, N.S., Sridharan, A., Kumar, K.S. 1992. A new method for the determination of coefficient of consolidation. *Geotechnical Testing Journal* 15, 1, 74-79. DOI: 10.1520/GTJ10227J
- [24] Sridharan, A., Prakash, K., Asha, S.R. 1995. Consolidation behavior of soils. *Geotechnical Testing Journal* 18, 1, 58-68. DOI: 10.1520/GTJ10122J
- [21] Tewatia, S.K., Bose, S.K., Sridharan, A., Rath, S. 2007. Stress induced time dependent behavior of clayey soils. *Geotechnical Geological Engineering* 25, 2, 239-255. DOI: 10.1007/s10706-006-9107-2
- [22] Olek, B.S, Woźniak, H. 2017. Determination of quasi-filtration phase of consolidation based on experimental and theoretical course of the uniaxial deformation and distribution of pore pressure. *Geology, Geophysics & Environment* 42, 3, 353-363. DOI:10.7494/geol.2016.42.3.353
- [23] Dobak, P., Pająk, R. 2008. Określanie parametrów filtracyjnych ilów krakowieckich z badań w konsolidometrze Rowe'a. *Geologia* 34, 4, 677-689.
- [24] Mikasa, M., Takada, N. 1986. Determination of coefficient of consolidation (c_v) for large strain and variable c_v values. In: Consolidation of soils, ASTM STP 892, R.N. Young and F.C. Townsend, Eds. American Society for Testing and Materials, Philadelphia, pp. 526-547.
- [25] Lovisa, J., Sivakugan, N. 2013. An in-depth comparison of c_v values determined using common curve-fitting techniques. *Geotechnical Testing Journal* 36, 1, 1-10. DOI: 10.1520/GTJ20120038
- [26] Sebai, S., Belkacemi, S. 2016. Consolidation coefficient by combined probabilistic and least residuals methods. *Geotechnical Testing Journal* 39, 5, 891-897. DOI: 10.1520/GTJ20150197
- [27] Feng, T.W., Lee, Y.J. 2001. Coefficient of consolidation from the linear segment of $t_{1/2}$ curve. *Canadian Geotechnical Journal* 38, 4, 901-909. DOI: 10.1139/t01-008
- [28] Tewatia, S.K, Venkatachalam, K. 1997. Improved \sqrt{t} method to evaluate consolidation test results. *Geotechnical Testing Journal* 20, 1, 121-125. DOI: 10.1520/GTJ11426J
- [29] ISO 14688-2:2017. Geotechnical investigation and testing. Identification and classification of soil. Part 2: Principles for a classification.
- [30] ISO 12677-2: 2007. Chemical analysis of aluminosilicate refractory products (alternative to the X-ray fluorescence method). Part 2: Wet chemical analysis.
- [31] Dobak, P., Gaszyński, J. 2015. Evaluation of soil permeability from consolidation analysis based on Terzaghi's and Biot's theory. *Geological Quarterly* 59, 2, 373-381. DOI: 10.7306/gq.1197
- [32] Terzaghi, K., Peck, R.B. 1967. *Soil Mechanics in Engineering Practice*. John Wiley & Sons, New York.
- [33] Cortellazzo, G. 2002. Comparison between laboratory and in situ values of the coefficient of primary consolidation c_v . *Canadian Geotechnical Journal* 39, 1, 103-110. DOI: 10.1139/t01-080
- [34] Chan, A.H.C. 2003. Determination of the coefficient of consolidation using a least squares method. *Géotechnique* 53, 7, 673-678. DOI:10.1680/geot.2003.53.7.673
- [35] Shukla, S. K., Sivakugan, N., Das, B. M. 2009. Methods for determination of the coefficient of consolidation and field observations of time rate of settlement - An Overview. *International Journal of Geotechnical Engineering* 3, 1, 89-108. DOI:10.3328/IJGE.2009.03.01.89-108

THE EFFECTS OF THE GEOMETRIC PARAMETERS OF A CIRCULAR SHALLOW FOUNDATION ON ITS UPLIFT BEARING CAPACITY IN LOESS SOIL

UČINKI GEOMETRIJSKIH PARAMETROV KROŽNEGA PLITVEGA TEMELJA NA NJEGOVO NOSILNOST NA IZVLEK V RAHLIH ZEMLJINAH

Cui Qiang

China Electric Power Research Institute, Transmission and Transformation Eng. Dep.
Beijing 102401, China
E-mail: everjsl@126.com

Ruiming Tong

China Electric Power Research Institute, Transmission and Transformation Eng. Dep.
Beijing 102401, China
E-mail: 18613839823@163.com

Zhenhua Zhang (corresponding author)

Hefei University of Technology, School of Civil Engineering
Hefei 230009, China
E-mail: zenithzhang@sina.com

Zhongcheng Lv

Jinshuitan Hydropower Plant of State Grid, Zhejiang electric power co., Ltd.
Lishui 323000, China

DOI <https://doi.org/10.18690/actageotechslov.15.2.74-80.2018>

Keywords

field uplift tests; circular shallow foundation; orthogonal test method; the uplift bearing capacity

Abstract

In order to reveal the effect of the geometric size parameter of a circular shallow foundation on its uplift capacity in loess soil, the shaft diameter d , the enlarge angle of the slab θ and the embedment ratio h_f/D of the shallow foundation were chosen to determine the field test schemes using the orthogonal test method. The field uplift tests were carried out on the tested foundations at a site located in Gangu County, Tianshui City, Gansu Province, China. The uplift load vs. the outward displacement curves of all the test foundations were recorded using automatic electronic measuring instrument. The test results reveal that all the uplift load vs. outward displacement curves of the tested foundations are non-linear and take on an obvious three stages. Through the analysis on all the uplift load vs. outward displacement curves, the uplift capacities are achieved using the L_1 - L_2 graphic method. By analyzing the relationship between the uplift capacities and the geometric parameters (enlarge angle of slab θ , the embedment ratio h_f/D and the shaft diameter d) of the tested foundations, it is concluded that the uplift capacities of all the tested foundations increase with the increase of θ , h_f/D and d , and the influencing degree of the three geometric factors on the uplift capacity of the circular shallow foundation is $\theta > d > h_f/D$.

Ključne besede

terenski preizkusi na izvlek; krožni plitvi temelj; ortogonalna preizkusna metoda; nosilnost na izvlek

Izvleček

Za ugotovitev vpliva geometrijske velikosti krožnega plitvega temelja na njegovo nosilnost na izvlek v rahlih zemljinah, so bili izbrani parametri premer temelja d , povečevalni kot plošče θ in razmerje vkopanja h_f/D plitvega temelja, s katerimi je določena shema terenskega preizkusa z uporabo ortogonalne preizkusne metode. Terenski preizkusi na izvlek so bili izvedeni na preizkušanih temeljih na gradbišču v okrožju Gangu, v mestu Tianshui, provinca Gansu, Kitajska. Krivulje odnosa med obremenitvijo na izvlek in zunanjih pomikov smo za vse preizkusne temelje zabeležili z avtomatskim elektronskim merilnim instrumentom. Rezultati preizkusa kažejo, da so vse krivulje obremenitev na izvlek - zunanji pomik na preizkušanih temeljih nelinearne, in da imajo izražene tri faze. Pri analiziranju krivulj obremenitev na izvlek - zunanji pomik so bile nosilnosti na izvlek dobljene z uporabo grafične metode L_1 - L_2 . Z analizo razmerja med nosilnostjo na izvlek in geometrijskimi parametri (povečevalni kot plošče θ , razmerje vkopanja h_f/D in premer temelja d) preizkušanih temeljev smo zaključili, da se nosilnost na izvlek pri vseh preizkušanih temeljih poveča s povečanjem θ , h_f/D in d , ter da je vplivna stopnja treh geometrijskih parametrov na izvlek krožnega plitvega temelja v razmerju $\theta > d > h_f/D$.

1 INTRODUCTION

Transmission towers not only transmit heavy compressive loads but also bear a considerable amount of uplift loads. The transmission towers need footings to fix them, which can anchor these towers with competent strata. Shallow foundations are widely used to bear the transmission towers. A circular shallow foundation is a very popular type of shallow foundation to support a transmission tower. Since the controlling design load for this type foundation is normally the uplift load stipulated by codes, the determination of the uplift bearing capacity of this kind of foundation is a key job for the foundation design. In deed, the factors to affect the uplift bearing capacity of a circular shallow foundation include the soil shear strength around the foundation, the geometric parameter of the foundation, the material of the foundation, etc.

Many researchers have studied how the factors influence on the uplift bearing capacity of shallow foundations. The studies were mostly conducted using indoor model experiments [1, 2, 3, 4, 5, 6, 7, 8, 9]. It is known to all that the results obtained by indoor model experiments are hard to use as a guide prototype foundation design because model experiments are always not satisfied with similarity theory. Therefore, some researchers carried out prototype pullout tests to discuss the features of the uplift load vs. outward displacement curves and the uncertainties of the parameters to fit the curves of the foundations in the Gobi field in the Northwest of China [10]. However, how multiple geometric parameters of shallow foundation influence the uplift capacity is hardly observed in the literature.

Although the effects of the geometric parameters of a shallow foundation on its uplift bearing capacity have been reported in many studies, only a limited number study the effects using prototype experiments [11,12,13]. Moreover, the prototype uplift tests reported in the literature mentioned above almost do not care for the effects of geometric parameters such as the enlarge angle of slab θ , the embedment ratio h_t/D and the shaft diameter d on the uplift bearing capacities of shallow foundations, except for some test results on the effects of normalized embedment depths (H/D) on the uplift performance of shallow foundations reported in these studies [11,12,13].

In order to understand well the effects of the geometric size parameters (enlarge angle of slab θ , embedment ratio h_t/D and shaft diameter d) of a shallow foundation on its uplift bearing capacity, in this paper, prototype uplift field tests were performed in loess soil located in northwest China, and variations of the uplift bearing capacities of the circular shallow foundations with different geometric parameters are discussed.

2 FIELD CONDITIONS

The field tests were conducted at a site located in the place of the 750-kV substation to be built in Gangu County, Tianshui City, Gansu Province, China. All the tested foundations were buried in one soil layer with relatively homogeneous loess soil. Both laboratory and in-situ tests were performed to determine the physical and mechanical parameters of the loess soil (Table 1).

Table 1. Physical and mechanical parameters of the loess soil.

Index properties for loess	Test result
Water content / %	16.5
Nature density / $\text{kg}\cdot\text{m}^{-3}$	1.89
Degree of saturation / %	43.2
Void ratio e	0.92
Liquid limit / %	30.2
Plastic limit / %	20.5
Modulus of compressibility/ kPa	15.2
Cohesion / kPa	14.8
Angle of internal friction / °	23.1

3 TEST SCHEME DESIGN

The orthogonal experimental design method is a mathematical statistical method to use an orthogonal table to study a specific indicator law determined by multiple factors. Users do fewer tests, and the regulations resulting from the tests can be found using this method [14]. The key steps of orthogonal experimental design are selecting factors for tests and determining the levels of each factor.

For the purpose of studying the effects of geometric parameters on the uplift bearing capacity of the circular shallow foundation, the orthogonal experimental design method was adopted to design the test schemes. The uplift bearing capacities of the tested foundations, which consists of a cylindrical shaft and a circular slab (Figure 1), are affected by geometric parameters such as the foundation shaft diameter d , the enlarge angle of slab θ and the embedment ratio h_t/D . Different geometric parameters have different effect degrees on the uplift bearing capacity of the foundation. In order to comprehensively analyze the effects of the three parameters on the uplift bearing capacity, the geometric parameters d , θ , and h_t/D were chosen for study. Each of the three factors (the three geometric parameters) were divided into three levels (Table 2). The parameters h_t/D , θ and d are indicated by A, B and C, respectively, in Table 2, and other geometric parameters are shown in Table 3.

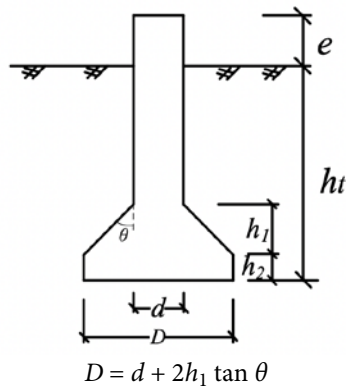


Figure 1. Schematic diagram of the tested foundations.

The standard orthogonal test table for the geometric parameters was used to develop the test schemes [15]. The test indicators are the uplift bearing capacity values of the tested foundations, whose geometric parameters are shown in Table 2 and Table 3. The test schemes are shown in Table 4, where *E* indicates a blank column, and the orthogonal table of factors and levels is shown in Table 4.

Table 2. Factors and levels of geometric parameters.

index	Factors (geometric parameters)		
	A h_t/D	B θ (°)	C d (mm)
1	1.5	15	900
2	2	30	1200
3	2.5	45	1500

Table 3. Other geometric parameters of the tested foundations.

parameter	value/mm
h_1	600
h_2	200
e	200

Table 4. Test schemes obtained by orthogonal experiment for L9 (3⁴).

Number	1	2	3	4	<i>D</i> value in figure 1
	A	B	C	E	
No.1	1(1.5)	1(15)	1(900)	1	1221
No.2	1(1.5)	2(30)	2(1200)	2	1892
No.3	1(1.5)	3(45)	3(1500)	3	2699
No.4	2(2.0)	1(15)	2(1200)	3	1521
No.5	2(2.0)	2(30)	3(1500)	1	2192
No.6	2(2.0)	3(45)	1(900)	2	2099
No.7	3(2.5)	1(15)	3(1500)	2	1821
No.8	3(2.5)	2(30)	1(900)	3	1592
No.9	3(2.5)	3(45)	2(1200)	1	2399

4 PREPARATION OF THE TESTED FOUNDATIONS

The circular shallow foundations were constructed in the field. The construction procedure is a borehole with a certain size made using the manual digging method; then the reinforcement cage was placed into the

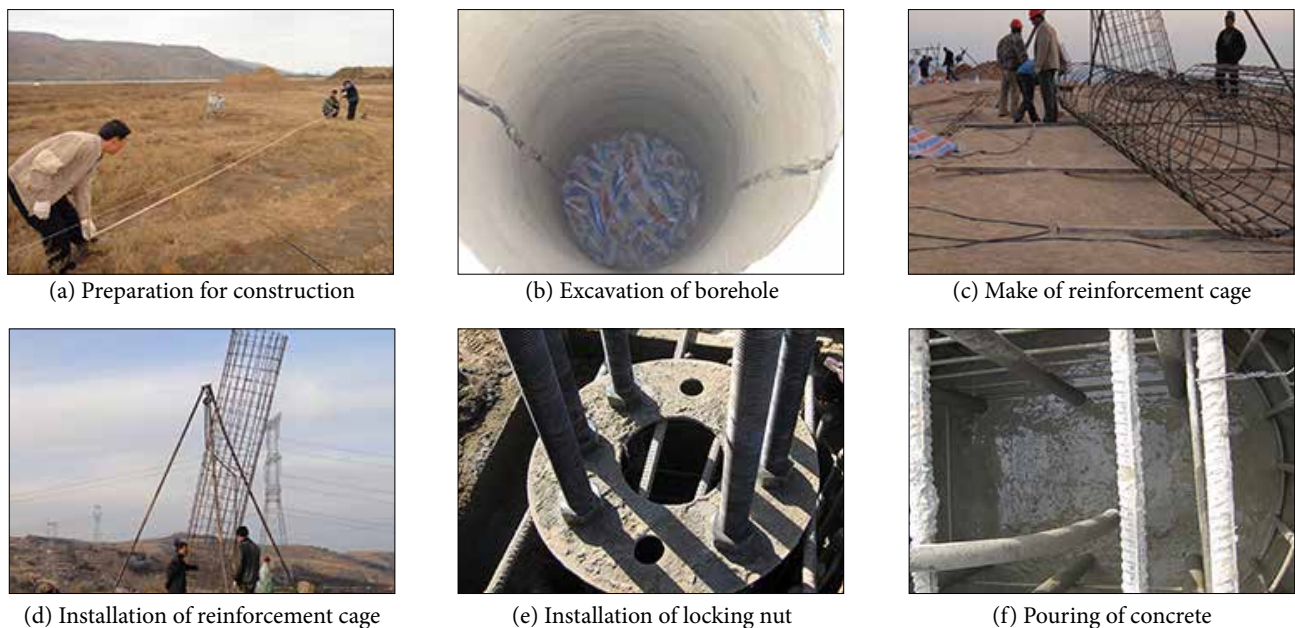


Figure 2. Construction process for the tested foundations.

borehole; after that the concrete with the compression strength of 30 MPa was placed into the hole. Finally, the foundation construction was cured for 28 days. After the process of construction, the foundation can be used for uplift tests. The construction process of the circular shallow foundation is shown in Figure 2.

5 UPLIFT TESTS

5.1 Uplift-test setup

The test setup was designed according to the criteria recommended in the Chinese Nation Code GB50007 [16] and the China Electric Power Industry Standard DL/ T 5219 [17]. The uplift test setup is a loading device shown in Figure 3. The loading device is composed of concrete supporting blocks, reaction beams made of reinforced steel plate and stiffeners, tension connecting bolts, etc. To allow the test foundations to develop possible rupture surfaces extending to the ground, the reaction beams were placed 10 m apart, perpendicular to the concrete supporting blocks. All the reaction beams were reinforced by welded steel plates and stiffeners to increase their stiffness. Based on the anticipated ultimate uplift bearing capacity of the tested foundations, tensile loading was applied by two 5000-kN hydraulic jacks using automatic electronic control with a stroke of 250 mm through the loading reaction beams. During each test, the head displacement of the tested foundation was measured by electronic gauges with a range of 50 mm. These gauges were attached to the reference beams installed over the tested foundation. The reference beams were of sufficient stiffness to support the instrumentation so that excessive variations did not occur. The same loading, reaction, and data-acquisition systems were used for all the tests. The loading direction supplied by the device is along the axial direction of the tested foundations.

5.2 Process of the uplift test

In general, the uplift test procedures of the tested foundation were conducted in accordance with the Chinese Nation Code GB50007 [16] and the China Electric Power Industry Standard DL/T 5219 [17]. All the tests were conducted with static loading, without load cycling. The process of the uplift test can be described as involving the following steps:

- (1) The slowly maintained load method [17] was adopted to load on the tested foundation, that is to say, the uplift loading was applied in increments of 10% of the anticipated ultimate load for each individual foundation, and the foundation was allowed to move under each maintained-load increment until a certain rate of displacement was achieved.
- (2) Each load increment was maintained after loading until the change rate of the outward displacement was less than 0.1 mm/h.
- (3) Then the next load increment was applied. The uplift test was continued up to the point of failure, at which the foundation was completely pulled out from the loess, or the uplift test was terminated after the last load was maintained for 24 h with the change rate of displacement exceeding 0.1mm/h.

6 TEST RESULTS

6.1 Uplift load vs. outward displacement curves

The measured uplift load vs. outward displacement curves for all the tested foundations are presented in Figure 4. It is clear from Figure 4 that the uplift load vs. displacement curves exhibit the same three stages, which are segment *oa*, segment *ab* and segment *bc* in the curve (Figure 5).

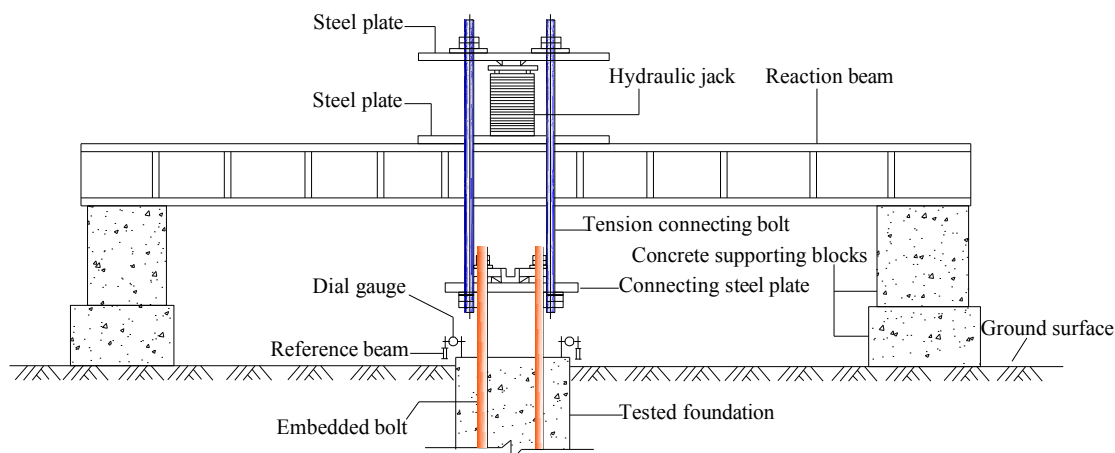


Figure 3. Loading device for uplift tests.

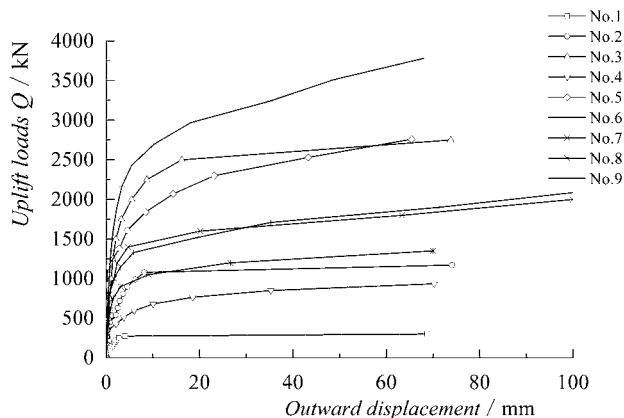


Figure 4. Uplift load vs. outward displacement curves of tested foundations.

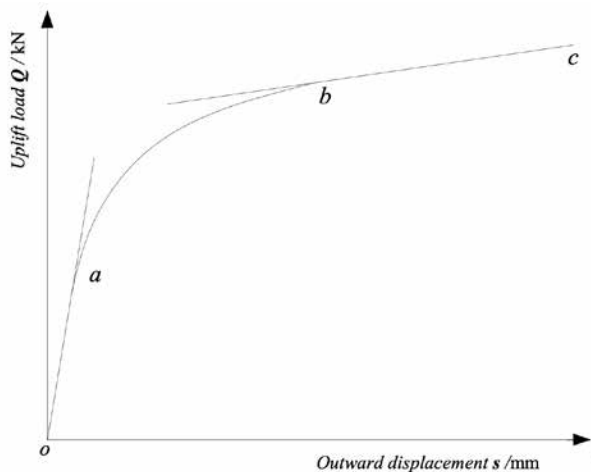


Figure 5. Three stages of uplift load vs. displacement curve.

Among these segments, segment *oa* is a straight line, where elastic deformation can be thought to occur in the loess soil around the tested foundation, and compressive deformation of the soil is dominant at this stage; the middle segment *ab* is a curve as the transition stage, indicating that plastic deformation occurs in the soil occasionally with elastic-plastic deformation, and the soil mainly takes on compressive and shear deformation; the terminal segment *bc* is a straight line with a gentle slope, and the main deformation is shear deformation in this stage.

6.2 Uplift capacity of the tested foundations

Based on the uplift load vs. outward displacement curves, the uplift bearing capacities of the tested foundations can be determined using the L_1 - L_2 graphic method [18]. The method takes two steps to determine the uplift capacity of the tested foundation. Specifically, the two steps are illustrated as the following.

- (1) the first step is extending the terminal segment *bc* from the last point (point *c* in Figure 5) in the uplift load vs. outward displacement curve, and then finding the intersection (point *b* in Figure 5) between the middle section *ab* and the terminal section *bc*;
- (2) the second step is finding the value of the vertical coordinate in point *b*, and the value is the uplift bearing capacity (Q_{L2} in Figure 6).

Table 5. The uplift capacities of the test foundations.

Numbers	h_f/D	enlarge angle $\theta/^\circ$	shaft diameter d/mm	uplift bearing capacities Q_{un}/kN
No.1		15	900	269
No.2	1.5	30	1200	943
No.3		45	1500	2037
No.4		15	1200	581
No.5	2.0	30	1500	1638
No.6		45	900	1319
No.7		15	1500	1403
No.8	2.5	30	900	1108
No.9		45	1200	2422

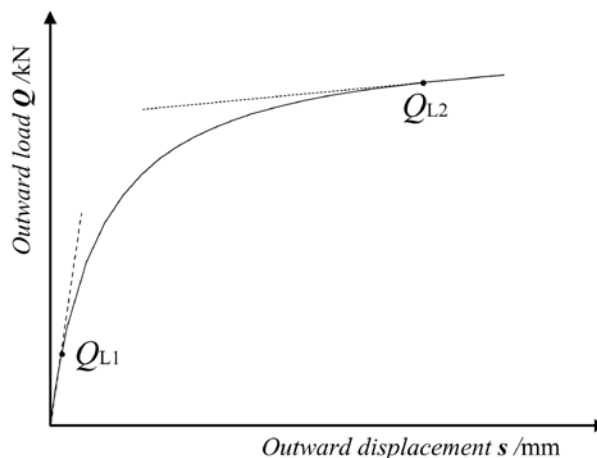


Figure 6. Graphical expression of the uplift bearing capacity of the tested foundation.

7 DISCUSSION

The uplift bearing capacities and geometric parameters of all the tested foundations are presented in Table 5. The effects of various geometric parameters on the uplift bearing capacities are discussed in terms of the test results mentioned above.

It has been shown in Table 5 that when the embedment ratio (h_t/D) equals 1.5, the uplift bearing capacities Q_{nu} increase with the increase in the enlarged angle of the slab ($\theta = 15, 30$ and 45°). Nevertheless, when the embedment ratio (h_t/D) equals 2.0 or 2.5, Q_{nu} does not increase anymore with the increase in enlarged angle of the slab θ due to the effect of the shaft diameter (d). Therefore, the uplift bearing capacities Q_{nu} of the tested foundations are influenced jointly by multiple geometric parameters of the foundation.

For analyzing the effects of multiple geometric parameters (h_t/D , θ and d) on the uplift bearing capacities Q_{nu} of the tested foundations, an orthogonal analysis was made on the test results, and the analysis results were listed in Table 6. In Table 6 the three lines K_1 , K_2 and K_3 represent, respectively, the sum of the three Q_{nu} values at Level 1, 2 and 3 of each factor (A , or B , or C), and \bar{K}_1 , \bar{K}_2 and \bar{K}_3 are the averages of the three Q_{nu} values at Level 1, 2 and 3 of each factor (A , or B , or C). It is clear from Table 6 that for the column of factor A (embedment ratio h_t/D), $\bar{K}_1 < \bar{K}_2 < \bar{K}_3$; for the column of factor B (enlarge angle θ), $\bar{K}_1 < \bar{K}_2 < \bar{K}_3$; and for the column of factor C (shaft diameter d), $\bar{K}_1 < \bar{K}_2 < \bar{K}_3$. So the best combination of the three factors to approach the maximum uplift bearing capacity of the foundation is $A_3B_3C_3$. The maximum uplift bearing capacity (2,422kN) in Table 6 occurs in group No.9, whose combination of the three factors is $A_3B_3C_1$, while the minimum uplift bearing capacity (269kN) can be found in group No.1 with the combination of $A_1B_1C_1$.

The difference between the maximum and the minimum of the three numbers in same column (A , or B , or C) is expressed by R in Table 6. If the value of R in each column varies differently, the level changes of the factor in the column have different effects on the uplift bearing capacity. From the variable range of R in each column in Table 6, it can be known that among the three factors (column diameter d , embedment ratio h_t/D and enlarge angle θ), the enlarged angle θ is the most sensitive to the uplift bearing capacity Q_{nu} of the foundation, the shaft diameter d is secondary, and the embedment ratio h_t/D is the least.

The trend of the uplift bearing capacities Q_{nu} for the foundations under different levels of each factor was demonstrated in Figure 7. It can be observed in Figure 7 that the enlarged angle θ has significant effects on the uplift bearing capacity Q_{nu} to be specific, when θ increases from 15° to 45° , Q_{nu} will increase by 156%; while the embedment ratio h_t/D has the least effect on Q_{nu} among the three factors, specifically, when h_t/D increases to 2.5 from 1.5, Q_{nu} will increase by 52%; the effect degree of the shaft diameter d on Q_{nu} is between those of θ and h_t/D .

Table 6. Analysis of the uplift capacity.

No	factors			Q_{nu}/kN
	A embedment ratio h_t/D	B enlarge angle θ	C shaft di- ameter d	
1	1	1	1	269
2	1	2	2	943
3	1	3	3	2037
4	2	1	3	581
5	2	2	1	1638
6	2	3	2	1319
7	3	1	2	1403
8	3	2	3	1108
9	3	3	1	2422
K_1	3249	2253	2696	
K_2	3538	3689	3946	
K_3	4933	5778	5078	
\bar{K}_1	1083	751	899	
\bar{K}_2	1179	1230	1315	
\bar{K}_3	1644	1926	1693	
R	561	1175	794	

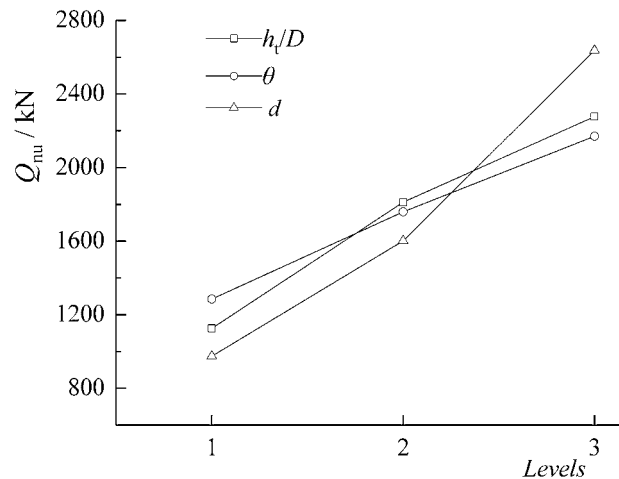


Figure 7. The trend of the uplift capacity under different factors and levels.

8 CONCLUSIONS

Based on the test results and discussions mentioned above, the conclusions can be drawn as follows:

- (1) The uplift load vs. outward displacement curves of the circular shallow foundations in loess soil are

non-linear in general, and they take on three stages, of which, one stage is a curve, and the other two are straight. From the angle of engineering, the three stages represent the stage (*oa*) of elastic deformation, the stage (*ab*) of appearance and the extension of the plastic zone, and the stage (*bc*) of shear failure in loess soils around the tested foundations;

- (2) The uplift bearing capacities of the circular shallow foundations in loess is related to the shaft diameter d , the embedment ratio h_i/D and the enlarge angle θ . With the increases in the three geometric parameters (d , h_i/D and θ) not only at the same time but also respectively, the uplift bearing capacities of the circular shallow foundations will increase;
- (3) The discussions relating to the test results show that the sensitivity of each geometric parameter to the uplift bearing capacity of the foundation circular shallow foundation in loess soil from large to small is $\theta > d > h_i/D$.

Acknowledgment

We acknowledge the National Natural Science Foundation of China under Grant No.51108435.

REFERENCES

- [1] Matsuo, M. 1967. Study on the Uplift Resistance of Footing (1). *J. Soils and Foundations* 7, 4, 1-37. Doi:10.3208/sandf1960.7.4_1
- [2] Matsuo, M. 1968. Study on the Uplift Resistance of Footing (2). *J. Soils and Foundations* 5, 4, 62-98. Doi:10.3208/sandf1960.8.18
- [3] Dickin, E.A., Leung, C. F. 1990. Performance of piles with enlarged bases subject to uplift force. *Canadian Geotechnical Journal* 27, 5, 546-556. Doi:10.1139/t90-070
- [4] Dickin, E.A., Leung, C.F. 1992. The influence of foundation geometry on the uplift behavior of piles with enlarged bases. *Canadian Geotechnical Journal* 29, 3, 498-505. Doi:10.1139/t92-054
- [5] El Naggar, M.H., Wei, J.K. 2000. Uplift behavior of tapered piles established from model piles. *Canadian Geotechnical Journal* 37, 1, 56-74. Doi:10.1139/t99-090
- [6] Liu, W.B., Zhou, J., Temuer, M.K. 2003. Uplift tests and calculations of under-reamed piles. *Industrial Construction* 33, 4, 42-45 (in Chinese).
- [7] Chen, R.P., Zhang, G.Q., Kong, L.G., etc. 2010. Large-scale tests on uplift ultimate bearing capacities of enlarged base piles in saturated and unsaturated silty soils. *Chinese Journal of Rock Mechanics and Engineering* 29, 5, 1068-1074 (in Chinese).
- [8] Yu, H. 2011. Influence of Pile Deformation Resistance to Pull Enlarged end of Performance Factors. *Logistics Engineering and Management* 33, 5, 120-121 (in Chinese). Doi:10.3969/j
- [9] Li, B.Z., Chen, Y. 2015. The bearing capacity analysis on straight chimney excavation foundation with different chimney and enlarged bottom. *Industrial Construction* 45, S1, 1019-1022 (in Chinese).
- [10] Lu, X.L., Qian, Z.Z., Tong, R.M. 2014. Uplift load-movement response of bell pier foundations in Gobi gravel. *Geotechnical Engineering* 164, 4, 380-389. Doi:10.1680/geng.12.00072
- [11] Consoil, N.C., Ruver, C.A., Schnaid, F. 2013. Uplift Performance of Anchor Plates Embedded in Cement-Stabilized Backfill. *Journal of Geotechnical and Geoenvironmental Engineering* 139, 3, 511-517. Doi:10.1061/(ASCE)GT.1943-5606.0000785
- [12] Consoli, N.C., Ruver, C.A., Girardello, V. etc. 2012. Effect of polypropylene fibers on the uplift behavior of model footings embedded in sand. *Geosynthetic International* 19, 1, 79-84. Doi:10.1680/gein.2012.19.1.79
- [13] Consoli, N.C., Thomé, A., Girardello, V. etc. 2012. Uplift behavior of plates embedded in fiber-reinforced cement stabilized backfill. *Geotextiles and Geomembranes* 35, 107-111. Doi: 10.1016/j.geotextmem.2012.09.002
- [14] Box, G.E.P., Hunter, W.G., Hunter, J.S. 1978. *Statistics for experimenters*. Wiley-Interscience, New York. Doi:10.2307/1267766
- [15] Yang, Z.X. 1978. *Construction of orthogonal tables*. Shandong People Press, JI Nan (in Chinese).
- [16] China Ministry of housing and construction 2010. *Code for design of building foundations GB50007-2011*. China Architecture and Building Press, Beijing (in Chinese).
- [17] ZhongNan Engineering Corporation Limited 2015. *Technical code for design of foundation of overhead transmission line DL/T5219-2014*. China Electric Power Press, Beijing (in Chinese).
- [18] Chen, Y.J., Chu, T.H. 2012. Evaluation of uplift interpretation criteria for drilled shafts in gravelly soils. *Can. Geotech. J.* 49, 1, 70-77. Doi : 10.1139/T11-080

THE DESIGN OF DRILLED DISPLACEMENT SYSTEM PILES USING THE CAVITY EXPANSION THEORY

NAČRTOVANJE SISTEMA UVRTANIH PILOTOV Z ODMIKANJEM Z UPORABO TEORIJE RAZŠIRJANJA PROSTORA

Stacho Jakub

Slovak University of Technology in Bratislava,
Faculty of Civil Engineering
Radlinskeho 11, 810 05 Bratislava, Slovakia
E-mail: jakubstacho22@gmail.com

DOI <https://doi.org/10.18690/actageotech Slov.15.2.81-91.2018>

Keywords

pile foundation, drilled displacement system pile, cavity expansion theory, static load test

Ključne besede

temeljenje na pilotih, sistem uvrtnih pilotov z odmikanjem, teorija razširjanja prostora, statični obremenilni preizkus

Abstract

Drilled Displacement System (DDS) piles are an innovative technology for pile foundations. These DDS piles are created by rotary drilling with a simultaneous full displacement of the soil in a horizontal direction. The optimal design of DDS piles can be obtained in sandy soils and fine-grained soils that allow for a horizontal displacement, which causes an increase in the shaft's resistance. This article deals with the use of Cavity Expansion Theory (CET) for a complex analysis of DDS piles. This method makes it possible to take into account the impact of the technology in pile design. A general view of the CET is presented and is described step by step for the solution of the present problem. The results of the calculations are compared and analysed with the results of three instrumented static load tests. The analyses include a comparison of the load-settlement curve as well as the load distribution over the pile's length, which was measured using strain gauges. The results of the analyses show very good agreement between the calculations and the measurements. The difference between the calculated and measured load-settlement curves did not exceed a 10% degree of accuracy. The possibilities for the future use of CET are also discussed.

Izvleček

Uvrtni piloti z odmikanjem (DDS) predstavljajo inovativno tehnologijo za temeljenje pilotov. Pilote izvedemo po tehnologiji DDS z rotacijskim vrtnjem in hkratnim polnim odmikanjem tal v vodoravni smeri. Optimalno obliko DDS pilotov lahko dobimo v peščenih in drobnozrnatih zemljinah, ki omogočajo vodoravno odmikanje, kar povzroči povečanje nosilnosti pilota na plašču. Ta članek obravnava uporabo teorije razširjanja prostora (CET) za kompleksno analizo pilotov DDS. Ta metoda omogoča upoštevanje vpliva tehnologije pri načrtovanju pilotov. Predstavljen je splošen pregled CET ter opisani vsi koraki reševanja obravnavanega problema. Rezultate izračunov smo analizirali in primerjali z rezultati treh statičnih obremenilnih preizkusov. Analize vključujejo primerjavo krivulje obremenitev-pomik in porazdelitve obremenitve po dolžini pilota, ki je bila izmerjena z uporabo merilcev specifičnih deformacij. Rezultati analiz kažejo zelo dobro ujemanje izračunanih in izmerjenih vrednosti. Razlika med izračunanimi in izmerjenimi krivuljami obremenitev-pomik ni presegala 10 %. Predstavljene so tudi možnosti prihodnje uporabe CET.

1 INTRODUCTION

Piles are the most frequently used elements of deep foundations that are used to transfer a load from a structure to a suitable bearing stratum when the soil mass immediately below a construction is unsuitable for the direct bearing of footings. New technologies for the execution of pile foundations are constantly being developed due to the stricter requirements of modern structures. The most appropriate way of categorizing piles according to their technology is as large displacement, small displacement, and replacement piles [1]. This article focuses on Drilled Displacement System (DDS) piles. DDS technology is also known as DD (Drilled Displacement), FDP (Full Displacement Pile), or APGD (Auger Pressured Grouted Displacement) piles. DDS piles are rotary drilled piles with the full displacement of the soil in the horizontal direction, which leads to a higher bearing capacity of the pile in comparison with replacement piles (see for example [2, 3, 4]). Brown [5] published a general review of DDS technology and its advantages and disadvantages in comparison with other pile technologies.

In the past, several calculation methods for determining the ultimate resistance and load-settlement curve of the pile have been developed, for example [6, 7, 8, 9]. Zhang et al. [10] classified the calculations into five categories: simplified analytical methods, load-transfer curve methods, finite-element methods (FEMs), boundary-element methods (BEMs), and variation methods. The selection of the most appropriate method for a pile design depends on experience and availability, and plays a very important role in the accuracy of the solution. This article deals with the use of Cavity Expansion Theory (CET), published by Mecsi [11, 12], for an analysis of pile displacement. The CET theory seems to be one of the most appropriate methods for a given case, because the principles which are assumed, i.e., creating a cylindrical space (a pile body) and the horizontal displacement of the soil to the surrounding area, are very similar to the real installation process of a DDS pile. The method makes it possible to calculate the changes in soil properties that are affected by the cylindrical displacement of the soil and take them into account in the calculation.

It is difficult to summarize the results of all previous researchers, because the CET has been used for the design or analysis of many geotechnical constructions. An analysis using CET leads to useful solutions for a variety of problems in geotechnical engineering [11, 13, 14]. Examples of the applications are the bearing capacity of a displacement pile (or a partial displace-

ment pile) [15], interpretation of a pressure meter [11, 16, 17] and cone penetration tests (CPT), for example [18], and an analysis of the deformation around tunnels. The application of CET to many geotechnical solutions was published by Yu [19]. CET can be classified into a pressure-controlled cavity expansion and a displacement-controlled cavity expansion [20]. CET used for analytical solutions assumes various constitutive laws of the medium around the cavity, for example, linear elastic or elastic perfectly plastic, with or without accounting for the volume variation [21]. These theories were adopted for the soil behaviour under a small strain as well as a large strain [14, 22,]. With the advent of numerical modelling, various numerical models were used to analyse some of the problems of a cylindrical cavity for different tasks, for example [23]. Many published simulations, for example [13, 14, 24], assumed that the soil around the cavity is homogeneous and isotropic. Due to the change in the sedimentary environment and a consolidated environment, however, the initial stress in the soil layer is usually anisotropic [24]. The use of the axisymmetric CET to investigate the effect of soil parameters on the ground movement in the vicinity of static pipe-bursting operations was studied by Fernando and Moore [25]. They present a parametric study which shows that the ground movements are controlled by the soil strength and dilatancy, rather than by the elastic soil properties. The case studies prepared by Rao et al. [26] showed that it is necessary to consider the effect of the coefficient of horizontal earth pressure K_0 . Analytical solutions based on $K_0 = 1$ overestimate the critical expansion pressure and the ultimate expansion pressure as well as the plastic zone around the cavity. Li et al. [27] presented a solution that investigates the effect of the initial stress anisotropy and the initial stress-induced anisotropy on the cavity expansion by adopting parametric studies with different over-consolidation ratios (OCRs).

The results of fully instrumented static load tests on DDS piles are analysed and compared with the results of calculations using the CET. The analysis includes a comparison of the load-settlement curves as well as a comparison of the measured and calculated load distributions over the pile's length measured using strain-gauges. Detailed analyses of three tested DDS piles are presented in the article.

2 METHODOLOGY OF THE PILE DESIGN USING THE CAVITY EXPANSION THEORY

General definitions of the soil stress deformations and volume changes in the soil as well as an examination of the cylindrical expansion for a given CET were

presented by Mecsi [11]. He showed that the volume changes occurring in the soil are attributed to the laws of the soil stress forming around a cylinder. The hardening of the soil and the impact of the soil mass around the cylinder on the stress-strain state are taken into account in the calculation.

The presented theory supposes an axisymmetric stress state in the normally consolidated soil with incompressible soil grains. The anisotropic stress-strain state is taken into account in the initial conditions. It means that the compressive stresses in the vertical direction and the earth pressure at rest in the horizontal direction of the soil are assumed. The zone, where the soil density increased due to a process of enforced expansion, is also taken into account. The basic characteristics of the calculation model used are:

- application of the Mohr-Coulomb (MC) conditions (plastic stress state),
- force equilibrium,
- nonlinear relationship between increasing soil stress and soil strain,
- assumption of the elastic behaviour for the decrease of the soil stress,
- changes in the soil density are obtained as a result of the strain in three mutually perpendicular directions (the 3D effect of the soil deformation is included).

In the initial stress state, the original geostatic stress in the vertical direction and the horizontal stress at rest

are considered. Because the soil volume is changed (compressed), the plastic stress state is reached according to the MC law. The soil volume continues to change (increase) after the plastic stress state has been reached.

The following effects are applied in the calculation model:

In the area outside the zone of compaction (elastic zone):

- a nonlinear relation between the radial deformations and stresses for the compaction, and a linear one for the expansion,
- the soil density (volume) is not changed.

At the border of the compaction zone:

- the same effects are applied as for the outside zone with some supplements,
- the MC relation comes into effect.

Within the plastic stress state zone (a zone of the compaction):

- the MC relation is applied,
- a nonlinear relationship between the radial deformations and the stresses for the compaction and a linear one for the expansion.

Individual assumptions and the steps of the calculations are simply described for the presented analyses, due to the extensiveness of the theory used. The basic assumption of the presented theory is shown in Fig. 1.

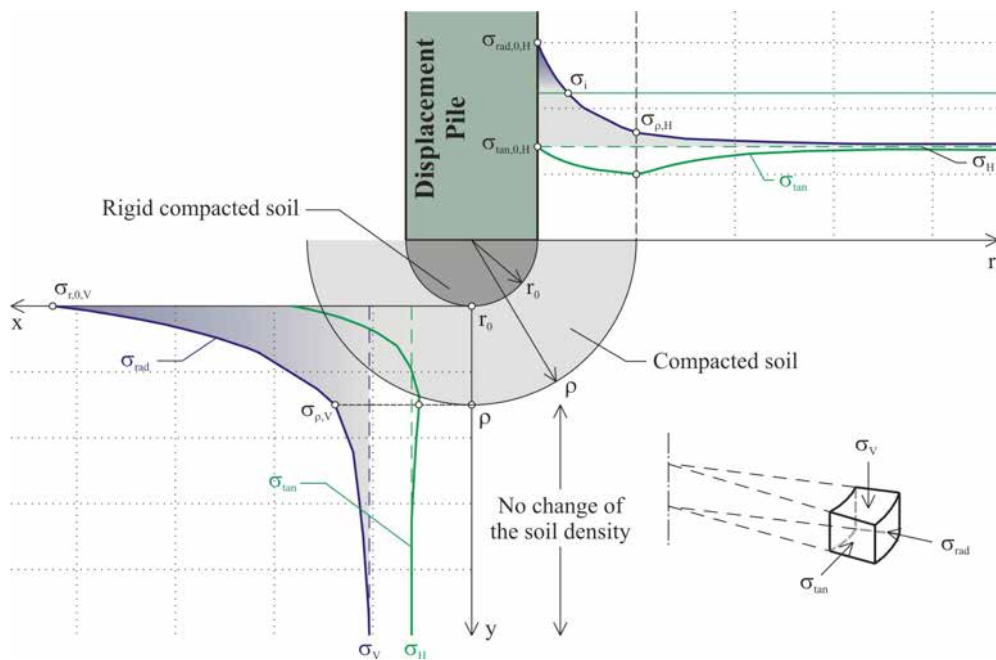


Figure 1. Description of the soil stresses near the bottom of the pile according to [11].

The distribution of the soil stresses acting beneath the pile bottom varies in the different directions. The soil immediately below the pile base becomes significantly harder after loading and a zone called the "rigid compacted soil" is created. The theory presented assumes that this fully compacted zone directly transfers a compressive load to the surrounding soil below the pile base. The radius of the fully compacted zone (rigid compacted soil) is equal to the pile radius r in the calculations. Based on this supposition, the base area of the pile in equation (5) is simply assumed to be πr^2 . When the load is applied to the pile, a spherical compacted zone is created from the bottom of the pile with the radius (ρ). In the first step of the calculations it is necessary to calculate the soil stresses at the boundary of the compacted zone ($\sigma_{r,V}$ in the vertical and $\sigma_{r,H}$ in the horizontal directions) with respect to the initial soil stresses (σ_V in the vertical and σ_H in the horizontal directions) using equations (1) and (2). The derivation process of both equations was described by Mecsi [11] in a step-by-step fashion.

$$m_r = 0 \Rightarrow \frac{\sigma_{\rho,V}^{(1-a)} - \sigma_V^{(1-a)}}{(1-a) \cdot E_0} - 2 \cdot \frac{\sigma_H - \xi \cdot (\sigma_{\rho,H} - \sigma_u)}{\sigma_H^a \cdot E_0} \Rightarrow \sigma_{\rho,V} \quad (1)$$

$$m_t = 0 \Rightarrow \frac{\sigma_{\rho,H}^{(1-a)} - \sigma_H^{(1-a)}}{(1-a) \cdot E_0} - \frac{\sigma_H - \xi \cdot (\sigma_{\rho,H} - \sigma_u)}{\sigma_H^a \cdot E_0} \Rightarrow \sigma_{\rho,H} \quad (2)$$

where m_r is the change in the volume in the radial direction, and m_t is the change in the volume in the tangential direction; σ_u is the unconfined soil strength; E_0 is the modulus of elasticity; and a is a parameter of the nonlinearity described below. This makes it possible to calculate the radius of the compaction zone ρ (extended plastic stress state), where the ultimate stress $\sigma_{r,H,limit}$ is also taken into account.

$$\rho = r_0 \cdot \left(\frac{\sigma_{r,H,limit} + \frac{c'}{\tan \varphi'}}{\sigma_{\rho,H} + \frac{c'}{\tan \varphi'}} \right)^{\frac{1+\sin \varphi'}{2 \cdot \sin \varphi'}} \quad (3)$$

The definition of the nonlinear deformation of the soil is one of the important points of the calculation. The effect of soil compaction is determined by changing the secant modulus using the parameter a . The parameter a can be determined according the results of an oedometer test. The secant modulus, which depends on the geostatic stress, is given by equation:

$$E_S = E_0 \cdot \left(\frac{\sigma}{\sigma_{ref}} \right)^a \quad (4)$$

The size of the vertical limit stress for the calculation of the ultimate pile base resistance $Q_{b,ultimate}$ is given by the difference between the vertical stress at the bottom of the pile under the load $\sigma_{r,0,V}$ and the initial geostatic stress σ_V . The value of $\sigma_{r,0,V}$ is given by equation (5). It is recom-

mended that the calculation be divided into more loading steps (from interval 0 to $Q_{b,ultimate}$) for the calculation of the load-settlement distribution under the pile base.

$$\sigma_{r,0,V} = \sigma_V + \frac{Q_b}{\pi \cdot r^2} \quad (5)$$

The distributions of the radial soil stress (σ_{rad}) and the tangential soil stress (σ_{tan}) as well as the distribution of the soil displacement ($\Sigma \Delta u_{r,i}$) allow a determination of the base resistance-soil displacement (compaction) curve. The distribution of soil stresses within the compacted (plastic) zone is statically determined under the force equilibrium and the Mohr-Coulomb conditions. The derivation process of the final equations presented was described in detail by Mecsi [11]. The radial soil stress distribution is given by the following equations:

- Inside the zone of compaction (if $r \leq \rho$):

$$\sigma_{r,V} = \left(\sigma_{\rho,V} + \frac{c'}{\tan \varphi'} \right) \cdot \left(\frac{\rho}{r} \right)^{\frac{4 \cdot \sin \varphi'}{1 + \sin \varphi'}} - \frac{c'}{\tan \varphi'} + \sigma_w \quad (6)$$

- Outside the zone of compaction (if $r > \rho$):

$$\sigma_{r,V} = (\sigma_{\rho,V} - \sigma_V) \cdot \left(\frac{\rho}{r} \right)^3 + \sigma_V \quad (7)$$

where σ_w represents the pressure of the water in the pores.

The change of the strain (in compression) is given by the equation:

$$\Delta \varepsilon_r = \frac{\sigma_{r,V}^{(1-a)} - \sigma_V^{(1-a)}}{(1-a) \cdot E_0} \quad (8)$$

and the change of the radial soil displacement is equal to:

$$\Delta u_{r,i} = \frac{\Delta \varepsilon_{r,i-1} + \Delta \varepsilon_{r,i}}{2} \cdot (r_i - r_{i-1}) \quad (9)$$

The shaft resistance and finally the load-settlement curve of the pile can be subsequently calculated after all the previous steps. The ultimate stress in the horizontal direction for the calculation of the ultimate shaft resistance is equal to:

$$\sigma_{r,H,limit} = \frac{\kappa \cdot \sigma_H}{\xi} + \frac{2 \cdot c'}{\sqrt{\xi}} \quad (10)$$

where κ is a multiple factor for the impact of the technology. Based on the Mohr-Coulomb relationship, the ratio of the principal stresses ξ can be expressed with the following correlation:

$$\xi = \frac{1 - \sin \varphi'}{1 + \sin \varphi'} \quad (11)$$

The ultimate shaft resistance of the pile is given by the ultimate shear strength along the pile using Coulomb's relationship:

$$\tau_{ult} = \sigma_{r,H,limit} \cdot \tan \varphi' + c' \quad (12)$$

and the shear resistance is given by the following equation:

$$t_{ult} = U_z \cdot \tau_{ult} \quad (13)$$

where U_z is the diameter of the pile at a depth z from the top of the pile.

Generally, the shear resistance is given by the equation:

$$t = \frac{u_{b+s}}{\Delta_M} \cdot t_{ult} \quad (14)$$

Elastic behaviour is considered up to the displacement Δ_M , which is required for the full mobilization of the shaft friction and u_{b+s} is the sum of the deformation of

the pile base and the pile shaft (settlement of the soil below the pile base and the axial compression of the pile body). When the value of Δ_M is reached, the plastic stresses are taken into account.

3 GEOLOGICAL CONDITIONS OF THE TESTED AREA

The geological conditions of the tested area consist of very soft layers with a thickness of about 13-15 m and very dense coarse-grained soils below them. The geologi-

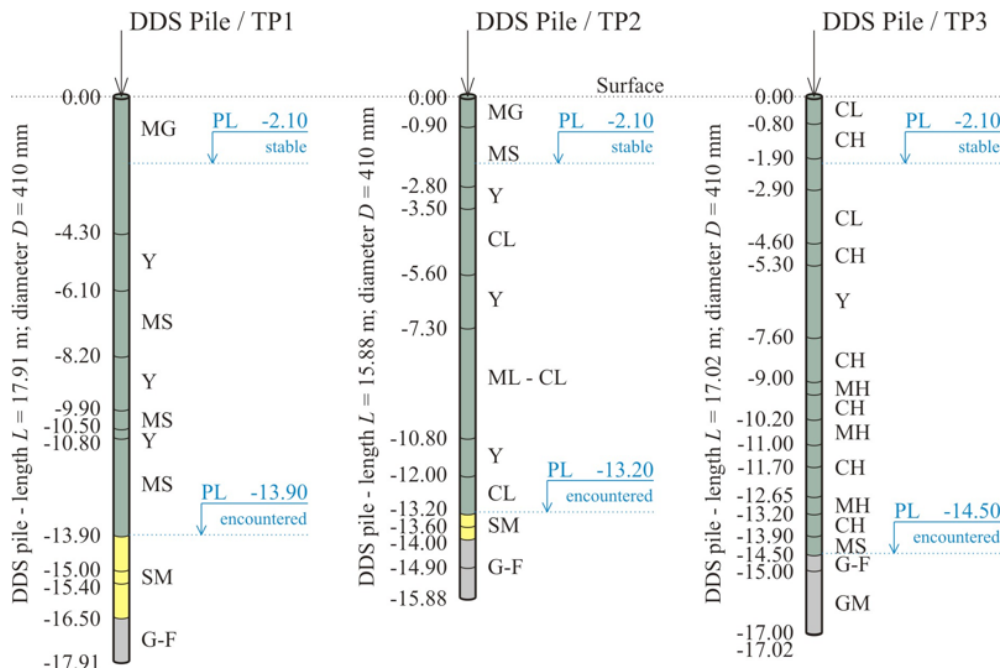


Figure 2. Geotechnical models of the analysed piles.

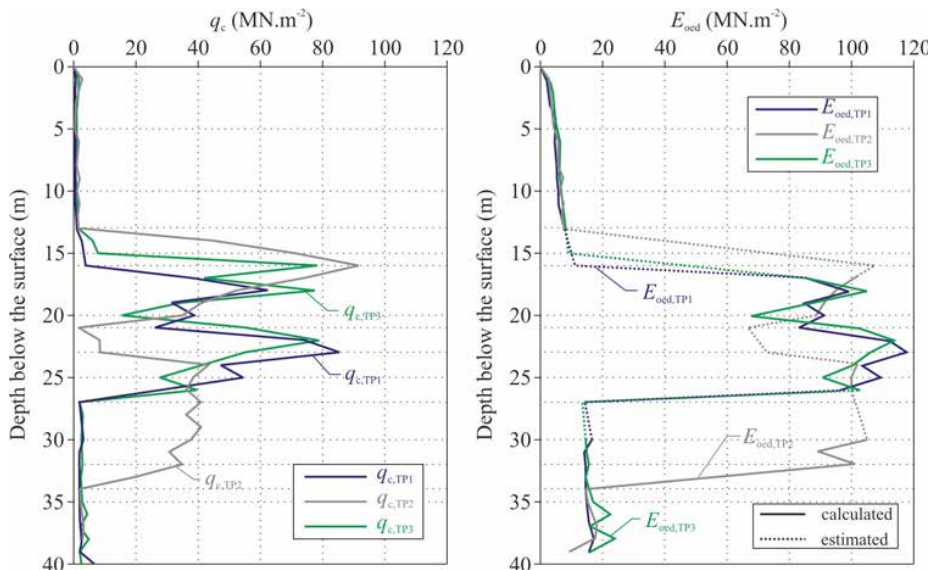


Figure 3. Results of CPT tests in the tested area.

Table 1. Soil properties used in the calculation.

Test pile	TP1			TP2			TP3	
	F	S	G	F	S	G	F	G
Symbol of soil	F	S	G	F	S	G	F	G
Depth (m)	-	13.90	16.50	-	13.20	14.00	-	14.50
Thickness (m)	13.90	2.60	1.41	13.20	0.80	1.88	14.50	2.52
γ (kN.m ⁻³)	19	18	19	19	18	19	19	19
γ_{sat} (kN.m ⁻³)	20	20	21	20	20	21	20	21
ϕ' (°)	20	28	37.5	20	28	37.5	20	37.5
c' (kN.m ⁻²)	20	10	1	20	10	1	20	0
E_s (kN.m ⁻²)	5160	28140	112000	6990	28140	117600	6600	119900
a (-)	0.5	0.4	0.1	0.5	0.4	0.3	0.5	0.3

cal profiles for the tested piles are shown in Fig. 2. The stratum of soft soil (0.00 to 13.20~14.50) is especially represented by sandy silts (MS), stiff silts, clays with low plasticity (ML-CL), and layers of organic clays (Y). In the case of TP3, soft soils were classified as clays with high plasticity (CH) and silts with high plasticity (MH). In the cases of TP1 and TP2, coarse-grained soils consist of silty sands (SM) of a thickness of 2.6 m (TP1) and 0.8 m (TP2). Very dense gravels with fine soils (G-F) are located below the sandy layers. In the case of TP3, coarse-grained soils consist of gravels with fine soils (G-F) and silty gravels (GM) immediately below the soft stratum.

An engineering-geological survey that was executed on the area of the tested piles included many in-situ tests and also standard laboratory tests [28]. The following were executed: 48 SPT tests, 54 CPT tests, 17 DPH tests, 10 piezometers and core drillings. The distributions of q_c and E_{oed} obtained using the correlation from the CPT test in the area of the tested piles are shown in Fig. 3. The soil properties used in the calculation are shown in Table 1.

Based on the results of the in-situ tests, the soft layers (0 to 13.20~14.50) have about the same mechanical soil properties. For this reason, the soft stratum is considered as homogeneous (separately in all profiles). The layer is marked using the symbol F (Table 1). The effective shear strength parameters ϕ' and c' were taken into account according to the results from the test report [28]. The impact of the groundwater was taken into account as a phreatic level under the pressure. The pore pressure was estimated as the difference between the encountered and the stable groundwater level (for example, TP2: (13.20 m to 2.10 m) * 10 kN.m⁻³ = 111 kN.m⁻²).

4 EXECUTION OF THE STATIC LOAD TEST

A static load test (SLT) is the most accurate method for pile design [7]. The fully instrumented SLT makes it

possible to obtain a complex overview of the interaction between the pile and the soils. The tested piles (TPs) were about 15 to 18 m long with a diameter of 410 mm. TP1 is 17.91 m long and anchored over 4.01 m into coarse-grained soils; TP2 is 15.88 m long and anchored over 2.68 m into coarse-grained soils; TP3 is 17.02 m long and is anchored over 2.52 m (Fig. 2). The settlement of the pile head, the horizontal aberration, the uplift of the reaction piles, and the distribution of the load over the pile's length using strain-gauges were recorded during the SLT and this allowed for a detailed analysis of the DDS pile. The static load tests were executed in 333-kN steps up to a maximum load of 2000 kN, including the unloading steps. As an example of the execution of the SLT of TP2: in the first phase of the SLT, the vertical load reached 1333 kN in four loading steps. After the unloading in the second step, the vertical load was increased to 2000 kN (in 333 kN steps) in the third phase. The unloading to 0 kN was carried out in the last

**Figure 4.** Details of the set up for the sensors in the static load test.

phase. The details of the set up for the sensors in the static load test are shown in Fig. 4.

5 COMPARISON OF THE RESULTS CALCULATED USING THE CET WITH THE RESULTS OBTAINED BY THE SLT

The load-settlement curves and the load distributions over the pile's length, which are calculated using the CET, are compared and analysed with the results of measurements obtained from the SLT. The analysis of the load-settlement curve and the load distribution over the pile's length plays a significant role and confirms the correctness of the calculation, because an analysis of only load-settlement curves could lead to a mistake in the evaluation of the pile resistance, as has been presented by, for example, Tosinini et al. [29]. The analysis of TP2 is presented in detail, step by step, according to the previous description of the calculation methodology.

Initially, the calculations of the pile-base resistance as well as the displacement below the pile base are presented. The increase in the radial stress $\sigma_{rad,i}$ in comparison with the geostatic stress $\sigma_{V,i}$ under the pile base is presented in Fig. 5. The values of $\sigma_{rad,i}$ are shown from a depth of $z = 0.205$ m, which is a rigid compaction of the soil, and is equal to the radius of the pile. The distributions of the tangential soil stress under the pile base $\sigma_{tan,i}$, compared with the horizontal geostatic stress at the rest $\sigma_{H,i}$ are also shown in Fig. 5.

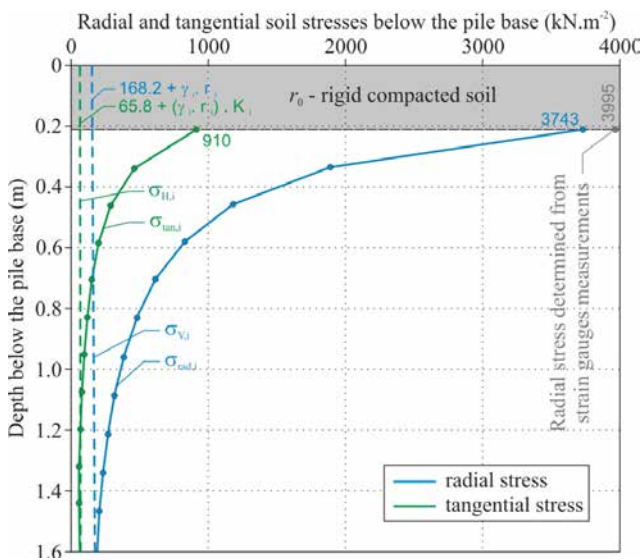


Figure 5. Distribution of the radial and tangential soil stresses below the pile base - TP2.

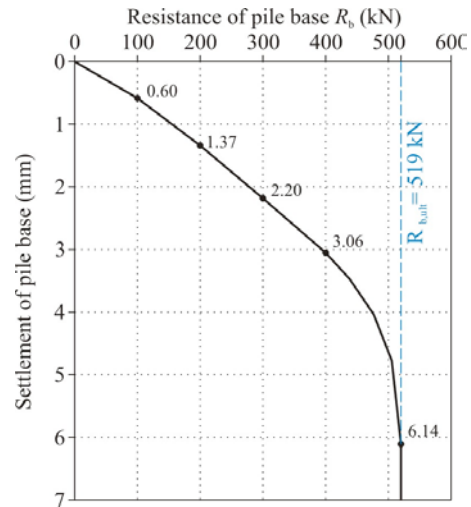


Figure 6. Resistance of the pile base-settlement curve - TP2.

The results presented are shown only for the magnitude of the vertical ultimate resistance of the pile base $Q_{b,ultimate}$, which is equal to the value of 519 kN. The resistance of the pile base depending on the soil displacement (compaction) is shown in Fig. 6.

In the next steps the ultimate stress $\sigma_{r,H,limit}$ and the ultimate shaft resistance, τ_{ult} and t_{ult} , are determined using equations (10), (12), and (13). The deformations required for full mobilization of the shaft friction Δ_M play a significant role in the calculation of the shaft resistance. The value of Δ_M was equal to 1.0 mm for

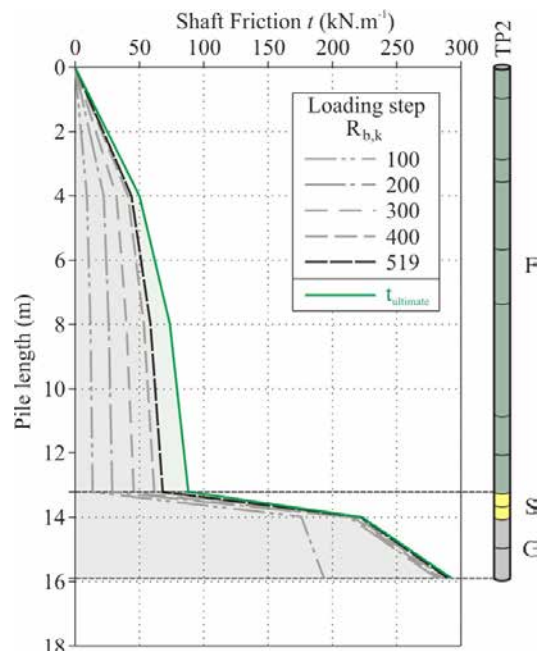


Figure 7. Distribution of the shaft friction over the pile length - TP2.

the coarse-grained soils and 10 to 20 mm for the fine-grained soils. The multiple factor κ was calculated according to the formulas for the displacement piles [11]. The distribution of the shaft friction over the pile's length is shown in Fig. 7. The presented curves are determined according to the results of the pile base (in the range from 0 to $R_{b,ult}$). The ultimate shaft friction t_{ult} is equal to the full mobilization of the shaft resistance (ultimate stress is moving in the plastic stress state).

These results make it possible to obtain a load distribution over the pile's length, as shown in Fig. 8. The calculated distribution of the load over the pile's length is compared with the measurements obtained using strain gauges in the static load test. This comparison confirms the correctness of the calculations. The difference between the calculated base resistance (519 kN) and the measured one (554 kN - SLT) is a 6% degree of accuracy. The difference at the boundary between the soft stratum and the coarse-grained soils (13.2 m) is a 4% degree of accuracy.

The comparison of the load-settlement curves obtained by the static load test and calculated using the CET is shown in Fig. 9. The comparison also includes the ratio of the pile base resistance to the total pile resistance. The results of the calculations are in good agreement with the measurements. The difference between the calculations and the measurements is less than about a 10% degree of accuracy.

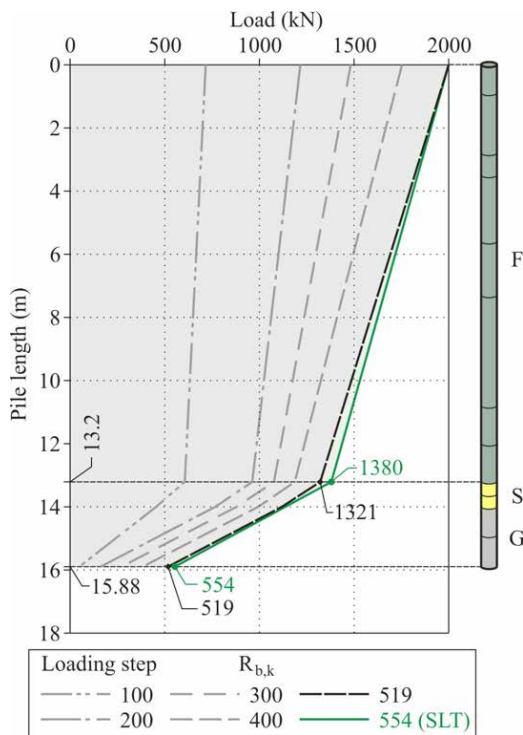


Figure 8. Distribution of the load over the pile's length - TP2.

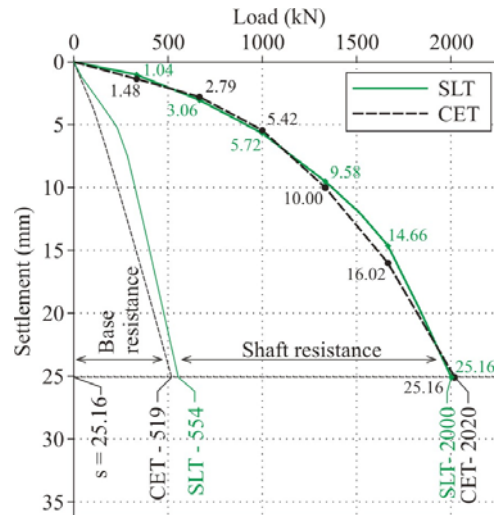


Figure 9. Load-settlement curve of DDS pile - TP2.

The results of the analyses of TP1 and TP3 are presented in the following part. The comparison of the calculated and measured load distributions over the pile's length (TP1) is shown in Fig. 10, and the comparison of the load-settlement curves is shown in Fig. 11.

As can be seen in Fig. 10, the calculated load distribution over the pile's length again provides a sufficient reliability. The difference between the calculated and measured load-settlement curves is less than a 5% degree of

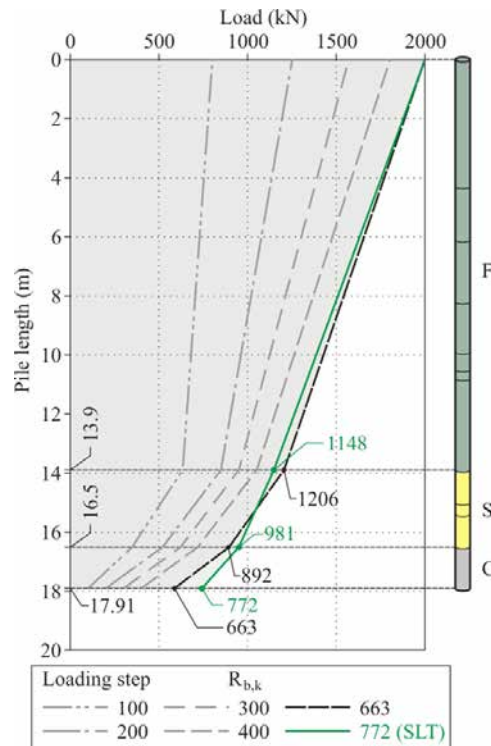


Figure 10. Distribution of the load over the pile's length - TP1.

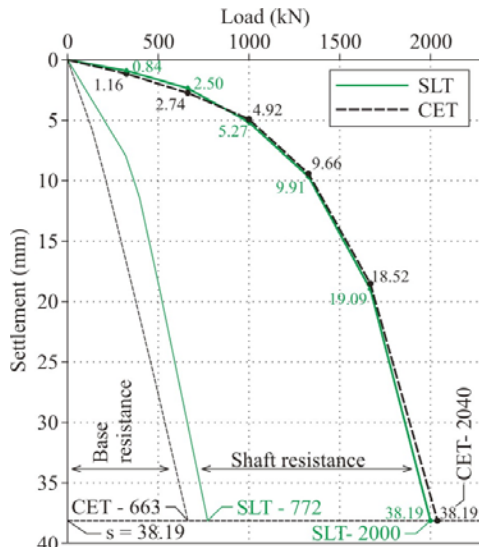


Figure 11. Load-settlement curve of DDS pile - TP1.

accuracy. A lower accuracy (< 15 %) is obtained for the pile-base resistance. It could be caused by insufficiently precise soil-strength parameters for the calculation of the pile base in this case, but the results are considered to be good enough. The results of the analyses of TP3 are presented in Fig. 12 and Fig. 13. Coarse-grained soils in the tested area of TP3 consist only of very dense gravels without any sand or sandy layers (Fig. 2), which leads to a higher bearing capacity.

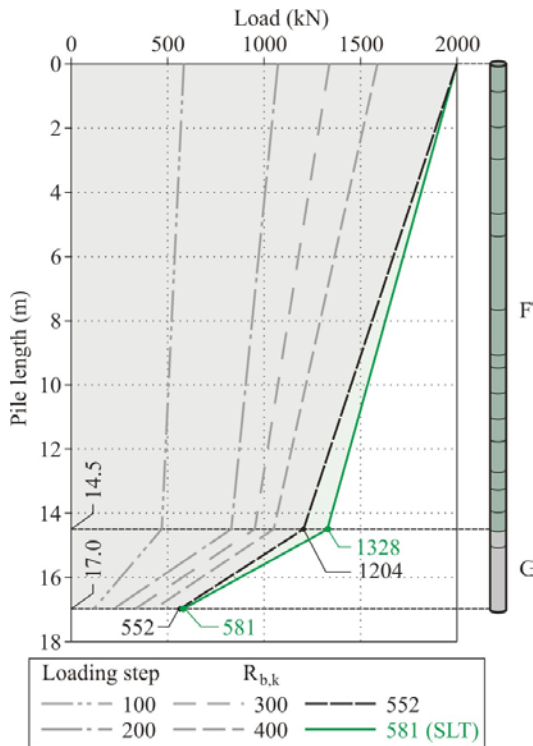


Figure 12. Distribution of the load over the pile's length - TP3.

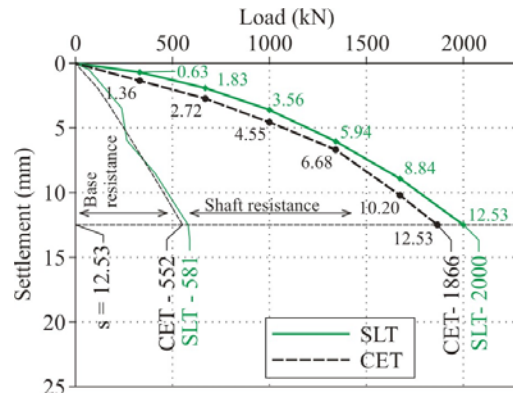


Figure 13. Load-settlement curve of DDS pile - TP3.

The vertical settlement of TP3 was significantly less than the previous ones. The use of the CET also allowed reliable results to be obtained in this case (TP3), while other methods (FEM and the Limit Load Curve Method according to Masopust [7]) were insufficiently accurate to reflect this difference [30].

In addition, CET makes it possible to calculate the changes of the stress state, the displacements, and the compaction around the pile that are affected by the pile technology. There are two different options for determining the pile resistance for a verification of the Ultimate Limit State (ULS). The first one is a determination of the pile resistance from a calculated load-settlement curve for a settlement equal to 10% of the pile diameter (41 mm in this case). The second one is the application of the presented theory in analytical calculation models. It is recommended that the characteristic values of the shaft resistance of the DDS pile can be calculated according to equation (15), taking into account the methodology presented.

$$R_{s,k} = \pi \cdot D \cdot \sum_{i=1}^n h_i \cdot (K_{H,i} \cdot \sigma_{or,i} \cdot \tan \varphi'_d + c'_d) \quad (15)$$

where $K_{H,i}$ is the coefficient of the horizontal earth pressure, which takes into account the impact of the technology; $\sigma_{or,i}$ is the geostatic stress at the middle of the i -layer; and φ'_d and c'_d are the effective parameters of the shear strength of the soil. Based on the CET method presented, the coefficient $K_{H,i}$ can be calculated using the following equation:

$$K_{H,i} = \frac{\sigma_{H,i} \cdot K_{\rho,H,i}}{\sigma_{V,i}} \quad (16)$$

where $\sigma_{V,i}$ is the vertical geostatic stress, $\sigma_{H,i}$ is the horizontal geostatic stress and $K_{\sigma,H,i}$ is the coefficient of the horizontal geostatic stress at the boundary of the compacted zone. This coefficient can be calculated using equation (2) or simply determined by using the diagrams presented by Mecsi [11].

6 CONCLUSION

Drilled Displacement System (DDS) piles are an innovative technology for pile foundations. DDS piles are created by rotary drilling, accompanied by a full horizontal displacement of the soil. The use of this technology can lead to a more effective and economical design in comparison with traditional pile technologies. Suitable geological conditions for DDS piles include sands, sandy gravels, and fine-grained soils, where a horizontal displacement can cause compaction of the surrounding soil. This process leads to an increase in the pile shaft's resistance.

The results of the three static load tests of the DDS piles are presented and analysed. These analyses include comparisons of the calculated load-settlement curves and load distributions over the pile length with the results of the static load test. A simple description of the methodology of CET is presented in the analysis of the test pile TP2. The detailed calculations include the distribution of the radial and tangential soil stresses, which are reflected in the pile base resistance-settlement curve. The calculations of the pile shaft's resistance include a determination of the shaft friction, the load distribution over the pile's length, and the load-settlement curve of the DDS pile. The analysis also includes changes to the soil stress state and the soil properties around the pile, which are affected by the pile technology.

The results of the analysis show very good agreement between the measurements and the calculations. The maximum difference between the load-settlement curves obtained using CET and SLT is equal to about a 10% degree of accuracy. The comparisons of the calculated and measured load distributions over the pile length provide the required degree of accuracy and confirm the correctness of the calculation methodology. The analyses confirm the suitability of the CET for the design of displacement piles. The CET allows a calculation of the soil properties, which are directly affected by the impact of the technology. These soil properties make it possible to take into account the impact of the DDS technology in analytical solutions of the pile resistance and they could also be used for numerical modelling.

Acknowledgments

The paper is one of the outcomes of the Grant VEGA agency No. 1 /0882/16: Influence of boundary conditions to limit states of geotechnical structures.

REFERENCES

- [1] Tomlinson, M., Woodward, J. 2007. Pile design and construction practice. 5th ed., Taylor & Francis e-Library.
- [2] Viggiani, C., Mandolini, A., Russo, G. 2012. Piles and pile foundations. Taylor & Francis, UK.
- [3] NeSmith, W. 2002. Static capacity analysis of augered, pressure-injected displacement piles. Int. Deep Foundations Congress, Florida, USA, pp. 1174-1186.
- [4] Zhussupbekov, A.Z., Ashkey, Y., Bazilov, R., Bazarbaev, D., Alibekova, N., Zhussupbekov, A. 2012. Geotechnical problems of new capital Astana (Kazakhstan). <http://www.mygeoworld.com/File/10268/geotechnical-problems-of-new-capital-astana-kazakhstan/download>, 10.10. 2017
- [5] Brown, D.A. 2005. Practical consideration in the selection and use of continuous flight auger and drilled displacement piles. Proc. Advances in design and testing deep foundations, Texas, USA, pp. 251-261. DOI: 10.1061/40778(157)1
- [6] Coyle, H.M., Reese, L.C. 1996. Load transfer for axially loaded piles in clay. Soil Mechanics and Foundations Division 92, 2, 1-26.
- [7] Masopust, J. 1994. Bored piles. Čenek a Ježek s.r.o., Prague, Czech Republic, [in Czech].
- [8] Nejad, F.P., Jaksa, M.B., Kakhi, M., McCabe, B.A. 2009. Prediction of pile settlement using artificial neural networks based on standard penetration test data. Computers and Geotechnics 36, 1125-1133.
- [9] Wang, Z., Xie, X., Wang, J. 2012. A new nonlinear method for vertical settlement prediction of a single pile and pile groups in layered soils. Computers and Geotechnics 45, 118-126. DOI: 10.1016/j.compgeo.2012.05.011
- [10] Zhang, Q.Q., Zhang, Z.M., Hej, Y. 2010. A simplified approach for settlement analysis of single pile and pile groups considering interaction between identical piles in multilayered soils. Computers and Geotechnics 37, 7-8, 969-976. DOI: 10.1016/j.compgeo.2010.08.003
- [11] Mecsi, J. 2013. Geotechnical engineering examples and solutions using the cavity expansion theory. Geotechnical Society Hungary, Budapest, Hungary.
- [12] Mecsi, J. 1996. Stresses, displacements, volume changes around the expansion cylinder in the soil. Proc. 10th Eur. Conf. Soil Mechanics and Foundation Engineering. Rotterdam, The Netherlands, pp. 243-246.
- [13] Vesic, A.S. 1972. Expansion of cavities in infinite soil mass. Soil Mechanics and Foundations Division 98, 3, 265-290.

- [14] Carter, J.P., Booker, J.R., Yeung, S.K. 1986. Cavity expansion in cohesive frictional soil. *Geotechnique* 36, 3, 349-358. DOI: 10.1680/geot.1986.36.3.349
- [15] Yu, H.S., Carter, J.P. 2002. Rigorous similar solutions for cavity expansion in cohesive-frictional soils. *Int. Journal of Geomechanics* 2, 2, 233-258.
- [16] Ladányi, B. 1963. Evaluation of pressuremeter tests in granular soils. *Proc. 2nd Pan American Conf. on Soil Mechanics and Foundation Engineering, Brazil, Vol. 1*, pp. 3-20.
- [17] Ervin, M.C. 1983. In-situ testing for geotechnical investigations. A.A. Balkema.
- [18] Salgado, R., Prezzi, M. 2007. Computation of cavity expansion pressure and penetration resistance in sands. *Int. Journal of Geomechanics* 7, 4, 251-265. DOI: 10.1061/(ASCE)1532-3641(2007)7:4(251)
- [19] Yu, H.S. 2000. *Cavity expansion methods in geomechanics*, Kluwer Academic Publishers Dordrecht, The Netherlands. DOI: 10.1007/978-94-015-9596-4
- [20] Au, S.K.A., Yeung, A.T., Soga, K. 2006. Pressure-controlled cavity expansion in clay. *Canadian Geotechnical Journal* 43, 7, 714-725. DOI: 10.1139/t06-037
- [21] Frikha, W., Bouassida, M. 2013. Cylindrical cavity expansion in elastoplastic medium with a variable potential flow. *Int. Journal of Geomechanics* 13, 1, 9-15. DOI: 10.1061/(ASCE)GM.1943-5622.0000166
- [22] Chadwick, P. 1959. The quasi-static expansion of a spherical cavity in metal and ideal soil. *The Quarterly Journal of Mechanics and Applied Mathematics* 12, 1, 52-71. DOI: 10.1093/qjmam/12.1.52
- [23] Zhou, W.H., Yin, J.H. 2008. A simple math model for soil nail and soil interaction analysis. *Computer and Geotechnics* 35, 3, 479-488. DOI: 10.1016/j.compgeo.2007.07.001
- [24] Xiao, Z.R., Zhang, Z., Du, M.F. 2004. An elastoplastic closed-form approach of cavity expansion in saturated soil based on modified Cam clay model. *Rock and Soil Mechanics* 25, 9, 1373-1378 [in Chinese].
- [25] Fernando, V., Moore, I.D. 2002. Use of cavity expansion theory to predict ground displacement during pipe bursting. *Pipelines 2002 - Beneath Our Feet: Challenges and Solutions*, American Society of Civil Engineers, Ohio, USA. DOI: 10.1061/40641(2002)81
- [26] Rao, P., Cui, J., Li, J. 2014. The elastoplastic solutions of cylindrical cavity expansion considering the $K_0 \neq 1$. *Proc. Advances in Soil Dynamics and Foundations Engineering GSP 240, Geo-Shanghai 2014, Shanghai, China*; pp. 433-443. DOI: 10.1061/9780784413425.044
- [27] Li, J., Gong, W., Li, L., Liu, F. 2017. Drained elastoplastic solution for cylindrical cavity expansion in K_0 -consolidated anisotropic soil. *Journal of Engineering Mechanics* 143(11). DOI: 10.1061/(ASCE)EM.1943-7889.0001357
- [28] Stacho, J., Ladicsova, E. 2014. Numerical Analysis of Drilled Displacement System Piles. *Proc. SGEM 2014, GeoConference on Science and Technologies in Geology, Exploration and Mining, Sofia, Bulgaria*, pp. 665-672. DOI: <http://dx.doi.org/10.5593/SGEM2014/B12/S2.085>
- [29] Tosini, L., Cividini, A., Gioda, G. 2010. A numerical interpretation of load tests on bored piles. *Computers and Geotechnics* 37, 3, 425-431. DOI: 10.1016/j.compgeo.2010.01.001
- [30] Stacho, J. 2013. Calculation of drilled displacement pile resistance by finite element method. *Proc. Advances in Architectural, Civil and Environmental Engineering, 23rd Annual PhD Student Conf., Bratislava, Slovakia*, pp. 498-505 [in Slovak].

NAVODILA AVTORJEM

Vsebina članka

Članek naj bo napisan v naslednji obliki:

- Naslov, ki primerno opisuje vsebino članka in ne presega 80 znakov.
- Izvleček, ki naj bo skrajšana oblika članka in naj ne presega 250 besed. Izvleček mora vsebovati osnove, jedro in cilje raziskave, uporabljeno metodologijo dela, povzetek izidov in osnovne sklepe.
- Največ 6 ključnih besed, ki bi morale biti napisane takoj po izvlečku.
- Uvod, v katerem naj bo pregled novejšega stanja in zadostne informacije za razumevanje ter pregled izidov dela, predstavljenih v članku.
- Teorija.
- Eksperimentalni del, ki naj vsebuje podatke o postavitvi preiskusa in metode, uporabljene pri pridobitvi izidov.
- Izidi, ki naj bodo jasno prikazani, po potrebi v obliki slik in preglednic.
- Razprava, v kateri naj bodo prikazane povezave in posplošitve, uporabljene za pridobitev izidov. Prikazana naj bo tudi pomembnost izidov in primerjava s poprej objavljenimi deli.
- Sklepi, v katerih naj bo prikazan en ali več sklepov, ki izhajajo iz izidov in razprave.
- Vse navedbe v besedilu morajo biti na koncu zbrane v seznamu literature, in obratno.

Dodatne zahteve

- Vrstice morajo biti zaporedno oštevilčene.
- Predložen članek ne sme imeti več kot 18 strani (brez tabel, legend in literature); velikost črk 12, dvojni razmik med vrsticami. V članek je lahko vključenih največ 10 slik. Isti rezultati so lahko prikazani v tabelah ali na slikah, ne pa na oba načina.
- Potrebno je priložiti imena, naslove in elektronske naslove štirih potencialnih recenzentov članka. Urednik ima izključno pravico do odločitve, ali bo te predloge upošteval.

Enote in okrajšave

V besedilu, preglednicah in slikah uporabljajte le standardne označbe in okrajšave SI. Simbole fizikalnih veličin v besedilu pišite poševno (npr. v , T itn.). Simbole enot, ki so sestavljene iz črk, pa pokončno (npr. Pa, m itn.). Vse okrajšave naj bodo, ko se prvič pojavijo, izpisane v celoti.

Slike

Slike morajo biti zaporedno oštevilčene in označene, v besedilu in podnaslovu, kot sl. 1, sl. 2 itn. Posnete naj bodo v katerem koli od razširjenih formatov, npr. BMP, JPG, GIF. Za pripravo diagramov in risb priporočamo CDR format (CorelDraw), saj so slike v njem vektorske in jih lahko pri končni obdelavi preprosto povečujemo ali pomanjšujemo.

Pri označevanju osi v diagramih, kadar je le mogoče, uporabite označbe veličin (npr. v , T itn.). V diagramih z več krivuljami mora biti vsaka krivulja označena. Pomen oznake mora biti razložen v podnapisu slike.

Za vse slike po fotografskih posnetkih je treba priložiti izvirne fotografije ali kakovostno narejen posnetek.

Preglednice

Preglednice morajo biti zaporedno oštevilčene in označene, v besedilu in podnaslovu, kot preglednica 1, preglednica 2 itn. V preglednicah ne uporabljajte izpisanih imen veličin, ampak samo ustrezne simbole. K fizikalnim količinam, npr. t (pisano poševno), pripišite enote (pisano pokončno) v novo vrsto brez oklepajev. Vse opombe naj bodo označene z uporabo dvignjene številke¹.

Seznam literature

Navedba v besedilu

Vsaka navedba, na katero se sklicujete v besedilu, mora biti v seznamu literature (in obratno). Neobjavljeni rezultati in osebne komunikacije se ne priporočajo v seznamu literature, navedejo pa se lahko v besedilu, če je nujno potrebno.

Oblika navajanja literature

V besedilu: Navedite reference zaporedno po številkah v oglatih oklepajih v skladu z besedilom. Dejanski avtorji so lahko navedeni, vendar mora obvezno biti podana referenčna številka.

Primer: »..... kot je razvidno [1,2]. Brandl and Blovsky [4], sta pridobila drugačen rezultat...«

V seznamu: Literaturni viri so oštevilčeni po vrstnem redu, kakor se pojavijo v članku. Označimo jih s številkami v oglatih oklepajih.

Sklicevanje na objave v revijah:

- [1] Jelušič, P., Žlender, B. 2013. Soil-nail wall stability analysis using ANFIS. Acta Geotechnica Slovenica 10(1), 61-73.

Sklicevanje na knjigo:

- [2] Šuklje, L. 1969. Rheological aspects of soil mechanics. Wiley-Interscience, London

Sklicevanje na poglavje v monografiji:

- [3] Mitchel, J.K. 1992. Characteristics and mechanisms of clay creep and creep rupture, in N. Guven, R.M. Pollastro (eds.), Clay-Water Interface and Its Rheological Implications, CMS Workshop Lectures, Vol. 4, The clay minerals Society, USA, pp. 212-244..

Sklicevanje na objave v zbornikih konferenc:

- [4] Brandl, H., Blovsky, S. 2005. Slope stabilization with socket walls using the observational method. Proc. Int. conf. on Soil Mechanics and Geotechnical Engineering, Bratislava, pp. 2485-2488.

Sklicevanje na spletne objave:

- [5] Kot najmanj, je potrebno podati celoten URL. Če so poznani drugi podatki (DOI, imena avtorjev, datumi, sklicevanje na izvorno literaturo), se naj prav tako dodajo.

INSTRUCTIONS FOR AUTHORS

Format of the paper

The paper should have the following structure:

- A Title, which adequately describes the content of the paper and should not exceed 80 characters;
- An Abstract, which should be viewed as a mini version of the paper and should not exceed 250 words. The Abstract should state the principal objectives and the scope of the investigation and the methodology employed; it should also summarise the results and state the principal conclusions;
- Immediately after the abstract, provide a maximum of 6 keywords;
- An Introduction, which should provide a review of recent literature and sufficient background information to allow the results of the paper to be understood and evaluated;
- A Theoretical section;
- An Experimental section, which should provide details of the experimental set-up and the methods used to obtain the results;
- A Results section, which should clearly and concisely present the data, using figures and tables where appropriate;
- A Discussion section, which should describe the relationships shown and the generalisations made possible by the results and discuss the significance

Podatki o avtorjih

Članku priložite tudi podatke o avtorjih: imena, nazive, popolne poštne naslove, številke telefona in faksa, naslove elektronske pošte. Navedite kontaktno osebo.

Sprejem člankov in avtorske pravice

Uredništvo si pridržuje pravico do odločanja o sprejemu članka za objavo, strokovno oceno mednarodnih recenzentov in morebitnem predlogu za krajšanje ali izpopolnitev ter terminološke in jezikovne korekture. Z objavo preidejo avtorske pravice na revijo ACTA GEOTECHNICA SLOVENICA. Pri morebitnih kasnejših objavah mora biti AGS navedena kot vir.

Vsa nadaljnja pojasnila daje:

Uredništvo
 ACTA GEOTECHNICA SLOVENICA
 Univerza v Mariboru,
 Fakulteta za gradbeništvo, prometno inženirstvo in arhitekturo
 Smetanova ulica 17, 2000 Maribor, Slovenija
 E-pošta: ags@uni-mb.si

- of the results, making comparisons with previously published work;
- Conclusions, which should present one or more conclusions that have been drawn from the results and subsequent discussion;
- A list of References, which comprises all the references cited in the text, and vice versa.

Additional Requirements for Manuscripts

- Use double line-spacing.
- Insert continuous line numbering.
- The submitted text of Research Papers should cover no more than 18 pages (without Tables, Legends, and References, style: font size 12, double line spacing). The number of illustrations should not exceed 10. Results may be shown in tables or figures, but not in both of them.
- Please submit, with the manuscript, the names, addresses and e-mail addresses of four potential referees. Note that the editor retains the sole right to decide whether or not the suggested reviewers are used.

Units and abbreviations

Only standard SI symbols and abbreviations should be used in the text, tables and figures. Symbols for physical quantities in the text should be written in *Italics* (e.g. v , T , etc.). Symbols for units that consist of letters should

be in plain text (e.g. Pa, m, etc.).

All abbreviations should be spelt out in full on first appearance.

Figures

Figures must be cited in consecutive numerical order in the text and referred to in both the text and the caption as Fig. 1, Fig. 2, etc. Figures may be saved in any common format, e.g. BMP, JPG, GIF. However, the use of CDR format (CorelDraw) is recommended for graphs and line drawings, since vector images can be easily reduced or enlarged during final processing of the paper.

When labelling axes, physical quantities (e.g. v , T , etc.) should be used whenever possible. Multi-curve graphs should have individual curves marked with a symbol; the meaning of the symbol should be explained in the figure caption. Good quality black-and-white photographs or scanned images should be supplied for the illustrations.

Tables

Tables must be cited in consecutive numerical order in the text and referred to in both the text and the caption as Table 1, Table 2, etc. The use of names for quantities in tables should be avoided if possible: corresponding symbols are preferred. In addition to the physical quantity, e.g. t (in Italics), units (normal text), should be added on a new line without brackets.

Any footnotes should be indicated by the use of the superscript¹.

LIST OF references

Citation in text

Please ensure that every reference cited in the text is also present in the reference list (and vice versa). Any references cited in the abstract must be given in full. Unpublished results and personal communications are not recommended in the reference list, but may be mentioned in the text, if necessary.

Reference style

Text: Indicate references by number(s) in square brackets consecutively in line with the text. The actual authors can be referred to, but the reference number(s) must always be given:

Example: "... as demonstrated [1,2]. Brandl and Blovsky [4] obtained a different result ..."

List: Number the references (numbers in square brackets) in the list in the order in which they appear in the text.

Reference to a journal publication:

- [1] Jelušič, P., Žlender, B. 2013. Soil-nail wall stability analysis using ANFIS. *Acta Geotechnica Slovenica* 10(1), 61-73.

Reference to a book:

- [2] Šuklje, L. 1969. Rheological aspects of soil mechanics. Wiley-Interscience, London

Reference to a chapter in an edited book:

- [3] Mitchel, J.K. 1992. Characteristics and mechanisms of clay creep and creep rupture, in N. Guven, R.M. Pollastro (eds.), *Clay-Water Interface and Its Rheological Implications*, CMS Workshop Lectures, Vol. 4, The clay minerals Society, USA, pp. 212-244.

Conference proceedings:

- [4] Brandl, H., Blovsky, S. 2005. Slope stabilization with socket walls using the observational method. *Proc. Int. conf. on Soil Mechanics and Geotechnical Engineering*, Bratislava, pp. 2485-2488.

Web references:

- [5] As a minimum, the full URL should be given and the date when the reference was last accessed. Any further information, if known (DOI, author names, dates, reference to a source publication, etc.), should also be given.

Author information

The following information about the authors should be enclosed with the paper: names, complete postal addresses, telephone and fax numbers and E-mail addresses. Indicate the name of the corresponding author.

Acceptance of papers and copyright

The Editorial Committee of the Slovenian Geotechnical Review reserves the right to decide whether a paper is acceptable for publication, to obtain peer reviews for the submitted papers, and if necessary, to require changes in the content, length or language.

On publication, copyright for the paper shall pass to the ACTA GEOTECHNICA SLOVENICA. The AGS must be stated as a source in all later publication.

For further information contact:

Editorial Board

ACTA GEOTECHNICA SLOVENICA

University of Maribor,

Faculty of Civil Engineering, Transportation Engineering and Architecture

Smetanova ulica 17, 2000 Maribor, Slovenia

E-mail: ags@uni-mb.si

NAMEN REVIEJE

Namen revije ACTA GEOTECHNICA SLOVENICA je objavljane kakovostnih teoretičnih člankov z novih pomembnih področij geomehanike in geotehnike, ki bodo dolgoročno vplivali na temeljne in praktične vidike teh področij.

ACTA GEOTECHNICA SLOVENICA objavlja članke s področij: mehanika zemljin in kamnin, inženirska geologija, okoljska geotehnika, geosintetika, geotehnične konstrukcije, numerične in analitične metode, računalniško modeliranje, optimizacija geotehničnih konstrukcij, terenske in laboratorijske preiskave.

Revija redno izhaja dvakrat letno.

AVTORSKE PRAVICE

Ko uredništvo prejme članek v objavo, prosi avtorja(je), da prenese(jo) avtorske pravice za članek na izdajatelja, da bi zagotovili kar se da obsežno razširjanje informacij. Naša revija in posamezni prispevki so zaščiteni z avtorskimi pravicami izdajatelja in zanje veljajo naslednji pogoji:

Fotokopiranje

V skladu z našimi zakoni o zaščiti avtorskih pravic je dovoljeno narediti eno kopijo posameznega članka za osebno uporabo. Za naslednje fotokopije, vključno z večkratnim fotokopiranjem, sistematičnim fotokopiranjem, kopiranjem za reklamne ali predstavitvene namene, nadaljnjo prodajo in vsemi oblikami nedobičkonosne uporabe je treba pridobiti dovoljenje izdajatelja in plačati določen znesek.

Naročniki revije smejo kopirati kazalo z vsebino revije ali pripraviti seznam člankov z izvlečki za rabo v svojih ustanovah.

Elektronsko shranjevanje

Za elektronsko shranjevanje vsakršnega gradiva iz revije, vključno z vsemi članki ali deli članka, je potrebno dovoljenje izdajatelja.

ODGOVORNOST

Revija ne prevzame nobene odgovornosti za poškodbe in/ali škodo na osebah in na lastnini na podlagi odgovornosti za izdelke, zaradi malomarnosti ali drugače, ali zaradi uporabe kakršnekoli metode, izdelka, navodil ali zamisli, ki so opisani v njej.

AIMS AND SCOPE

ACTA GEOTECHNICA SLOVENICA aims to play an important role in publishing high-quality, theoretical papers from important and emerging areas that will have a lasting impact on fundamental and practical aspects of geomechanics and geotechnical engineering.

ACTA GEOTECHNICA SLOVENICA publishes papers from the following areas: soil and rock mechanics, engineering geology, environmental geotechnics, geosynthetic, geotechnical structures, numerical and analytical methods, computer modelling, optimization of geotechnical structures, field and laboratory testing.

The journal is published twice a year.

COPYRIGHT

Upon acceptance of an article by the Editorial Board, the author(s) will be asked to transfer copyright for the article to the publisher. This transfer will ensure the widest possible dissemination of information. This review and the individual contributions contained in it are protected by publisher's copyright, and the following terms and conditions apply to their use:

Photocopying

Single photocopies of single articles may be made for personal use, as allowed by national copyright laws. Permission of the publisher and payment of a fee are required for all other photocopying, including multiple or systematic copying, copying for advertising or promotional purposes, resale, and all forms of document delivery.

Subscribers may reproduce tables of contents or prepare lists of papers, including abstracts for internal circulation, within their institutions.

Electronic Storage

Permission of the publisher is required to store electronically any material contained in this review, including any paper or part of the paper.

RESPONSIBILITY

No responsibility is assumed by the publisher for any injury and/or damage to persons or property as a matter of product liability, negligence or otherwise, or from any use or operation of any methods, products, instructions or ideas contained in the material herein.



University of Maribor
Faculty of Civil Engineering,
Transportation Engineering
and Architecture

www.fgpa.um.si

University
of Ljubljana



Faculty of
Civil and Geodetic
Engineering

Faculty of
Natural Sciences and
Engineering

www.fgg.uni-lj.si
www.ntf.uni-lj.si



GEOTEHNIŠKO DRUŠTVO • IJDZETS
SLOVENIAN GEOTECHNICAL SOCIETY

www.sloged.si

SLOVENSKO DRUŠTVO ZA
PODOZEMNE GRADNJE
SLOVENIAN SOCIETY FOR
UNDERGROUND STRUCTURES

www.ita-slovenia.si